

## Final Report for AOARD Grant 09-1-4024

**"Large optoelectronic enhancement of light-harvesting polymers by chain confinement and charge percolation for LEDs and photocells based on ultrathin films and CNT nanocomposites"**

September 30, 2010

**Arnold C.-M. Yang**

Department of Materials Science and Engineering, National Tsing Hua University, Hsinchu 30013, Taiwan; Mailing Address : 101, Sec. 2, Kuang Fu Road, Hsinchu City, Taiwan 30013; Phone : +886 3 572 0792; Fax : +886 3 572 2366; [acyang@mse.nthu.edu.tw](mailto:acyang@mse.nthu.edu.tw),

Period of Performance: 01/09/2009 – 31/08/2010

### Abstract

The massive enhancement induced by molecular constraints in the optoelectronic efficiencies of conjugated polymers was investigated further using applied stresses, strains, and adhesions in both the amorphous (MEH-PPV) and the crystalline (P3HT) polymer systems. A confocal photoluminescence (PL) and Raman system integrated with in-situ atomic force microscopy was installed to unveil the microscopic optical properties as a function of the physical state as varying across the polymer samples. After removing the influence of a waveguide effect in the stretching experiment using strain-hardened matrices, the magnitude of the enhancement was found to be strongly dependence on the molecular strains ( $\varepsilon$ 's), becoming significant to ~2-fold as  $\varepsilon = 60\%$ , then reaching ~17-fold at  $\varepsilon = 300\%$ , and finally leveling to ~40-fold for  $\varepsilon$ 's greater than 530%, with the dominant emissions and the absorptions (PLE spectrum) independent of  $\varepsilon$ . The strain-induced enhancement was attributed to suppression of Franck-Condon type interactions in the stress-rigidified polymer chains, and it could be substantially reduced by the post-stretching relaxation and the intermolecular energy-draining pathways. Similar enhancement observed in the dewetted thin film systems was found to be also arising from this molecular constraint effect in that both the residual layer on the exposed substrates and the highly stretched surface layer on the droplets contributed to the observed PL enhancement. Very importantly, we also found that when the optoelectronic efficiencies were significantly enhanced by the molecular constraints, exciton hopping and the oxidative decays were both substantially suppressed.

Furthermore, as an extension to this molecular constraint effect, chain conformation was found to have strong effects on the optoelectronic efficiencies in the as-spun ultrathin films even before dewetting or stretching. It was found that the PL efficiencies were decreasing with film thickness until it eventually leveled off as the film thickness was above a threshold around 100 nm. This thickness dependence varied for different substrates, obviously due to the influences by substrate van der Waals interactions operative during the thin film formation process that had resulted different chain conformations. A unique charge injection phenomenon was noted for the films on bare silicon where the photoexcited excitons in MEH-PPV separated and injected into to silicon valence and conduction bands driven by the built-in voltage across the interface. This charge injection, however, was absent in the dewetted ultrathin residual layer, apparently due to the ultrahigh PL efficiencies in the highly molecularly constrained conjugated macromolecules so that the formation and thus the hopping of the excitons were substantially suppressed.

The molecular constraint effect was also explored in the conjugated polymer – carbon nanotubes systems with focuses on the synthesis, chain conformation, and photovoltaics properties of the ultrathin layer (~2 - 10nm) of conjugated polymer P3HT on carbon nanotubes. The electric conductivity of the ultrathin layer was found to be approximately 5 orders of magnitude smaller than the bulk. Quantitative analyses had concluded that charge tunneling or leakage currents were independent of this observation and attributed it to the electron hopping across the molecular scale thickness. It was found that as the coating thickness decreased, the crystallinity of the P3HT decreased, along with significant red-shifting of Raman that signified alterations of chain conformation. Furthermore, although the photoluminescence peak remained unchanged when grafted on CNTs, modifications of P3HT energy gap was observed, indicating variations of vibronic levels arising from the grafting. Moreover, broadening of the PL emission took place that suggested decreasing of

| <b>Report Documentation Page</b>  |                                    |   | Form Approved<br>OMB No. 0704-0188                        |   |
|---|------------------------------------|---|---|---|
| <p>Public reporting burden for the collection of information is estimated to average 1 hour per response, including the time for reviewing instructions, searching existing data sources, gathering and maintaining the data needed, and completing and reviewing the collection of information. Send comments regarding this burden estimate or any other aspect of this collection of information, including suggestions for reducing this burden, to Washington Headquarters Services, Directorate for Information Operations and Reports, 1215 Jefferson Davis Highway, Suite 1204, Arlington VA 22202-4302. Respondents should be aware that notwithstanding any other provision of law, no person shall be subject to a penalty for failing to comply with a collection of information if it does not display a currently valid OMB control number.</p> |                                    |   |   |   |
| 1. REPORT DATE<br><b>16 NOV 2010</b>  | 2. REPORT TYPE<br><b>Final</b>     | 3. DATES COVERED<br><b>07-07-2009 to 06-08-2010</b> |   |   |
| 4. TITLE AND SUBTITLE<br><b>Large Optoelectronic Enhancement of Light-Harvesting Polymers by Chain Confinement and Charge Percolation of</b>  |                                    |   | 5a. CONTRACT NUMBER<br><b>FA23860914024</b>               | 5b. GRANT NUMBER  |
|   |                                    |   | 5c. PROGRAM ELEMENT NUMBER                                |   |
| 6. AUTHOR(S)<br><b>Arnold Chang-Mou Yang</b>  |                                    |   | 5d. PROJECT NUMBER  | 5e. TASK NUMBER   |
|   |                                    |   | 5f. WORK UNIT NUMBER                                      |   |
| 7. PERFORMING ORGANIZATION NAME(S) AND ADDRESS(ES)<br><b>National Tsing Hua University, 101, Kuang Fu Rd, Sec 2, Hsinchu 30043, Taiwan, TW, 30043</b>   |                                    |   | 8. PERFORMING ORGANIZATION REPORT NUMBER<br><b>N/A</b>    |   |
| 9. SPONSORING/MONITORING AGENCY NAME(S) AND ADDRESS(ES)<br><b>AOARD, UNIT 45002, APO, AP, 96337-5002</b>  |                                    |   | 10. SPONSOR/MONITOR'S ACRONYM(S)<br><b>AOARD</b>          | 11. SPONSOR/MONITOR'S REPORT NUMBER(S)<br><b>AOARD-094024</b> |
| 12. DISTRIBUTION/AVAILABILITY STATEMENT<br><b>Approved for public release; distribution unlimited</b>   |                                    |   |   |   |
| 13. SUPPLEMENTARY NOTES   |                                    |   |   |   |
| 14. ABSTRACT<br><b>This is a report on the massive enhancement induced by molecular constraints in the optoelectronic efficiencies of conjugated polymers investigated by using applied stresses, strains, and adhesions in both amorphous MEH-PPV and crystalline P3HT polymer systems.</b>  |                                    |   |   |   |
| 15. SUBJECT TERMS<br><b>Conductive Polymers, nano photonics, Solar Cells</b>  |                                    |   |   |   |
| 16. SECURITY CLASSIFICATION OF:   |                                    |   | 17. LIMITATION OF ABSTRACT<br><b>Same as Report (SAR)</b> | 18. NUMBER OF PAGES<br><b>84</b>                              |
| a. REPORT<br><b>unclassified</b>  | b. ABSTRACT<br><b>unclassified</b> | c. THIS PAGE<br><b>unclassified</b>                 | 19a. NAME OF RESPONSIBLE PERSON                           |   |

lifetimes of the photo-generated species when grafted on CNTs. Bilayer photovoltaic devices with the [6,6]-phenyl C61-butyric acid methyl ester (PCBM) as the electron acceptor have shown that the nanocomposite P3HT/P3HT-g-CNT performed much more efficiently as the electron donor, in both photocurrent density and power conversion efficiency, compared to the neat P3HT. Finally, as reference systems for comparison, the molecular interactions during the nanoplastic flows in the nanocomposites of CNTs-PBO and SWCNTs-PS were investigated.

The research work was divided into the following segments: 1) Effects of molecular strains to chain hardening on photoluminescence (PL) efficiencies of conjugated polymer MEH-PPV, 2) Large PL enhancement of MEH-PPV conjugated polymer by dewetting processes, 3) Confocal optical study of PL enhancement in molecularly constrained MEH-PPV conjugated polymer by dewetting, 4) Molecular packing and the induced effect on PL of MEH-PPV in thin films prepared by spin coating, 5) The synthesis, chain conformation, PL, and photovoltaic behavior of ultrathin P3HT grafted on carbon nanotubes (CNTs), 6) The electric properties of ultrathin layer of conjugated polymer P3HT grafted on CNTS, 7) Molecular interactions during plastic flows between CNTs and rigid rod PBO chains in nanocomposites, 8) Nanoplastic flows between polymer chains and SWCNTs in the glassy state. The work will be illustrated in the sections that follow.

**List of Publications:** (publications, conference presentations, or patents resulted from this work.)

1. K. P. Tung, C.-H. J. Tsao, T. M. Hong<sup>2</sup>, K. C. Hwang, J.-H. Hsu, J. D. White, and A. C. -M. Yang\*, “Large Enhancements in Photoluminescence of Conjugated Polymers by Molecular Constraints via Mechanical Stretching”, submitted.
2. B. J. Chen, C. W. Yang, C. C. Chang, P. W. Lee, C. H. Tsao, G. Reiter, C. T. Yuan, J. Tang, T. L. Lin<sup>4</sup>, P. K. Wei, A. C.-M. Yang\*, “Large Optoelectronic Enhancement of Conjugated Macromolecules Constrained by Dewetting Interfacial Interactions”, submitted.
3. Chih-Wei Lin and Arnold C.-M. Yang, “Nano-Plastic Interactions of Surface-Grafted Single-Walled Carbon Nanotubes with Glassy Polymer Chains in Nanocomposites”, *Macromolecules*, in press.
4. Chih-Wei Lin, Anthony C.-Y. Chou, Steve L.-C. Hsu, Arnold C.-M. Yang\*, “Nano-Plastic Flows in Rigid-Rod Polybenzoxazole and the Molecular Reinforcement via Interactions with Surface-Grafted Carbon Nanotubes”, submitted to *Macromolecules*, in revision.
5. Anh Phuong Le, Tsai-Ming Huang, Po-Tsun Chen, Arnold Chang-Mou Yang\*, “The Synthesis and Optoelectronic Behaviour of Conjugated Polymer Poly(3-hexylthiophene) Grafted on the Surface of Multi-Walled Carbon Nanotubes”, submitted.
6. Tsai-Ming Huang, Chih-Wei Lin, Yen-Hui Liu, Le Anh Phuong, Arnold C.-M. Yang\*, “Electric Conductivity of Polymeric Nanolayers Grafted on Multi-walled Carbon Nanotubes in Nanocomposites”, in preparation.
7. Y. L. Chang, Y. Chien, Y. H. Chang, C. H. Wang, G. Reiter, A.C.-M. Yang\*, “Molecular Stresses in Metastable Ultrathin Polymer Films Cast from Spin Coating”, in preparation.
8. Peiwei Lee, Wei-Chen Li, Yi-Chien, Chih-Hong Chang, Po-Tsun Chen, Ya-Hui Yang, Arnold Chang-Mou Yang\*, “Confocal Micro-Photoluminescence Study of Dewetted Thin Films Containing Conjugated Polymer MEH-PPV”, in preparation.
9. Arnold C.-M. Yang, “Energy Release and the Induced Ultrahigh Optoelectronic Enhancements in Metastable Polymer Films by Spin Coating”, 2010 American Chemical Society Annual Meeting at Boston, August, 2010. (invited speaker)
10. Arnold C.-M. Yang, “Thin film instability of pi-conjugated macromolecules condensed from spin coating and the induced ultrahigh optoelectronic enhancement”, Materials and Manufacturing Directorate, Wright-Patterson Air Force Research Labs, Dayton, OH, August, 2010. (invited speaker)
11. Arnold C.-M. Yang, “Metastable Molecular Condensation of Conjugated Polymers in Ultrathin Films by Spin Coating and the Optoelectronic Enhancements by Energy Release Methods”, 7th US Air Force-Taiwan NSC Workshop on Nanoscience, I-Lan, Taiwan, March 2010.

12. Arnold C.-M. Yang, "Dramatic Optoelectronic Enhancements in Conjugated Polymers by Molecular Constraints ", 2010 Joint AFOSR and ONR Organic/Hybrid Photovoltaics Program Review, Santa Barbara, CA, June, 2010.

**DD882:** As a separate document, please complete and sign the inventions disclosure form.

## SECTION 1

### Large Enhancements in Photoluminescence of Conjugated Polymers by Molecular Constraints via Mechanical Stretching

K. P. Tung<sup>1</sup>, C.-H. J. Tsao<sup>1</sup>, T. M. Hong<sup>2</sup>, K. C. Hwang<sup>3</sup>, J.-H. Hsu<sup>4</sup>, J. D. White<sup>5</sup>, and A. C. -M. Yang<sup>1\*</sup>,

<sup>1</sup>Department of Materials Science and Engineering, <sup>2</sup>Department of Physics, <sup>3</sup>Department of Chemistry, National Tsing Hua University, Hsinchu 300, Taiwan.

<sup>4</sup>Department of Materials and Opto-electronics Science, National Sun-Yat-Sen University, Kaohsiung 804, Taiwan

<sup>5</sup>Department of Optoelectronics, Yuan Ze University, Taoyuan 320, Taiwan

#### Abstract

An enormous enhancement of photoluminescence (PL) in a conjugated polymer was observed when the polymer was finely dispersed and stretched to large molecular strains in a strain-hardened matrix that was optically inactive. This strain-induced enhancement was explored and attributed to suppression of Franck-Condon type interactions in the stress-rigidified polymer chains. While the dominant emissions and the absorptions (PLE spectrum) were unchanged, the PL enhancement illustrated a strong dependence on the molecular strains ( $\varepsilon$ 's), becoming significant to ~2-fold as  $\varepsilon = 60\%$ , then reaching ~17-fold at  $\varepsilon = 300\%$ , and finally leveling to ~40-fold for  $\varepsilon$ 's greater than 530%. Post-stretching relaxation was found causing substantial reduction of the effect. This stretch-induced enhancement was not observed in the concentrated MEH-PPV systems ( $c > 5\%$ ), however, indicating the existence of effective energy-draining pathways independent of the stretching effect.

#### Introduction

Conjugated polymers have enthused considerable interests owing to their unique optoelectronic properties, low cost, and ease of processing that promise a prominent future role in lighting, energy generation, and microelectronics [1-5]. With  $\pi$ -electronic orbitals extending in segments along the backbone, they harvest photons that match the vibronic gaps and generate electron-hole pairs that may soon relax into bound states, the excitons [6-29]. Upon formation, these photo-induced species may recombine to emit light or are separated and collected by the external electrodes. However, due to the strong interactions with chain vibrations (polaron interactions) [14,17,18,20-29], charge transport along chains is generally retarded, thus hopping mechanisms rise instead and dominate carrier migration in this class of materials. Consequently, non-radiative species emerge [8-13,30-33] and they may dissipate energy amounting to well above 90% of the total absorbed energy [8,10]. The resulted low quantum yields have long been the major hurdle for the development of polymer-based energy or lighting devices.

Although the microscopic description of photon energy transferring process is still in the making, the physical origins of these polaron interactions may be linked to the influences of local Coulomb interactions arising from photo-induced variations of the electronic clouds associated with the polymer segments [7,15-17, 20,21]. Separated by a distance of the order of 2-3 nm [7,10,14-17,20-22], the induced positive and negative charge centers may interact with chain vibrations (phonons) to reduce the local electrostatic energy increase and cause net conformation changes of the molecular strands. The incurred local deformations thereby obstruct the phase-conserving electronic redistribution, effectively forming so-called “self-trapping” for the induced charge carriers [6]. Obviously, polymer backbones of low rotational energies are prerequisite for this type of interactions, as is the case of long linear polymeric chains under no stresses. Conversely, if the polymer chains are stretched to the states that chain rotation energies are strictly prohibited, such Franck-Condon type interactions may be suppressed, and thus drastic enhancements of optoelectronic efficiencies may result.

Stretching conjugated macromolecules into large strains with diminutive relaxation, in fact, can be done by blending into an optically inert glassy polymer film and pulled on supporting ductile copper grids [37]. This method is particularly useful considering that pristine films of most conjugated polymers are brittle in the glassy state and deformations incurred above the glassy state are inherently associated with instantaneous relaxations. When dispersed in the film, the conjugated macromolecules deform congruently with the matrix polymer and may be stretched to very large molecular strains (more than 500%) in the local deformation zones [37-46]. Using this method, we have successfully

unveiled the effect of mechanical stretching and found dramatic enhancements in photoluminescent efficiencies in the stretched conjugated polymers.

### Experimental Section

The experiment was carried out by stretching the conjugated polymer (poly[2-methoxy-5-((2'-ethylhexyl)oxy)-1,4-phenylene-vinylene]) (MEH-PPV) dispersed in a thin film of either polystyrene (PS) or poly(2,6-dimethyl-1,4-diphenylene oxide) (PPO), both saturated glassy polymers. The conjugated polymer MEH-PPV ( $M_n = 150,000 \sim 250,000$  g/mol.,  $M_w/M_n \approx 5$ ) and the PPO ( $M_w = 244,000$  g/mol.,  $M_w/M_n \approx 3$ ) were both purchased from Sigma-Aldrich Chemical Co. The PS ( $M_w = 2,000,000$  g/mol.,  $M_w/M_n \leq 1.3$ ) and the styrene oligomers (OS) ( $M_w = 2,032$  g/mol.,  $M_w/M_n \leq 1.06$  and MW = 760 g/mol.,  $M_w/M_n \leq 1.1$ ) were obtained from the Pressure Chemical Co. All polymers were used as received without further purification. Blends of MEH-PPV with either PS or PPO were prepared with MEH-PPV weight fractions ( $c$ ) ranging from 0.1 wt % to 10 wt %.

Thin polymer films (~0.5 μm) were prepared by spin coating (2500 rpm ~ 3000 rpm) from the polymer solutions in a solvent mixture of equal-parted toluene, tetrahydrofuran, and cyclohexanone. The polymer solutions were wrapped in aluminum foil in all time for UV light protection. Before use, filtration of the solution was carried out by using syringe (0.2 μm pores) to remove dust or un-dissolved particles, which may have reduced the actual MEH-PPV concentration in the films. After spin coating, the film was floated off from the substrate onto a water surface and quickly picked up on a piece of copper grid [37,38]. The copper grids had been annealed at 600°C in vacuum for one hour to remove residual elasticity and then dip-coated with a thin polymer layer to promote the film adhesion [37,38]. After drying for about 1 day, the specimen was briefly exposed to solvent vapor to enhance film/grid bonding [37,38].

For stretching experiment, the specimen mounted on a strain jig was pulled uni-axially under an optical microscope to the applied deformation (Fig. 1a). The photo-luminescence (PL) spectra of the sample were recorded by using a Perkin-Elmer LS-55 photoluminescence spectrometer, with the data checked using another PL spectrometer (Horiba-Jobin Yvon FluoroMax®-3) by the integrated sphere method. Atomic force microscope, AFM, (Digital Instrumental, Nanoscope IIIa and Dimension™ 3100) and transmission electron microscope, TEM, (JEOL JEM-2010) were employed to investigate the topography and microstructure of local deformation zones of crazes. A confocal PL microscope (Leica SP2-Confocal) was also used to explore the microscopic luminescent properties of the stretched samples.

### Results and Discussions

Thin films of Pristine MEH-PPV films ( $c = 100\%$ ) were found very brittle and underwent cracking on the copper grid at low applied strains ( $e$ 's) ( $e < 2.0\%$ ), making it impossible to investigate the molecular deformation effect in this fashion.

However, when dispersed in a glassy polymer matrix, the MEH-PPV macromolecules were stably stretched up to more than 500% in the local deformation zones [37-46], allowing detailed study on the stretching effect.

Generally, glassy polymers develop local deformation zones beyond a threshold around  $e_c \sim 1\%$  as a result of local necking, initiating at the strain-softened regions that are subsequently strain-hardened to propagate the yielding zones. The macromolecules within these local deformation zones, in the form of either crazes [37-46] or shear deformation zones (SDZs) [37,40,44], are pulled into large molecular strains close to the stretching limit of the entangled chain network [37,38,42,44,46], approximately  $(l_e/d_e - 1)$  where  $l_e$  is the molecular contour length between entanglements and  $d_e$  is the direct distance between adjacent entanglement points [37]. Assuming that the MEH-PPV deforms congruently with the surrounding matrix, the molecular strain applied to the dispersed MEH-PPV molecules is  $\sim (l_e/d_e - 1)$  within the local deformation zones, and  $\varepsilon \sim e_c$  outside the local deformation zones, where  $l_e$ ,  $d_e$ , and  $e_c$  vary with the choice of the polymer matrix.

In the matrix of PS with molecular weight of 2M (PS2M), crazes emerged when  $e > e_c \sim 0.5\%$  (Fig. 1a) and the molecular strain in the crazes had been measured by TEM to be  $\varepsilon \sim (l_e/d_e - 1) \sim 300\%$  [37,38,41,42]. By approximating the craze as composing of closest-packed cylinders aligned to the stretch direction, the molecular strain within the craze can be conveniently determined from AFM profiling from the relationship

$$0.8 \times (\tau - 2D) \approx \tau / (\varepsilon + 1), \quad (1)$$

where  $D$  is the surface depression in the craze and  $\tau$  is the original film thickness [43-46]. For the blend systems containing MEH-PPV, it was found that  $D$  modestly decreased with  $c$  indicating that the MEH-PPV molecules participated to the local deformation, but the crazing behavior (e.g., the craze morphology and the threshold strain  $e_c$  for crazing) and the craze microstructure (Fig. 1b) were essentially invariant with  $c$  over the entire range explored here.

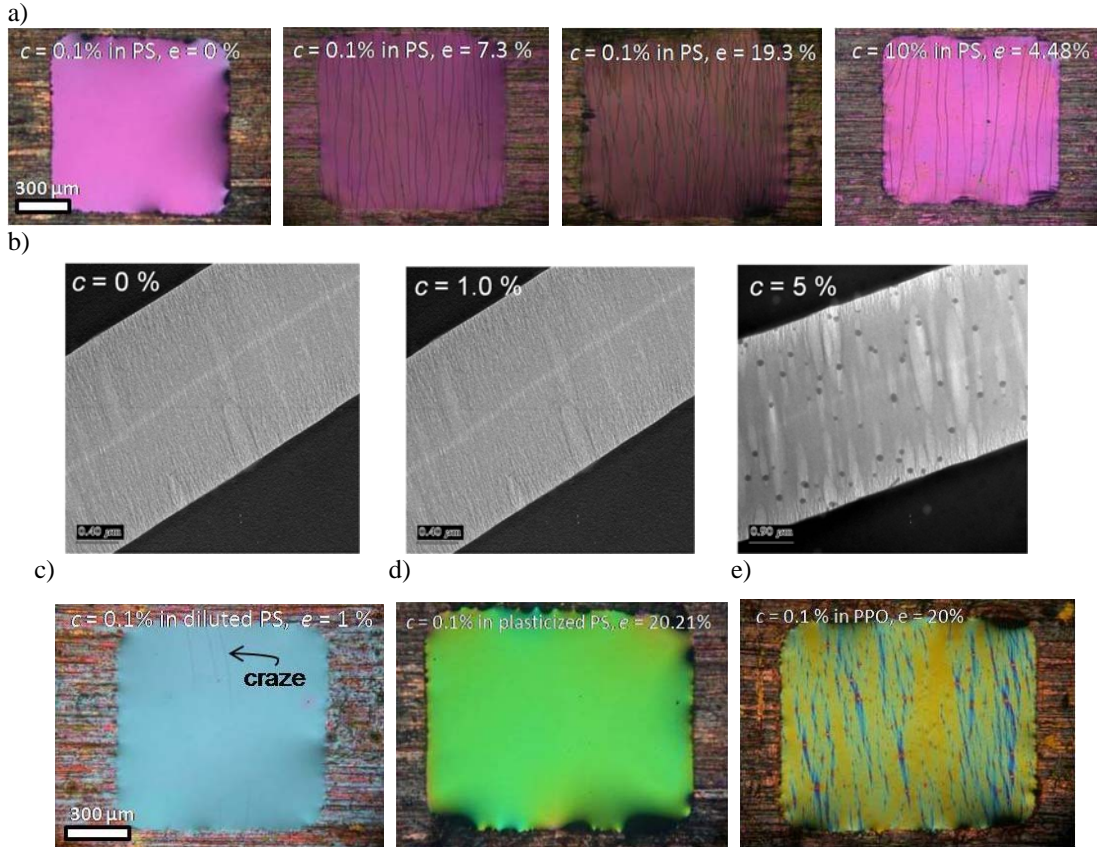


**Figure 1.** a) Optical micrographs of the polymer films for various MEHPPV fractions ( $c$ 's) and applied strains ( $\epsilon$ 's) where tiny local deformation zones (crazes) emerge in the stretched films. b) TEM micrographs of the local deformation zones (crazes) for various  $c$ 's. c) Tiny local deformation zones (crazes) grown in the brittle films of diluted chain entanglement network (with 50% of styrene oligomer, Mw = 2k g/mol.). d) Fully plasticized film (with 55 wt.% of styrene oligomer MW = 760 g/mol.) that deforms homogeneously up to  $\epsilon \sim 20\%$ . e) Local deformation zones (SDZs) grown in films of MEH-PPV dispersed in PPO matrix.

The dispersion of MEH-PPV in the PS2M matrix was generally acceptable for  $c \leq 1$  wt.%, but small MEH-PPV aggregate (diameter  $< 0.1$  μm) emerged in the more concentrated films ( $c \geq 5.0$  wt.%) (Fig. 1b). However, these aggregate particles did not disrupt the initiation and growth of the local deformation zones. The MEH-PPV that dissolved was assumed dispersed uniformly in the matrix.

Before stretching the PL spectra manifested a dominating intra-chain emission peak at ~550 nm (blue-shifted from that at ~565 nm of the pristine MEH-PPV film [33,47,48] due to the dilution effect) and a shoulder corresponding to the inter-molecular emission (Fig. 3a) [11,12,32] located identical to that of the pristine MEH-PPV films at ~600 nm. As  $c$  increased, the inter-chain emission increased in intensity in response to the increased tendency of chain aggregation. When normalized to  $c$ , the intra-chain intensity was about 20 times greater in samples of  $c = 0.1$  wt.% than that in  $c = 10.0$  wt.%, illustrating the dominance of inter-chain energy loss pathways in the concentrated samples [8-13]. Upon a mechanical strain applied to the films, a large enhancement in photoluminescence (PL) was observed in samples of  $c \leq 1$  wt.%. The PL enhancement, detectable to the bare eye (Figs. 2a), was

clearly manifested by the bright local deformation zones against the background of bulk (Fig. 2b) under a confocal fluorescence microscope despite that the deformation zones contained only 1/4 of the mass (and thus the MEH-PPV macromolecules) of the bulk. The PL intensities measured by using the PL spectrometer were observed to increase steadily with  $e$  (Figure 2d), consistently with the increase of the amount of stretched MEH-PPV molecules.

In a stark contrast, the PL intensities of the films of greater MEH-PPV concentrations ( $c \geq 5.0$  wt.%) were essentially unchanged upon stretching (Figure 2d) although comparable populations of local deformation zones (Fig. 1a) and similar craze microstructures were observed (Fig. 1b). These local deformation zones were clearly darker than the background (Figure 2c). A modest increase of the intra-chain emission, however, was detectable. Obviously, the non-radiative energy loss pathways had played a significant role during the energy transferring process following the absorption in these samples.

Nevertheless, for all  $c$ 's, the major emission peaks did not change with  $e$ . Consistently, the PLE spectra were also independent of  $e$  (Fig. 3a). Comparable PL behavior of the films was observed with either 480 nm or 350 nm excitation but the shorter wavelength of 350 nm was mostly used here to reduce the background interference.

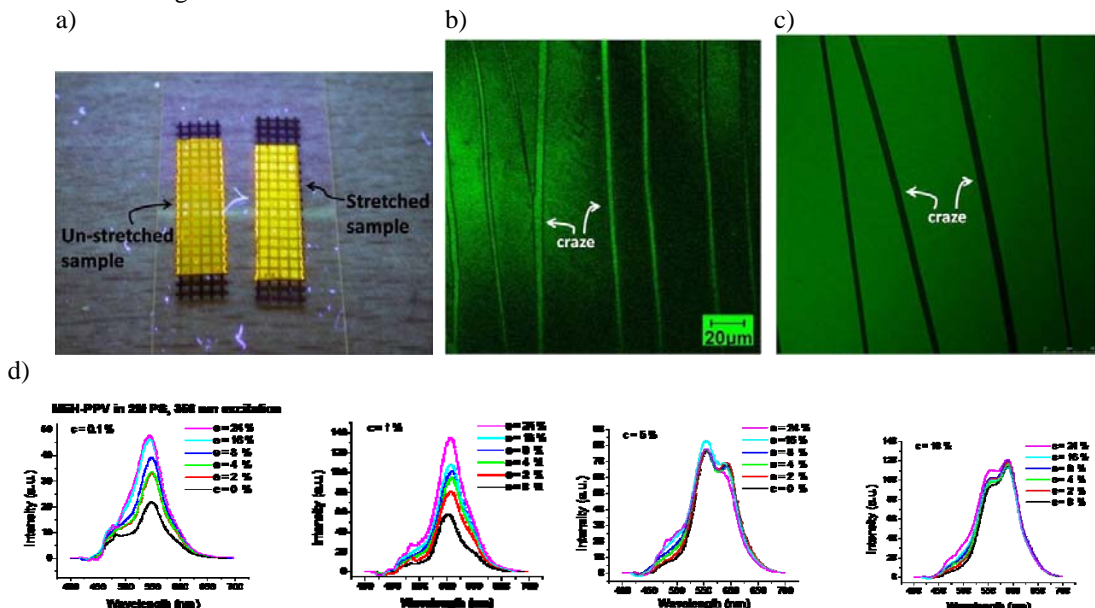


Figure 2. a) Luminescence enhancement by small strains in films of diluted MEH-PPV is observable to the bare eye. b) Confocal PL micrograph of a stretched sample of low MEH-PPV concentration ( $c = 1.0$  wt.%,  $e = 8\%$ , excitation frequency: 488 nm). c) Confocal PL micrograph of a stretched sample of high MEH-PPV concentration ( $c = 5.0$  wt.%,  $e = 8\%$ , excitation frequency: 488 nm). d) PL luminescence spectra for various  $c$ 's as a function of applied strain  $e$  (excitation wavelength: 350 nm).

A different polymer, PPO, was used for the matrix in exploring the regime of lower molecular strains as the PPO provided the molecular strain  $\varepsilon \sim (l_e/d_e - 1) \sim 60\%$  within the deformation zones of SDZs whilst  $e_c \sim 1.0\%$  in the elastic bulk [40]. In these samples, the PL spectra manifested much smaller PL enhancement upon stretching (Figure 3b) than those in the PS2M matrix where  $\varepsilon \sim 300\%$ .

The PL enhancement behavior under further lower molecular strains was studied by using a fully plasticized polymer as the matrix that contained PS2M and a styrene oligomer OS (MW = 760 g/mol.) in the weight ratio of 55: 45 (OS760: PS2M) [42]. These films deformed homogeneously without local deformation, giving  $\varepsilon = e$  everywhere in the samples [42]. In these samples, virtually no changes in the PL spectrum were observed for  $e$ 's up to  $e = 20\%$  (the breaking limit of the supporting copper grids), clearly indicating that no PL enhancements for molecular strains smaller than 20%.

It thus indicates that the MEH-PPV in the elastic bulk ( $\varepsilon \sim 0.5\%$ ) of the stretched samples made no contributions to the PL enhancement. The observed PL enhancement was entirely coming from the stretched MEH-PPV within the local deformation zones.

The molecular strain effect was further investigated by increasing  $\varepsilon$  using matrices of diluted PS entanglement networks. Typical examples of these diluted systems were blends of PS2M and a styrene oligomer ( $M_w = 2032$  g/mol.; OS2k) [42], which were glassy at room temperature and underwent local deformation upon stretching (Fig. 1c). The stretching limit  $l_e/l_0$  and thus the molecular strain  $\varepsilon$  within the local deformation zones increased with the dilution by OS2k, to  $\varepsilon = 380\%$  and  $550\%$ , respectively, for 30wt.% and 50wt.% OS2k [42]. As clearly shown by the PL spectra (Figures 3c and 3d), the stretched MEH-PPV therein manifested even greater increases of the PL intensities.

In order to analyze quantitatively the PL increases due to the mechanical stretching, we estimated the volume of local deformation zones as a function of applied strain  $e$ . It can be shown that the volume occupied by the deformation zones in the film is  $\frac{l_0^2 \tau(e - e_c)}{\varepsilon + 1}$ , where  $l_0$  is the original sample length, and

the volume of the elastic bulk is  $l_0(1 + e_c) \left[ 1 - \frac{e - e_c}{\varepsilon + 1} \right]$ . For simplicity, the PL intensity of the main peak

(at  $\sim 550$  nm) was used for comparison. The PL intensity measured from the sample ( $I_t$ ) was assumed to be a linear sum of the PL emissions from the local deformation zones ( $I_p$ ) and the elastic bulk ( $I_b$ ), i.e.,  $I_t = I_p V_p + I_b(1 - V_p)$  where  $V_p$  represents the film volume fraction of the local deformation zones. An apparent enhancement factor  $\gamma$  defined as  $I_p/I_b$  was thus expressed as

$$\gamma \equiv \frac{I_p}{I_b} = \frac{1}{V_p} \left( \frac{I_t}{I_b} - 1 + V_p \right). \quad (2)$$

Since the optical damping length  $z = \alpha^{-1}$  ( $\alpha$  is the absorption coefficient) measured in a UV-Visible spectrometer was around  $0.314$   $\mu\text{m}$  (at  $\lambda = 550$  nm at  $c = 1.0\%$ ), the  $V_p$  over the total light-emitting volume can be shown to be

$$V_p \equiv \frac{\tau(e - e_c)}{[z(\varepsilon + 1) + \tau(e - e_c)]}. \quad (3)$$

From the Eq. 2,  $\gamma$  was readily determined from the PL intensities  $I_t$  (of stretched samples) and  $I_b$  (of these samples without stretching), the applied strain  $e$ , the threshold strain for local deformation  $e_c$ , and the molecular strain  $\varepsilon$  in the local deformation zones.

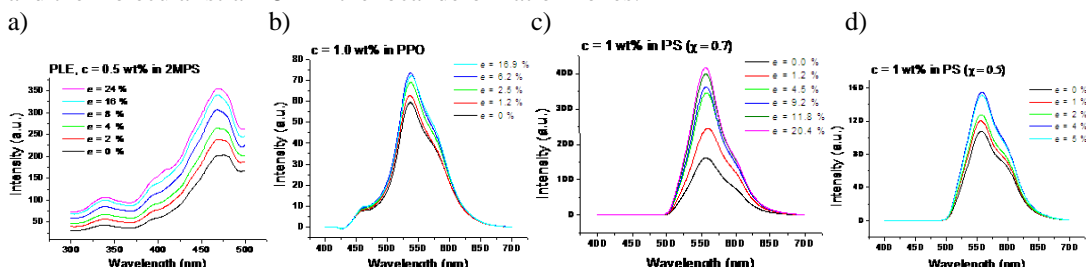


Figure 3. a) The PLE spectrum of the photoluminescent film is independent of the applied strain. b) PL spectra of MEH-PPV in PPO ( $c = 1$  wt%) stretched to various strain  $e$ 's. c) PL spectra of MEH-PPV in diluted PS matrix (30% OS2k,  $c = 1$  wt%). d) PL spectra of MEH-PPV in a diluted PS matrix (50% OS2k,  $c = 1$  wt%).

Before the actual enhancements were determined, a light extraction effect arising from the existence of local deformation zones in the film was analyzed and removed. Due to total internal reflection, a portion of the photoluminescent emissions was trapped in the film and parts of it would be released from the openings of the local deformation zones giving rise to inflated values of PL enhancement. This extra component, however, would saturate at large numbers of local deformations zones because the fraction of the trapped luminescence is known generally capped below around one half. Furthermore, previous experiments [44,45] had revealed that the local deformation zone population quickly leveled off for  $e$ 's greater than  $\sim 5\%$  after an initial increase with  $e$  in a typical glass polymer film of PS2M. Therefore, the light extraction effect could be removed if the PL enhancements were calculated from the incremental strain intervals  $(e_i, e_{i+1})$  at large  $e$ 's where the zone population was not increasing, via the Eqs. 2 and 3 with  $e_c = e_i$ ,  $e = e_{i+1}$ , and  $I_t = I_{e_{i+1}} - I_{e_i}$ . The enhancement factors so obtained were found to be very close to the extrapolated  $\gamma$  (defined by the Eq. 2) at large  $e$ 's (Figure 4a). This result indicates that the light extraction effect had become trivial at large  $e$ 's due to

dominance of the stretch-induced PL enhancement, consistent with the rapid decrease and then leveling-off of  $\gamma$  with  $e$ . For the convenience of determination, the PL enhancements were obtained from the saturated  $\gamma$  values from the plots of  $\gamma$  vs.  $e$  (Figure 4a).

In this fashion, the PL enhancement was measured and found to increase with molecular strain  $e$ , from barely changed (~1.0-fold) for  $e < 20\%$  (plasticized PS2M matrix), to ~2-fold for  $e = 60\%$  (PPO matrix), ~17-fold at  $e = 300\%$  (undiluted PS2M), ~33-fold at  $e = 380\%$  (diluted PS glass matrix), and finally leveling to ~40-fold at  $e = 530\%$  (diluted PS glass matrix), for  $c = 1.0\text{wt.\%}$  (Fig. 4b).

This large enhancement, if induced principally from the stress, should be very sensitive to stress relaxation. This was verified by annealing the stretched samples (MEH-PPV in the PS2M matrix) at  $90^\circ\text{C}$  with purged  $\text{N}_2$  because the local deformation zones of crazes in PS2M were known to undergo fibril coalescence at wide sections due to stress relaxation during physical ageing [41]. In these aged samples, the PL enhancement was found to decrease significantly from ~17-fold to ~10-fold at 5 hrs of annealing (Fig. 4c), consistent with the proposed stress-induced mechanism.

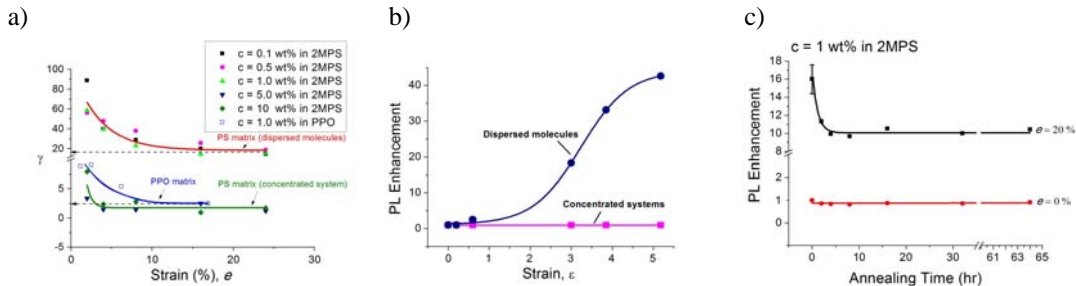


Figure 4. a) PL enhancement for the well-dispersed MEH-PPV as a function of  $e$  for  $c = 0.1$  and  $1.0\text{ wt.\%}$ , in PS, as well as  $c = 1\text{ wt.\%}$  in PPO. b) PL enhancements  $\gamma$  versus molecular deformation  $e$  for MEH-PPV molecules. (Due to fragility of the samples, the  $\gamma$  for  $e = 530\%$  was estimated by extrapolation to large  $e$ 's from the small  $e$ 's data.) c) The PL enhancement vs. annealing time ( $90^\circ\text{C}$  in purged  $\text{N}_2$ ).

The physical origin of this molecular strain effect was tentatively attributed to the suppression of the polaron interactions of the stress-rigidified MEH-PPV chains based on the well-accepted Franck-Condon principle vibronic interactions [6]. Although many details are still to be unveiled for the dynamic photoelectronic processes, it is reasonable to envisage that the electronic transitions upon photoexcitation give rise to well-separated positive and negative charge centers that are capable to interact instantaneously with the local segmental vibrations to lower the induced steric energy increase. For the generally flexible polymer chains, this would result in local chain deformations that form traps for the charge carriers until they hop away. As well known, large energy losses consequently result. However, if the polymer chains are pulled to the extent that segmental rotations via which local deformations may result are prohibited, no traps will form and thus dramatic enhancement of quantum efficiencies should rise.

Although we are reporting the first discovery of this stretch-induced PL enhancement in conjugated polymers, it had been observed that charge conductivity in solid polyaniline films increased more than an order of magnitude when stretched [34]. Similarly, when confined in their rigid monomer crystals, the 1D quantum wires of single polydiacetylene chains demonstrate the absence of self-trapping [25-29]. Furthermore, recent measurements by confocal microscopy and single molecule spectroscopy on molecularly constrained MEH-PPV within a 3-4 nm thickness layer on strong-adhered substrate have revealed the substantially increased non-radiative lifetimes, likely resulted from suppression of the exciton-phonon interactions [47].

Moreover, the average binding energies of trapped polarons in ordinary MEH-PPV were reported to range from ~0.09 eV to 0.22 eV [14,17,18], comparable to the chain vibration energy (~0.2 eV) determined from photo-induced IR-active vibrations [17] and the gauch-trans energy barriers calculated for a model linear polymer (0.10 - 0.20 eV), consistent with the proposed Franck-Condon-type interpretation for the strain-induced effect.

The fact that this remarkable mechano-optoelectronic effect was not observed in the stretched films of concentrated MEH-PPV ( $c \geq 5.0\text{ wt.\%}$ ) suggests the strong influence of inter-molecular interactions on the energy loss pathways in this class of materials [8,11-13]. In addition, the so-called “molecular

“aggregates” may serve as quenchers of the photoinduced species. One important corollary of the mechano-optoelectronic interactions revealed here is the prospect of imposing properly designed molecular constraints for optoelectronic enhancement in conjugated polymers. Like stretching, many other effective means, such as ultrathin layer molecular adhesion [47], may also be used, thus offering new windows for developing efficient electronic devices based on polymers.

### **Conclusions:**

In summary, by exploiting the local deformation behavior of glassy polymer matrices, a large molecular constraint effect due to mechanical stretching was observed in the conjugated polymer MEH-PPV finely dispersed within-in. The PL efficiency was found enhanced considerably when the macromolecules were pulled beyond a threshold molecular strain ( $> 20\%$ ), then increasing with molecular strain to reach  $\sim 17$ -fold at  $\varepsilon = 300\%$ , and finally leveling off  $\sim 40$ -fold at  $\varepsilon = 530\%$ . In addition, the strain-induced PL enhancement is very sensitive to stress relaxation and the inter-chain energy dissipation. The results indicate that, when the chain segments are constrained by a large stress, the electron-phonon interactions inherent to the soft 1-D molecules reduce drastically due to the increased chain stiffness that hinders changes in local chain conformation and suppresses self-trapping of charges. This dramatic effect has important implications for both the basic understanding of the photoelectronic processes of conjugated polymers and the development of high efficiency devices based on the materials.

### **Acknowledgements:**

The authors benefit greatly from the discussions with Prof. Gunter Reiter of University of Freiburg, Germany, and Dr. Mark Geoghegan of University of Sheffield, U.K.. The work is supported by National Science Council (NSC) of Taiwan and a grant from the US Air Force (AOARD-084125) under the Taiwan NSC-US Air force Nanoscience Program.

### **References:**

- [1] A. G. MacDiarmid, A. J. Epstein, *Faraday Discuss. Chem. Soc.* **317** (1989).
- [2] J. H. Burroughes, D. D. C. Bradley, A. R. Brown, R. N. Marks, K. MacKay, R. H. Friend, P. L. Burns, A. B. Holmes, *Nature* **347**, 539 (1990).
- [3] C. Tanase, E. J. Meijer, P. W. M. Blom, D. M. de Leeuw, *Phys. Rev. Lett.* **91**, 216601-1 (2003).
- [4] T. Virgili, G. Cerullo, L. Luer, G. Lanzani, *Phys. Rev. Lett.* **90**, 247402-1 (2003).
- [5] N. Tessler, G. J. Denton, R. H. Friend, *Nature* **382**, 695 (1996).
- [6] M. Fox, *Optical Properties of Solids*, Oxford University Press, 2001.
- [7] Z. Vardeny, E. Ehrenfreund, O. Brafman, M. Nowak, H. Schaffer, A. J. Heeger, F. Wudl, *Phys. Rev. Lett.* **56**, 671 (1986).
- [8] M. Yan, L. J. Rothberg, F. Papadimitrakopoulos, M. E. Galvin, T. M. Miller, *Phys. Rev. Lett.* **72**, 1104 (1994).
- [9] Z. An, C. Q. Wu, X. Sun, *Phys. Rev. Lett.* **93**, 216407-1 (2004).
- [10] D. Moses, A. Dogariu, A. J. Heeger, *Synthetic metals* **116**, 19 (2001)
- [11] I. B. Martini, A. D. Smith, B. J. Schwartz, *Phys. Rev. B* **69**, 035204 (2004).
- [12] B. J. Schwartz, *Annu. Rev. Phys. Chem.* **54**, 141 (2003).
- [13] J.-L. Bredas, J. Cornil, D. Beljonne, D. A. Dos Santos, Z. Shuai, *Acc. Chem. Res.* **32**, 267 (1999).
- [14] K. D. Meisel, H. Vocks, P. A. Bobbert, *Phys. Rev. B* **71**, 205206 (2005).
- [15] M. G. Roe, J. M. Ginder, P. E. Wigen, A. J. Epstein, M. Angelopoulos, A. G. MacDiarmid, *Phys. Rev. Lett.* **60**, 2789 (1988).
- [16] M. Wohlgemann, W. Graupner, G. Leising, Z. V. Vardeny, *Phys. Rev. B* **60**, 5321 (1999).
- [17] T. Drori, E. Gershman, C. X. Sheng, Y. Eichen, Z. V. Vardeny, E. Ehrenfreund, *Phys. Rev. B* **76**, 033203 (2007).
- [18] E. Artacho, M. Rohlffing, M. Cote, P. D. Haynes, R. J. Needs, C. Molteni, *Phys. Rev. Lett.* **93**, 116401-1 (2004).
- [19] H.-F. Meng, T.-M. Hong, *Phys. Rev. B* **61**, 9913 (2000).
- [20] J.-L. Bredas, R. Silbey, *Science* **323**, 348 (2009).
- [21] E. Collini, G. D. Scholes, *Science* **323**, 369 (2009).
- [22] L. J. Rothberg, M. Yan, A.W.P. Fung, T. M. Jedju, E. W. Kwock, M. E. Galvin, *Synth. Met.* **84**, 537 (1997).

- [23] K. Pakbaz, C.H. Lee, A. J. Heeger, T.W. Hagler, D. McBranch, *Synth. Met.* **64**, 295 (1994).
- [24] R. Kersting, U. Lemmer, M. Duessen, H. J. Bakker, R. F. Mahrt, H. Kurz, V. I. Arkhipov, H. Bassler, E. O. Bobel, *Phys. Rev. Lett.* **73**, 1440 (1994).
- [25] F. Dubin, R. Melet, T. Barisien, R. Grousson, L. Legrand, M. Schott, V. Voliotis, *Nature Physics* **2**, 32 (2006).
- [26] H. Bassler, *Nature Physics* **2**, 15 (2006).
- [27] R. Lecuiller, J. Berrehar, J. D. Ganiere, C. Lapersonne-Meyer, P. Lavallard, M. Schott, *Phys. Rev. B* **66**, 125205 (2002).
- [28] T. Guillet, J. Berrehar, R. Grousson, J. Kovensky, C. Lapersonne-Meyer, M. Schott, V. Voliotis, *Phys. Rev. Lett.* **87**, 087401-1 (2001).
- [29] R. Lecuiller, J. Brrehar, C. Lapersonne-Meyer, M. Schott, *Phys. Rev. Lett.* **80**, 4068 (1998).
- [30] A. Cadby, R. Dean, R. A. Jones, D. G. Lidzey, *Adv. Mater.* **18**, 2713 (2006).
- [31] N. A. Iyengar, B. Harrison, R. S. Duran, K. S. Schanze, J. R. Reynolds, *Macromolecules* **36**, 8978 (2003).
- [32] D. A. Vanden Bout, W.-T. Yip, D. Hu, D-K. Fu, T. M. Swager, P. F. Barbara, *Science* **277**, 1074 (1997).
- [33] G. He, Y. Li, J. Liu, Y. Yang, *Appl. Phys. Lett.* **2002**, **80**, 4247.
- [34] A. J. Epstein, A. G. MacDiarmid, “The controlled electromagnetic response of polyanilines and its application to technologies”, p. 141 in W. R. Salaneck, D. T. Clark, E. J. Samuels (Eds.), *Science and Applications of Conducting Polymers*, Adam Hilger, New York, USA (1991).
- [35] T. W. Hagler, K. Pakbas, K. F. Voss, A. J. Heeger, *Phys. Rev. B* **44**, 8652 (1991).
- [36] S. Heun, R. F. Mahrt, A. Greiner, U. Lemmer, H. Bassler, D. A. Halliday, D. D. C. Bradley, P. L. Burn, A. B. Holmes, *J. Phys.: Condens. Matter* **5**, 247 (1994).
- [37] E. J. Kramer, *Advances in Polymer Science* **52/53**, 1 (1983).
- [38] E. J. Kramer, L. L. Berger, *Advances in Polymer Science* **92**, 1 (1990).
- [39] R. P. Kambour, *J. Polym. Sci. Macromol. Rev.* **7**, 1 (1973).
- [40] A. M. Donald, E. J. Kramer, *Polymer* **23**, 457 (1982).
- [41] A. C.-M. Yang, E. J. Kramer, *J. Polym. Sci.: Polym. Phys. Ed.* **23**, 1353 (1985).
- [42] A. C.-M. Yang, E. J. Kramer, C. C. Kuo, S. L. Phoenix, *Macromolecules* **19**, 2020 (1986).
- [43] A. C.-M. Yang, M. S. Kunz, J. A. Logan, *Macromolecules* **26**, 1776 (1993).
- [44] J. H. Lin, A. C.-M. Yang, *Macromolecules* **34**, 3698 (2001).
- [45] C.-C. Hsiao, T. S. Lin, L. Y. Cheng, C.-C. M. Mar, and A. C.-M. Yang, *Macromolecules* **38**, 4811 (2005).
- [46] C.-W. Lin, L.C. Huang, C.-C. M. Ma, A.C.-M. Yang, C.-J. Lin, L.-J. Lin, *Macromolecules* **41**, 4978 (2008).
- [47] C. W. Yang, *Master Thesis* 2006; B. J. Chen, *Master Thesis* 2010, Department of Materials Science and Engineering, National Tsing Hua University, Taiwan; B. J. Chen, et. al., “Massive Optoelectronic Enhancement of Conjugated Macromolecules Constrained by Dewetting Interfacial Interactions”, in submission.
- [48] J. Liu, T.-F. Guo, Y. Yang, *J. App. Phys.*, **91**, 1595 (2002).

## SECTION 2

### Large Optoelectronic Enhancement of Conjugated Macromolecules Constrained by Dewetting Interfacial Interactions

B. J. Chen<sup>1</sup>, C. W. Yang<sup>1</sup>, C. C. Chang<sup>1</sup>, P. W. Lee<sup>1</sup>, C. H. Tsao<sup>1</sup>, G. Reiter<sup>2</sup>, C. T. Yuan<sup>3</sup>, J. Tang<sup>3</sup>, T. L. Lin<sup>4</sup>, P. K. Wei<sup>3</sup>, A. C.-M. Yang<sup>1\*</sup>

<sup>1</sup>Department of Materials Science and Engineering, National Tsing Hua University, Hsinchu, Taiwan

<sup>2</sup>Institute of Physics, Albert-Ludwigs-Universität, Freiburg, Germany

<sup>3</sup>Research Center for Applied Sciences, Academia Sinica, Taipei, Taiwan

<sup>4</sup>Department of Engineering and Systems Science, National Tsing Hua University, Hisnchu, Taiwan

#### Abstract

The photoluminescence of a conjugated polymer, poly[2-methoxy-5-((2'-ethylhexyl)oxy)-1,4-phenylenvinylene] (MEH-PPV), manifested an enormous enhancement when contained in a film that dewetted and left an ultrathin residual layer on “exposed” substrate. This residual layer ( $\sim 3 - 5$  nm) was resulted from strong interfacial mechanical interactions during dewetting. The blue-shifted emission from the conjugated macromolecules constrained in the ultrathin layer eventually overwhelmed the film luminescence to result an enhancement factor greater than 15 fold. On the other hand, the emission from the rest of the film that contained relaxing chains underwent red shifting with only minor intensity changes. Single-molecule spectroscopy revealed that accompanying the efficiency enhancement the luminescence lifetime increased considerably and the characteristic blinking was effectively turned off. The large optoelectronic enhancement is attributed to the reduction of phonon-excitons interactions in the molecularly constrained polymer chains strongly adhesive to the substrate.

#### Introduction

Plastic optoelectronic devices [1-3] for energy or lighting have convincingly become one of the most anticipated breakthroughs to occur for a world facing stark challenges of commodity scarcity. This anticipation was anchored in the light of low material cost, ease of processing, and ample room for engineering of general polymeric systems, in addition to a long successful history of converting breakthroughs in polymer technology into broad industrial adaption. Nevertheless, present polymer technologies are still far from being able to deliver sufficient efficiencies that warrant practical applications. Emerging recently, however, that evidence of chain conformation effects points opportunities for revamping the efficiency landscape of the polymer-based devices [4-10]. The chain packing state and molecular constraints may significantly influence the optoelectronic efficiencies of polymers [7]. Along the same line, hereby reported is the extraordinary photoluminescence enhancement unleashed when conjugated polymer chains were molecularly constrained in ultrathin layers with thicknesses less than one tenth of their unperturbed molecular dimensions [11-12].

In further details, broadly employed in polymeric optoelectronics thin conjugated polymer films ( $< 100$  nm) are produced by spin coating in which molecular condensation is direct consequence of dynamic balance between rapid solvent evaporation, capillarity of the transient viscous film, and sluggish chain rearrangements. The existence of very large entropic molecular stresses [13-15] arising from deviation from thermal equilibrium of the frozen chains represents a sizable energy stored in the thin film to be released and drive the film toward local equilibrium via dewetting when in contact with high temperatures or plasticizing vapors. Amid the formation of droplets that contain relaxing chains during dewetting, a thermodynamically predicted very thin residual layer, of thickness  $h^*$ , develops in film-retreated regions. Although little has been known regarding the state of the  $h^*$  layer, the molecular chains therein are under great molecular constraints through confinement in a space less than one tenth of their molecular dimensions.

For conjugated polymers, the energy dissipation routes of the photo-induced charges (excitons) strongly depend on the inter-chain Coulomb interactions and the intrinsic segmental vibrations [4-6,16-18]. Thus, the quantum efficiency depends strongly on the molecular packing state in the thin film. For example, aggregation of molecular segments arising from  $\pi-\pi$  interactions was long

reported to substantially reduce the luminescent efficiencies. It is also clear that since strong covalent bonds exist only along the main chains, polymer molecules are intrinsically much softer than the inorganic crystalline counterparts, such as silicon and gallium oxide. Hence self-trapping of the excited charges to the soft chains due to interactions with chain vibrations (phonons) or deformations (time integrals of vibrations) would lead to hindered charge mobility and significantly retarded charge recombination efficiencies [19]. It was recently discovered that the photoluminescence efficiencies of a conjugated polymer increased dramatically when the chains were stretched and strain-hardened [7,19]. Rather than using crossheads to result stretching, the work reported here utilized the stored mechanical energy within thin polymer films to produce highly constrained states of conjugated macromolecules in the  $h^*$  layer by which an extraordinary efficiency enhancement was achieved. This approach is compatible with the microelectronic processes and may pave the way toward fabrications of high efficient plastic optoelectronic devices.

### **Experimental Section**

The polymer poly[2-methoxy-5-((2'-ethylhexyl)oxy)-1,4-phenylenevinylene], MEH-PPV, was purchased from Sigma-Aldrich Chemical Co., with  $M_w$  125,000~250,000 g/mol with polydispersity ( $M_w/M_n$ ) around 5. The polystyrene (PS) was bought from Pressure Chemical Co. with a molecular weight of  $M_w = 2,032$  and  $M_w/M_n = 1.06$ . A solvent blend of equal parted toluene (HPLC/SPECTRO, TEDIA), tetrahydrofuran (THF, anhydrous, TEDIA), and cyclohexanone (GC grade, Sigma-Aldrich) was used to dissolve the MEH-PPV polymer or mixture of MEH-PPV and PS. The blend (MEH-PPV/PS) was composed by 1:3 mass ratio of MEH-PPV to PS. The solution was stirred slowly at 50°C for 12 - 24 hours and filtered (0.45  $\mu\text{m}$  pore size) to remove any non-dissolved particles in solution. The polymer solution was then spin-casted on 1 cm  $\times$  1 cm substrate. By adjusting the spin speed, the film thicknesses were controlled at 20, 40, and 60 nm. The substrate is either the bare silicon wafer that came with a thin native oxide (1-3 nm) on the top or silicon wafer coated with a low energy rubber of polydimethylsiloxane (PDMS: Sylgard 182, Dow Corning). The PDMS was spin-coated from toluene solution followed by curing at 130°C for 25 minute. The thickness of silicone was around 3 nm for the pure MEH-PPV film and less than 1 nm for the MEH-PPV/PS film.

The prepared polymer films were generally smooth and uniform although those spun from solutions of higher MEH-PPV concentrations tended to have more local slumps in the films. After preparation, the samples were always protected in aluminum foil wrappings before being tested. Some control samples were prepared in a glove box (MBraun, Germany) but their testing results were essentially identical to that prepared in the ambient conditions.

The films were then annealed in a vacuum oven at a temperature between 100 - 130°C, during which the film morphology and the luminescence spectra were monitored and recorded. Optical microscope and atomic force microscope was used to record the film morphological information. A fluorescence spectrometer (Perkin Elmer) was used to measure the photoluminescence spectra. For single-molecule spectroscopy, time-resolved confocal microscope (PicoQuant MT 200) was used with an excitation at ~460 nm by a pulsed diode laser (~80 ps pulse width). The excitation was focused to diffraction limit by microscope objective and the fluorescence was collected by the same objective and guided into a confocal pinhole (50 micron in diameters) and detected by single photon avalanche photon diodes. Time-tagged, time-resolved measurements based on time-correlated single-photon counting technique were performed during single-molecule detection to obtain the fluorescence decay profiles [20-21]. Photoluminescence mapping of the dewetted film was also done by utilizing a scanning near-field optical microscope. In order to explore the thickness of the residual monolayer of dewetted films, x-ray reflectivity method using the synchrotron radiation (National Synchrotron Radiation Research Center,  $\lambda = 0.154982$  nm) was employed. The specular reflectivity was measured and fit to a multilayered model following the Abeles formulation [22-23]. From the fitting, the fine structure of the dewetted film was obtained.

### **Results and Discussions**

The MEH-PPV thin films underwent dewetting when annealed at a temperature between 100 and 130°C on PDMS-coated silicon wafer. The dewetting took place following a heterogeneous nucleation and growth mechanism in which small pinholes emerged after a first period of annealing around 1hour and then continued to evolve into a fully developed droplet pattern after 5 hours (for the 20 nm films, Figures 1a and b). The required annealing times became significantly longer for thicker films (Figures

1a and b) and for the films on bare silicon, due to the effects of varied molecular recoiling stresses as well as the influences of long range van der Waals interactions between the substrate and free surface [11,14,15,24-26].

The dewetting of the conjugated polymer films induced an extraordinarily large photoluminescence enhancement, as shown in Figure 1c. The enhancement factor estimated from the peak intensities ranged from 2 to 14 fold, depending on the film thickness (Figure 1c). For 20 nm MEH-PPV films, close examination revealed that a blue-shifted new peak (at 543 nm) emerged simultaneously with the appearance of the dewetting holes, and the new peak remained approximately unchanged throughout the dewetting. Before dewetting, the intra-chain and inter-chain emissions were resolved from the spectrum to be 565 nm and 595 nm, respectively, by Gaussian curve fitting, and these are very close to those reported elsewhere [27]. It was found that all the spectra were best analyzed by assuming unchanged wavelengths of these emissions during dewetting (Appendix A). From the results, the temporal variations of these peak intensities were obtained and are shown in Figure 2a. Clearly seen, the new peak increased rapidly in intensity with dewetting while the original emissions of the intrachain and interchain emissions underwent only relatively minor variations. Similar behavior was observed for the 60 nm MEH-PPV films although the development of the new peak was not as prominent as for the thinner films.

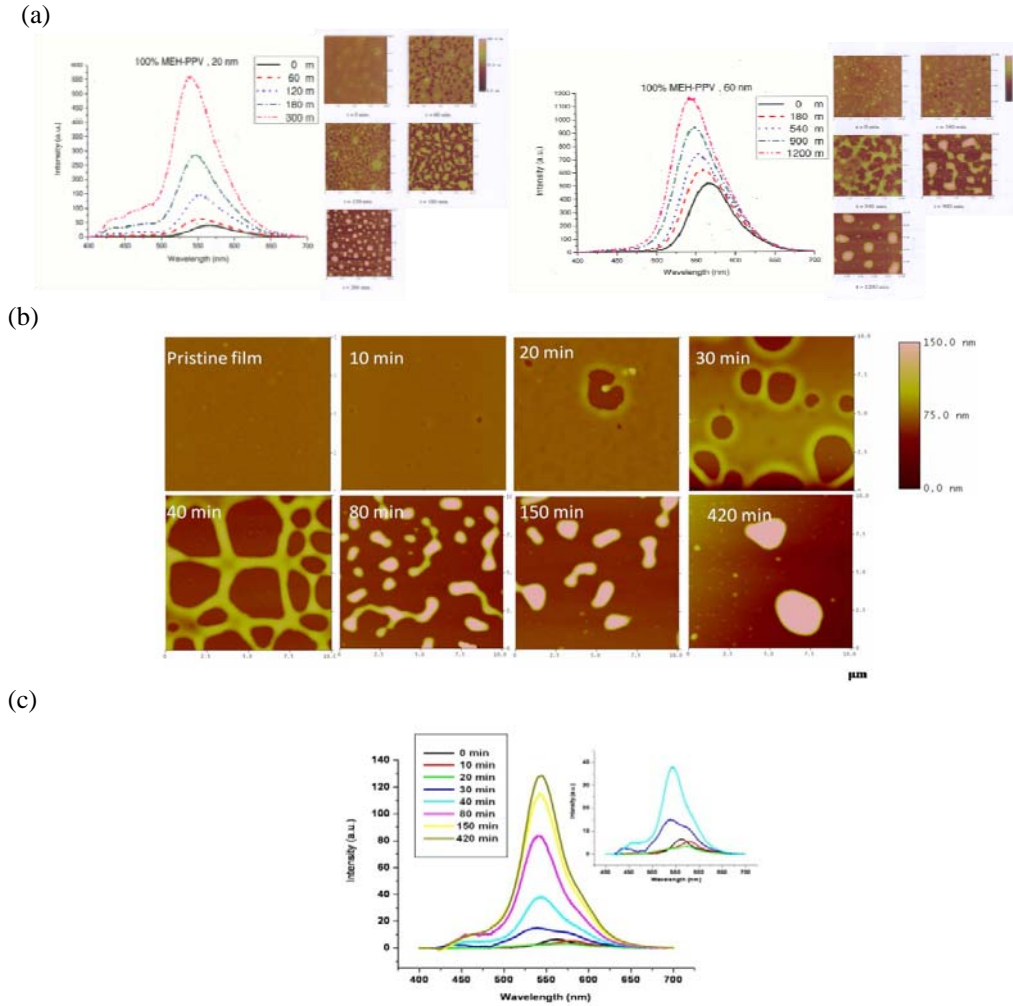


Figure 1. Topographic evolution and luminescence spectra of dewetted thin films: a) 20 and 60 nm MEH-PPV films, and b,c) 20 nm MEH-PPV/PS films.

Also shown in Figure 1 are the topographic and luminescent properties of the dewetting

MEH-PPV/PS films. These plasticized films dewetted with much faster speeds and the apparent ultimate luminescent enhancement was even greater, at around 19 fold. At 10 min, holes of  $\sim$  100 nm in diameter emerged, which grew to several microns at 30 min. These holes coalesced at 40 min and the ridges started to break at 80 min. A full dewetted droplet pattern was formed at around 420 min. The resolutions of the intra-chain emission, interchain emission, and the new peak are shown in Appendix A. Similarly to that in the undiluted MEH-PPV films, a new peak emerged at around 543 nm after the holes had nucleated, and increased in intensity continuously with dewetting (Figure 2b). The variations of the intrachain (560 nm) and interchain emissions (600 nm) are comparatively much smaller; the increases of both are related to the continuous dissolution of MEH-PPV molecules in the short chain PS.

A brief examination over the dewetting film by using near field scanning optical microscope (NSOM) had revealed considerably stronger luminescence emitting from the regions within of holes as compared to that from outside the holes (Figure 3c). Furthermore, detailed AFM topographic analysis (Figure 3d) revealed that the depth of all dewetting holes were smaller than 16 nm despite the film thickness was 20 nm. Under a confocal microscope, this monolayer emitted brightly when the focal plane was near the surface of the substrate (Figure 3b). All this illustrates that there was a residual layer of polymer with a thickness around 4 nm behind the retreating dewetting holes (Figure 3a), and this residual layer was responsible for the new emission peak at  $\sim$  540 nm that increased in intensity with the progress of dewetting. As a further proof, the area coverage of the residual layer was determined from bearing ratio analysis on the AFM topography results and it was found that the increasing of the residual layer area with the dewetting time was in perfect synchronization with that of the new peak intensity (Figures 2).

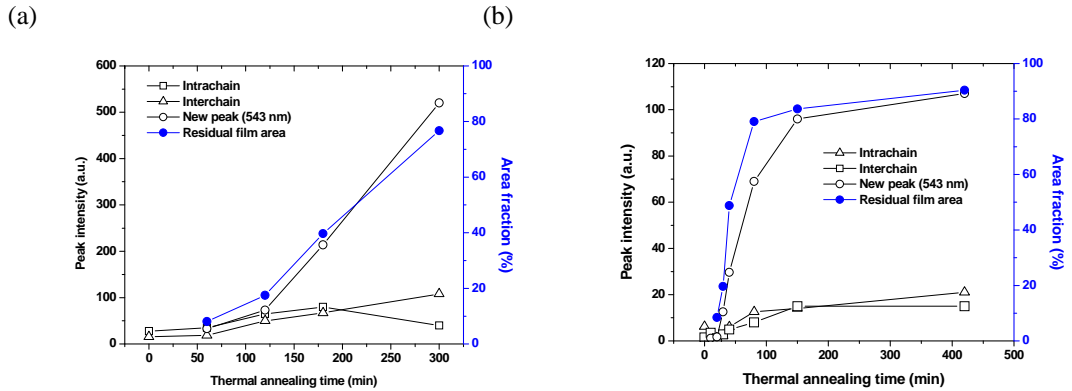


Figure 2. Emission intensities of the resolved peaks and the residual layer area fraction versus dewetting time for the 20 nm a) MEH-PPV films and b) MEH-PPV/PS films.

The thickness of the residual MEH-PPV was further measured by x-ray reflectivity using synchrotron radiation fitted with a multilayer model [22,23]. The multilayer model, as shown in Appendix B, is constructed by a first layer of the polymer droplets and air, a second layer of the residual polymer layer, a third layer of the silicone overcoat, a fourth layer of the native oxide on the silicon wafer, and a fifth layer of the silicon wafer. The thickness, roughness, and scattering length density of each layer were required to fit the specular reflectivity data using the Abeles formulation [22,23]. The morphological information acquired by using AFM was useful guides for the fitting simulations. The fitting results indicate that there was a 5.5 nm (roughness  $\sim$  1.5 nm) residual layer of the fully dewetted 20 nm MEH-PPV films. For the 20 nm MEH-PPV/PS films, a residual layer of 3.9 nm thick with 0.2 nm roughness was resulted, in excellent agreement with the AFM measurements shown in Figure 3d.



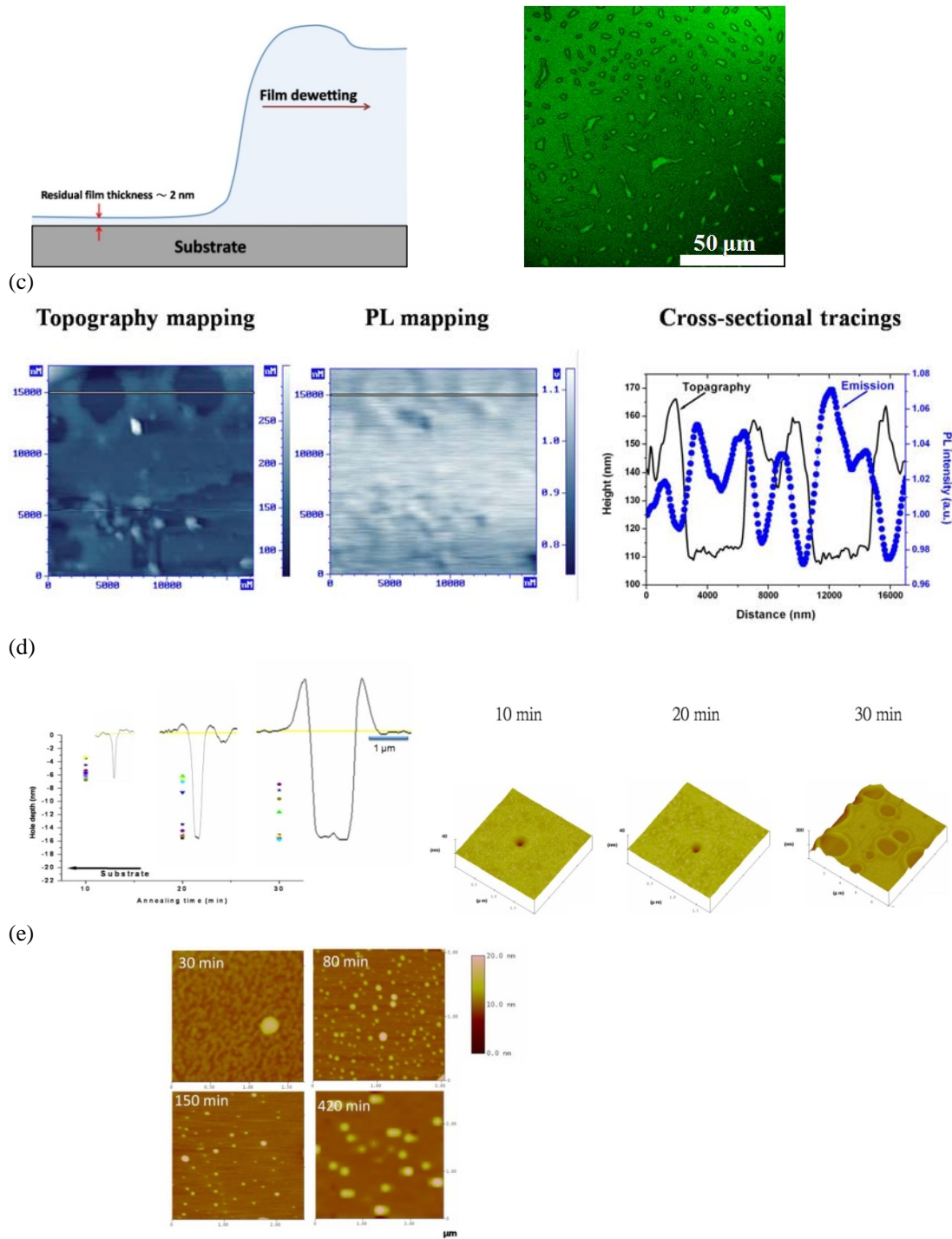


Figure 3. a) Schematic depiction of the residual layer from dewetting. b) A confocal luminescent micrograph on the dewetted region with focused on the vicinity of the residual layer. c) NSOM survey on the dewetted MEH-PPV film. d) The cross-sections of the dewetting holes that show the existence of a residual polymer layer on the retreated surface. e) The topography of the residual layer continued to evolve with annealing time.

Closely related to the existence and molecular state of the residual layer, continuous coarsening of the droplets was observed even when the islands had well developed (Figures 1a and b). This indicates some effective mechanical linkages between these dewetted droplets that had enabled the

large scale mass transfer of the giant MEH-PPV molecules (unperturbed molecular sizes  $\sim$  30 nm) over a distance on length scales  $\sim$  10 microns. The continuous evolution of the film morphology, including that of the residual layer, beyond island formation clearly had resulted in further increase of the new emission peak (Figure 1).

Further exploring into the physical origin of the residual layer, the dewetting process undoubtedly are initiated by the dominant residual stress arising from the entropic molecular recoiling of frozen chains in the film. This recoiling stress, estimated to be around  $10^4$  greater than the long-range van der Waals interactions [14], undergoes relaxation as the film are annealed over long period of times in a temperature that provides enough thermal activations to the chain segments [15]. In the wake of stress dissipation when the film evolve into droplets, the van der Waals force finally takes the rein and dominates the evolution of the polymeric system. This residual layer of  $h^*$  thickness, well-predicted thermodynamically on the basis of the long range capillary interactions [28], is readily observed owing partly to the topological connections within macromolecules that reduce molecule evaporation and thus lead to its stable existence in the ambient condition.

Other than the thermodynamic basis for its development, the formation of the residual layer obviously was strongly influenced by the specific interactions between the dewetting polymer films and the substrates. In this regard, the interfacial adhesion and friction, as well as the molecular recoiling stress [11,13-15] and the mechanical coupling between the film and the substrate [15] are important. [28]. Effect of the surface Hamaker constant on the residual layer formation, which is being studied, is beyond the scope of this paper.

The topography of the residual layer in MEH-PPV/PS was further studied by using AFM. It was shown that the freshly created residual layer demonstrated a complex surface structure that featured small “winding lumps” around 50 nm in lateral width (Figure 3a). This structure quickly evolved into small droplets of lateral diameter around 50 nm emerging from a smoothed platform, and these droplets underwent coarsening as dewetting continued. The above process (Figure 3a) resembled an equilibrating process of the metastable residual layer that was created under the extremely large interfacial frictional deformations. Mimicking a smaller scale dewetting, the metastable winding lumps evolved into a thermodynamically more stable state during the ensuing annealing that features smoother surface, lower film thickness that approached closer to the theoretical  $h^*$  [28], and the emergence of local droplets that contained the relaxed polymer chains.

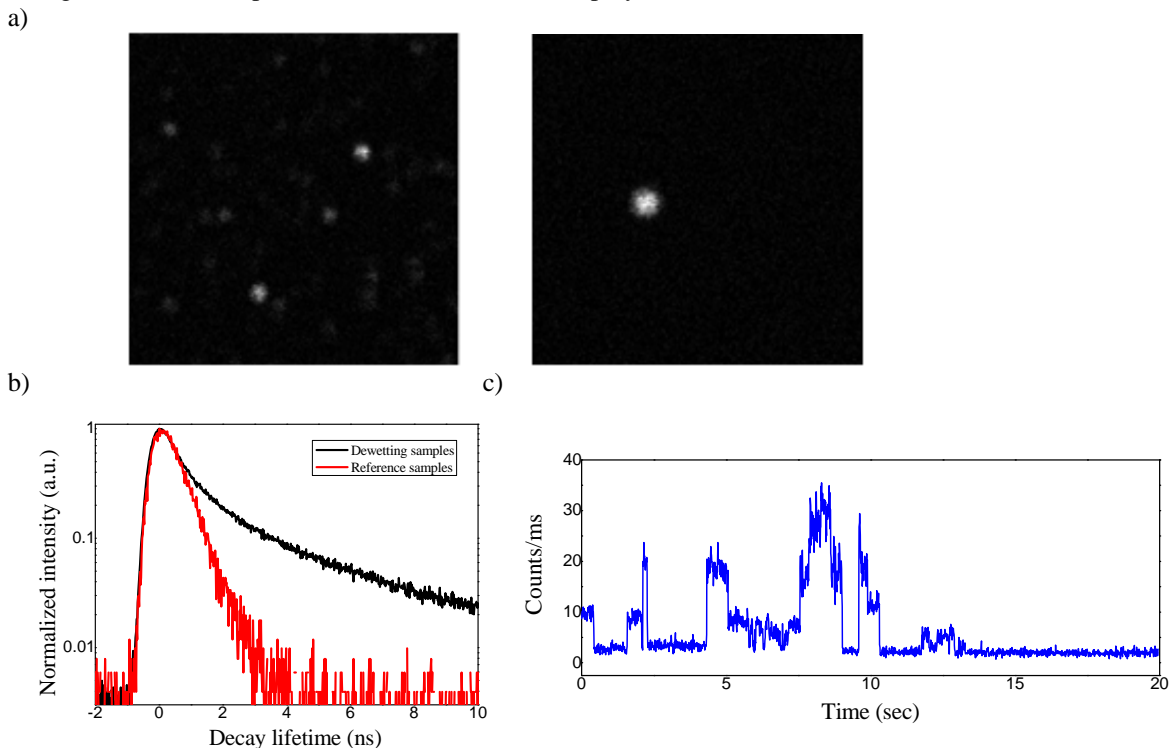


Figure 4. a) Single molecules emitting lights from the as-deposit film before dewetting (left

micrograph) and the residual layer of the dewetted region (right micrograph). b) Decaying characteristics of the single molecule luminescence corresponding to a). c) Blinking of the MEH-PPV single molecule before dewetting. No blinking of the molecules in the residual film.

It is important to note that polymer films underwent dewetting upon contact of plasticizing agents [29-31] and may produce the similar enhancement effect on the photoluminescence. However, the enhancement effect was generally lower in the “solvent annealing” experiments, which was attributed to the reduced friction and increased chain relaxation in the solvent-rich environment [31].

Single molecule spectroscopy [8-10,20,21] was employed to investigate the effect of dewetting on the luminescent characteristics of the conjugated polymer. In this experiment, trace amount ( $10^{-9}$  concentration) of MEH-PPV was added into the PS (Mw = 2k g/mol.) for preparing the spin coated thin films that was then forced to dewet. Before dewetting, a relatively large amount of luminescent emitting spots with sizes on the screen smaller than the optical resolution limit (~ 0.3 microns) were observed to populate across the film (Figure 4a, left). These lighting spots illustrated blinking when the intensity was recorded versus time (Figure 4c). In the dewetted film, similar images were observed in the droplets areas with the number density of the lighting spots dramatically increased. In the residual layer region between droplets, the number of lighting spots decreased considerably but the emissions are much brighter (Figure 4a, right). This is consistent with the large shear extension in the residual layer that significantly reduces the number of single molecules and the observed large photoluminescent enhancement. Furthermore, in contrast to the ordinary single molecules, these stretched in the residual layer did not show any blinking. The luminescence lifetime was observed to increase substantially in the residual layer (Figure 4b), a result possibly contributed by the increase of non-radiative lifetimes stemming from hindrance of phonon interactions in these molecular constrained molecules.

The deformation-induced optoelectronic efficiencies observed here are in excellent agreement with that observed in the strain-hardened conjugated macromolecules highly diluted in glassy polymers [7]. The extraordinarily large optoelectronic enhancements induced by chain hardening by stretching had been attributed to the effective molecular constraints imposed on the otherwise soft polymer chains. When the conjugated polymer chains are fully stretched to the strain-hardened state, self-trapping of the photo-excited charge was significantly depressed due to the dramatically increased local chain stiffness, thus charge recombination to produce luminescence was made much more efficient than in the relaxed state. The macromolecules confined in the residual layer behind the dewetting fronts were effectively constrained in the extremely deformed state by the large adhesion and frictional force stemming from interaction with the substrate. Thus, the strain-hardened effect prevailed to give rise to the very large optoelectronic enhancement. In the stretch-induced experiment, however, blue shifts were not observed to accompany with the efficiency enhancement. Thus, the blue shifts observed of the new peak from the residual layers were arising from the further separation of the conjugated molecules stemming from the large accumulated deformation from long distance dragging associated with droplet formations. The molecular separation induced blue shift is consistent with the dilution effect of PS in the MEH-PPV/PS blend relative to the pristine MEH-PPV films as discussed earlier and presented in Figure 1.

Finally, the large optoelectronic enhancement by thin film dewetting may find useful applications in the energy and lighting devices as the thin film processes involved are fully compatible with the current prevailing technology for microelectronics and display industries. This assessment is particularly true when the dewetting is carried out by solvent imbibing in a multilayer fashion.

## Conclusions

The photoluminescence of the thin polymer film containing a conjugated polymer MEH-PPV manifested dramatic enhancement upon annealing when the film dewetted and formed an ultrathin residual polymer layer on the “exposed areas”. A new emission peak emerged at a wavelength approximately 20 nm blue-shifted relative to the original film emission with the luminescent intensity increased in sync with the increase of the residual layer area. The emission from the residual layer may eventually overwhelm the total emission to give a luminescent enhancement greater than 19 fold in the 20 nm MEH-PPV/PS films. The luminescent enhancement depended on film thickness, conjugated polymer concentration, and the substrate surface properties. In contrast, the luminescence from the result of the film underwent red shifting with only modest intensity changes during the

dewetting process. The residual layer, with a thickness around 3 – 5 nm as determined from AFM and specular x-ray reflectivity, developed under the strong influences of surface capillary interactions and a chain conformation effect. The macromolecules within the residual layer were extensively deformed and thus molecularly constrained. Single molecule spectroscopy indicated that along with the extraordinary enhancement the lifetime of the luminescence increased significantly with the blinking characteristic turned off in the residual layer. The large optoelectronic enhancement is attributed to the retarded phonon-excitons interactions in the molecularly constrained conjugated polymer chains.

### Acknowledgements

The authors greatly appreciate the instructive discussions with Dr. Mark Geoghegan of University of Sheffield, U.K., Prof. J. H. Hsu of National Sun Yat Sen University, Kaohsiung, and Prof. Jonathan White of University of Yuanze, Chungli, Taiwan. The work is supported by National Science Council of Taiwan (NSC 98-2120-M-007-010-; NSC 96-2628-E-007-020-MY3) and grants from the US Air Force (AOARD-084125, -094024) under the US Air force-Taiwan NSC Nanoscience Initiatives.

### References

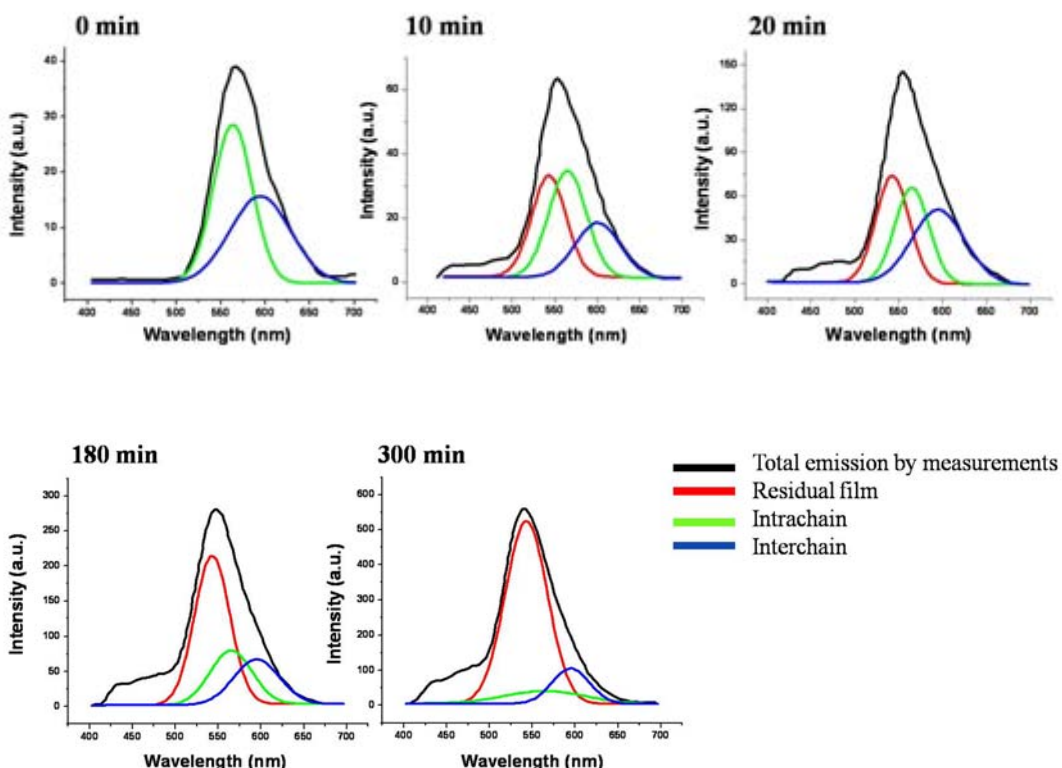
- [1] G. Gustafsson, Y. Cao, G. M. Treacy, F. Klavetter, N. Colaneri, and A. J. Heeger, *Nature* **357**, 477(1992).
- [2] D. Braun, A. J. Heeger, *Appl. Phys. Lett.* **58**, 1982 (1991).
- [3] M. Berggren, O. Inganäs, G. Gustafsson, J. C. Carlberg, J. Rasmusson, M. R. Andersson, et al, *Nature* **372**, 44 (1994).
- [4] G. He, Y. Li, J. Liu, Y. Yang, *Appl. Phys. Lett.* **80**, 22 (2002).
- [5] H.-L. Chou, S.-Y. Hsu, P.-K. Wei, *Polymer* **46**, 4967 (2005).
- [6] T.-Q. Nguyen, V. Doan, B. J. Schwartz, *J. Chem. Phys.* **110**, 8 (1999).
- [7] K. P. Tung, *Master Thesis*, 2008, Department of Materials Science and Engineering, National Tsing Hua University, Taiwan; K. P. Tung, B. J. Chen, C. H. Tsao, T. M. Hong, K. C. Hwang, A. C.-M. Yang, “Large Optoelectronic Enhancement Induced by Molecular Stretching in Conjugated Single Molecule Polymers”, in submission.
- [8] P. F. Barbara, A. J. Gesquiere, S.-J. Park, Y. J. Lee, *Acc. Chem. Res.* **38**, 602 (2005).
- [9] J. Yu, R. Lammi, A. J. Gesquiere, P. F. Barbara, *J. Phys. Chem. B* **109**, 10025 (2005).
- [10] J. Yu, D. Hu, P. F. Barbara, *Science* **289**, 1327 (2000).
- [11] Y. L. Chang, *Master Thesis* 2008, Department of Materials Science and Engineering, National Tsing Hua University, Taiwan; A. C.-M. Yang, Y. L. Chang, Y. Chien, Y. H. Chang, G. Reiter, “Molecular Stresses in Metastable Ultrathin Polymer Films Prepared by Spin Coating”, to be submitted. .
- [12] C. W. Yang, *Master Thesis* 2006, Department of Materials Science and Engineering, National Tsing Hua University, Taiwan.
- [13] G. Reiter, M. Hamieh, P. Damman, S. Sclavons, S. Gabriele, T. Vilmin, and E. Raphael, *Nat. Mater.* **4**, 754 (2005).
- [14] M. H. Yang, S. Y. Hou, Y. L. Chang, A. C.-M. Yang, *Phys. Rev. Lett.* **96**, 066105 (2006).
- [15] S. Al Akhrass, G. Reiter, S. Y. Hou, M. H. Yang, Y. L. Chang, F. C. Chang, C.F. Wang, A.C.-M. Yang, *Phys. Rev. Lett.* **100**, 178301 (2008).
- [16] M. Yan, L. J. Rotherberg, E. W. Kwock, and T. M. Miller, *Phys. Rev. Lett.* **75**, 1992 (1995).
- [17] J.-L. Bredas, J. Cornil, D. Beljonne, D. A. Dos Santos, and Z. Shuai, *Acc. Chem. Res.* **32**, 267 (1999).
- [18] Z. An, C. Q. Wu, and X. Sun, *Phys. Rev. Lett.* **93**, 216407-1 (2004).
- [19] M. Fox, *Optical Properties of Solids*, Oxford University Press, 2001.
- [20] C. T. Yuan, P. Yu, and J. Tang, *Appl. Phys. Lett.* **94**, 243108 (2009).
- [21] C. T. Yuan, P. Yu, H. C. Ko, J. Huang, and J. Tang, *ACS Nano* **3**, 3051 (2009).
- [22] A. Nelson, *J. App. Cryst.*, **39**, 273 (2006).
- [23] O. S. Heavens, *Optical Properties of Thin Films*, Butterworth, London (1955) (?)
- [24] G. Reiter, *Phys. Rev. Lett.* **68**, 75 (1992).
- [25] A. Sharma, and G. Reiter, *J. Coll. Interf. Sci.* **178**, 383 (1996).
- [26] P.-G. de Gennes, F. Brochard-Wyart, and D. Quere, *Capillarity and wetting phenomena :drops, bubbles, pearls, waves*, New York, Springer (2004).

- [27] J. Liu, T.-F. Guo, Y. Yang, *J. App. Phys.*, **91**, 1595 (2002).
- [28] R. Seemann, S. Herminghaus, and K. Jacobs, *Phys. Rev. Lett.*, **86**, 5534 (2001).
- [29] S. H. Lee, P. J. Yoo, S. J. Kwon, and H. H. Lee, *J. Chem. Phys.* **121**, 4346 (2004).
- [30] L. Xu, T. Shi, and L. An, *J. Chem. Phys.* **129**, 044904 (2008).
- [31] B. J. Chen, *Master Thesis* 2010, Department of Materials Science and Engineering, National Tsing Hua University, Taiwan; C. H. Wang, B. J. Chen, P. W. Lee, Y. S. Wang, Y. W. Liu, T. S. Lin, A. C.-M. Yang, “Control of Mechanical Energy Release for Extraordinary Optoelectronic Enhancement in ultrathin Polymer Films by Solvent Dewetting”, to be submitted.

#### Appendix A:

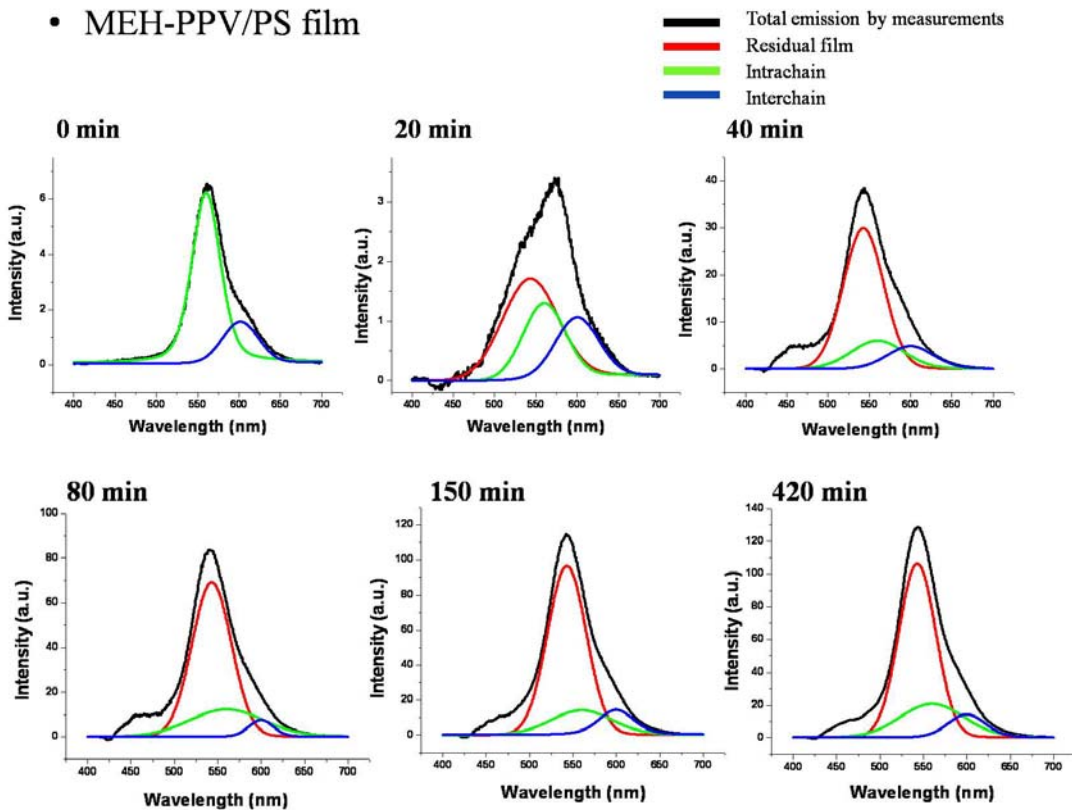
Each spectrum of the dewetting films shown in Figure 1a was resolved by fitting the Gaussian peaks centered at 565nm (intrachain emission), 595 nm (interchain emission), and 543 nm (the new peak). For the films before dewetting, only the 565 nm and 595 nm curves were used for the fitting. The results of the analyses are shown in the following.

- MEH-PPV film



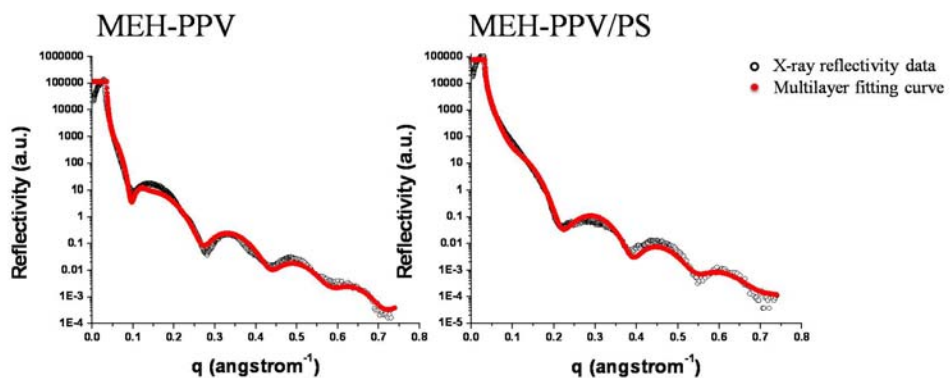
The spectra shown in Figure 1c for the blend MEH-PPV/PS were resolved according to the intramolecular (560 nm), intermolecular (600 nm), and residual layer emissions (543 nm) as follow.

- MEH-PPV/PS film



## Appendix B:

Specular x-ray reflectivity data were acquired and analyzed by using a multilayer model with the Abeles formulation [24-26] for the dewetted MEH-PPV (20 nm, 38 hrs at 130°C) and the MEH-PPV/PS films (20 nm, 7 hrs at 100°C). The morphological information acquired by using AFM was used as guides for the fitting. For the fully dewetted 20 nm MEH-PPV films (38 hrs at 130°C), the average droplet height determined from AFM was around 65 nm. The droplet volume fraction from bearing ratio analysis was calculated to be around 6.06%. The scattering length density (SLD) of the first layer was calculated to be 0.551 from  $\rho_{\text{1st layer}} = \rho_{\text{MEH-PPV}} \times \text{volume fraction}$  ( $\text{SLD}_{\text{MEH-PPV}} = 9.09$ ,  $\text{SLD}_{\text{PS}} = 9.52$  from the Database). For the MEH-PPV /PS film (7 hrs at 100°C), the droplet height and volume fraction were 385 nm and 4.11%, respectively. The SLD was calculated to be 0.386 based on volume ratio of the blend. The simulated curves fit well with the original data. The results are summarized in the tables that follow.



| Layer               | Thickness (nm)       |                | SLD ( $10^{-6} \text{A}^0$ ) |                | Roughness ( nm) |                |
|---------------------|----------------------|----------------|------------------------------|----------------|-----------------|----------------|
|                     | AFM                  | Fitting result | Database                     | Fitting result | AFM             | Fitting result |
| MEH-PPV<br>droplets | 64.856               | 62.554         | 0.551                        | 0.6            | 6.853           | 7              |
| Residual film       | Difficult to measure | 5.5            | 9.09                         | 7.1151         | 0.5             | 1.5            |
| Silicone            | 3 nm                 | 0.87733        | 9.706                        | 6              | 0.129           | 0.2            |
| Silicon oxide       | 2~3 nm               | 3.5414         | 18.9                         | 14.162         | 0.35            | 0.39273        |

| Layer                  | Thickness (nm)       |                | SLD ( $10^{-6} \text{A}^0$ ) |                | Roughness ( nm) |                |
|------------------------|----------------------|----------------|------------------------------|----------------|-----------------|----------------|
|                        | AFM                  | Fitting result | Database                     | Fitting result | AFM             | Fitting result |
| MEH-PPV/PS<br>droplets | 384.88               | 356.7          | 0.4                          | 0.39563        | 29.139          | 29.835         |
| Residual film          | Difficult to measure | 3.9            | 9.48                         | 6.2321         | 0.86            | 0.34765        |
| Silicone               | <1 nm                | 0.19414        | 9.706                        | 6.9781         | 0.129           | 0.13           |
| Silicon oxide          | 2~3 nm               | 1.0701         | 18.9                         | 17.023         | 0.35            | 0.2927         |

## SECTION 3

### Confocal Micro-Photoluminescence Study of Dewetted Thin Films Containing Conjugated Polymer MEH-PPV

Peiwei Lee, Wei-Chen Li, Yi-Chien, Chih-Hong Chang, Po-Tsun Chen, Ya-Hui Yang, Arnold Chang-Mou Yang\*

Department of Materials Science and Engineering, National Tsing Hua University, Hsinchu 300, Taiwan

#### Abstract

Photoluminescence (PL) of dewetted thin films of the conjugated polymer MEH-PPV diluted in the optically inert polystyrene matrix was studied by using a confocal laser spectroscope integrated with an atomic force microscope. Consistent with the far-field PL spectroscopic measurements obtained before, the confocal results also illustrated similar massive PL enhancements in the dewetted films. It was revealed, however, that not only the residual layer on the exposed substrate but also the droplets showed strong PL enhancement although the former illustrated even stronger PL efficiencies than the latter. The blue-shift of the intra-chain emission of the dewetted film was found to be from mostly the droplets, not the residual layer. The PL efficiency of the residual layer was found to be independent of the substrate despite the fact that the residual layer was only ~3nm in thickness over which injection of charges from decomposed excitons was observed in the as-spun films. This indicates that when the PL efficiency was substantially enhanced, excitation formation was suppressed, and so did the charge injection at the interface.

#### Introduction:

Conjugated polymers have attracted intensive research in recent years because of their potential applications in many important fields, such as light emitting diodes, lasers, displays, and photovoltaic cells.[1-3] Recent discoveries have revealed the existence of strong effects of chain packing and conformation that may revolutionarily revamp the efficiency landscapes of polymer-based devices [4-6]. Recently we have discovered that by dewetting a thin polymer films that contain conjugated polymer MEH-PPV a huge PL enhancement can be resulted [7]. This dewetting-induced PL enhancement was attributed to the formation of a residual layer on the exposed substrate and the accompanied blue shift of the enhanced PL was attributed to the effect of molecular separation in the residual layer. The PL enhancement was found to be strongly dependent on the substrate, a result previously ascribed to variation of the dewetting processes due to distinct substrate van der Waals force that resulted different substrate shearing lengths. Furthermore, unique thickness effect on the PL of the as-spun ultrathin films before dewetting was observed, which was attributed to the combination effect of chain conformation and charge injection at the silicon substrate. In this report, we tried to explore the micro-PL behavior of the dewetted films to unveil the origins underlying these observations.

#### Experimental Processes:

Thin films of 10% MEH-PPV diluted in 90% polystyrene (PS) were prepared by spin coating from the polymer solution in a solvent composed of equal parts toluene, cyclohexanone and THF. The MEH-PPV(MW= 150K~250K) was purchased from Aldrich Chemical Company and the polystyrene (MW= 2K) was bought from the Pressure Chemical Company. After stirring for one day, the solution was used for spin coating the solid films at 5000 rpm on silicon wafer and glass slips. The film thickness was measured by using an atomic force microscope and controlled at around 30 nm. After spin coating, the thin films were dried in vacuum for approximately 12 hours before use. The dewetting experiment was conducted in a vacuum oven at 130C.

Optical microscopy (OM) and atomic force microscopy (AFM) were used to unveil the film topography as a function of dewetting time. Photoluminescence spectra were obtained with a fluorescence spectrometer (Perkin Elmer). Micro-photoluminescence spectra of specific features on the dewetted films, particularly the residual layer and droplets, were recorded by the confocal system excited by a 473 nm laser. The confocal measurements of the dewetting features followed three steps as shown in Figure 1 to prevent the focus effect.

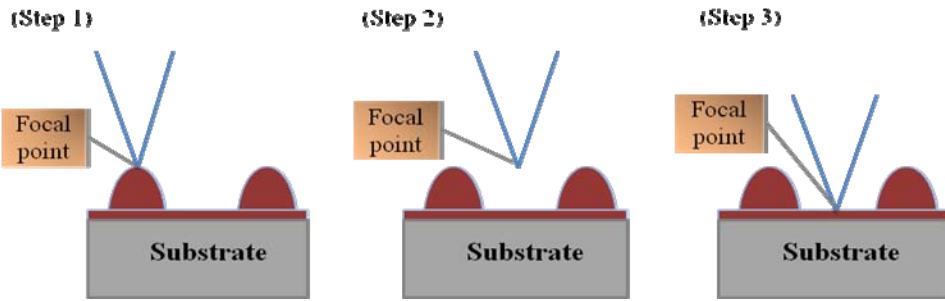


Figure 1. Steps taken for the micro-photoluminescence measurement of the dewetted films using the confocal laser system.

### Result and discussion:

The AFM topography of the dewetted film as a function of dewetting time was shown in Figure 2.

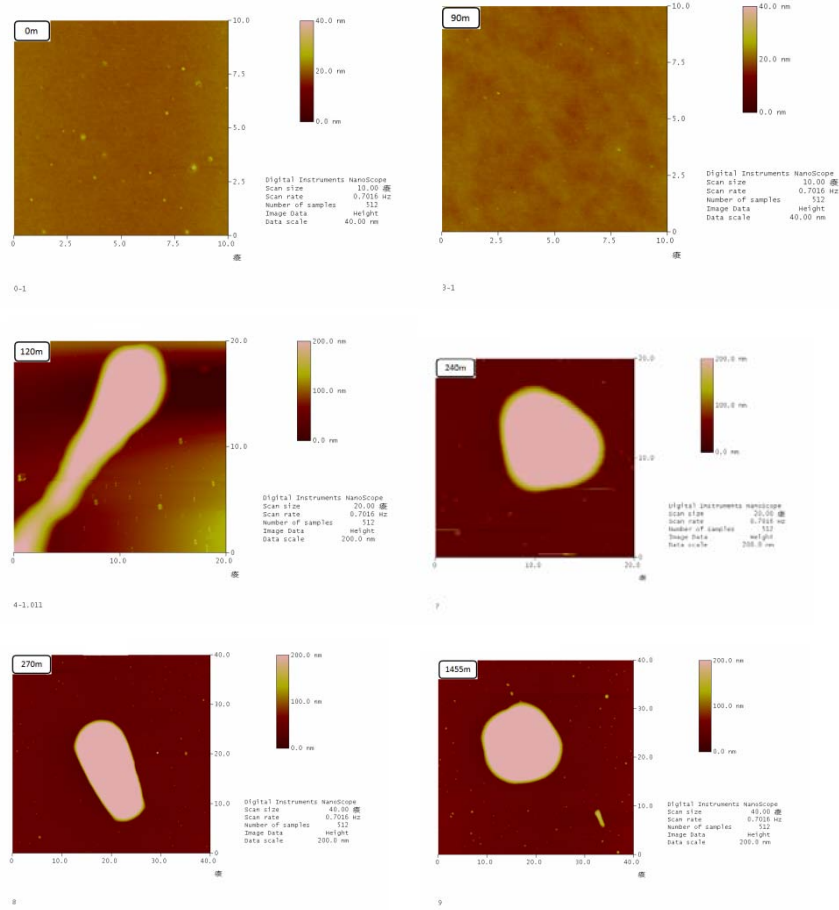
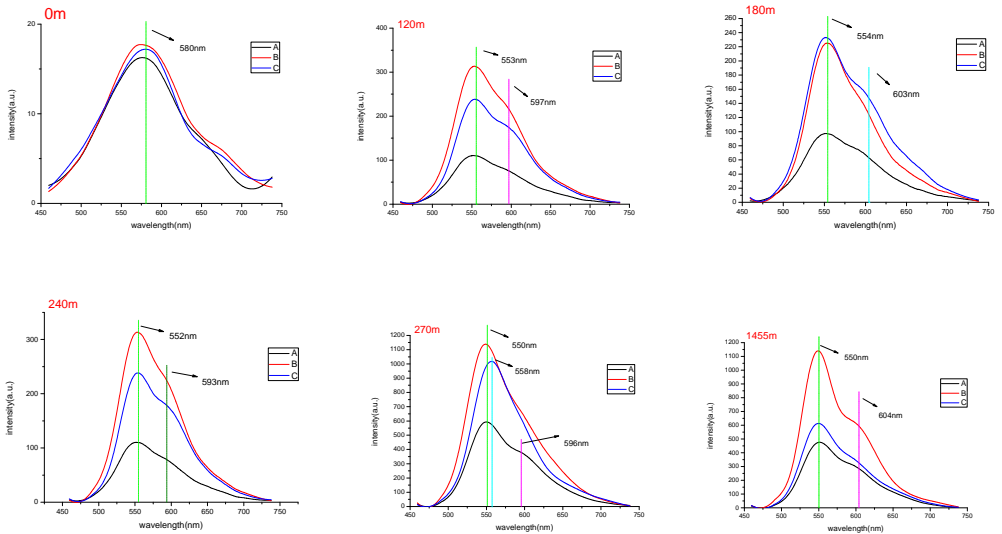


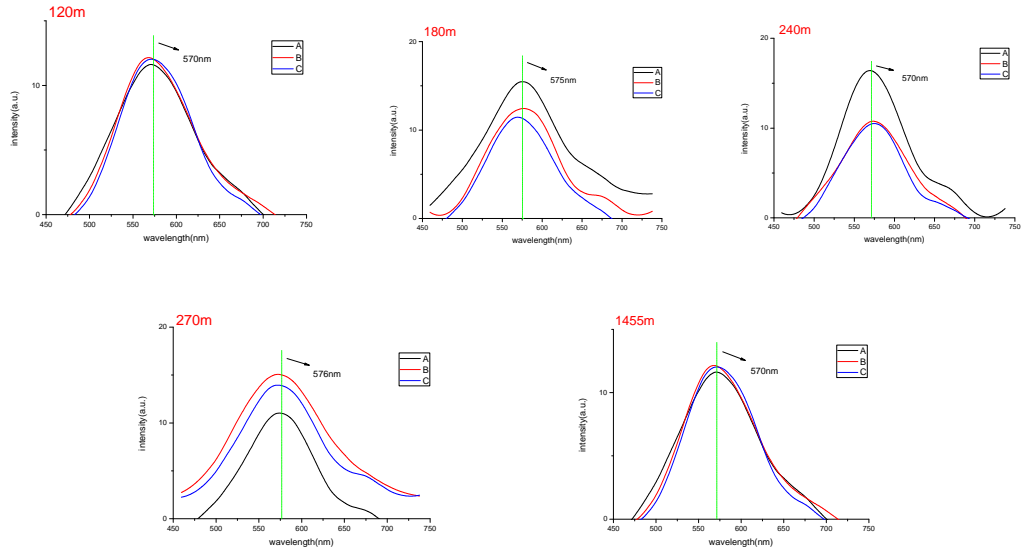
Figure 2. Surface topography of the dewetting films under the AFM.

The residual layer region and the droplets on the dewetted film were probed separately for the PL spectra as a function of time by using the confocal laser system (Figure 3).

a) Droplets



b) Residual thin film



c)

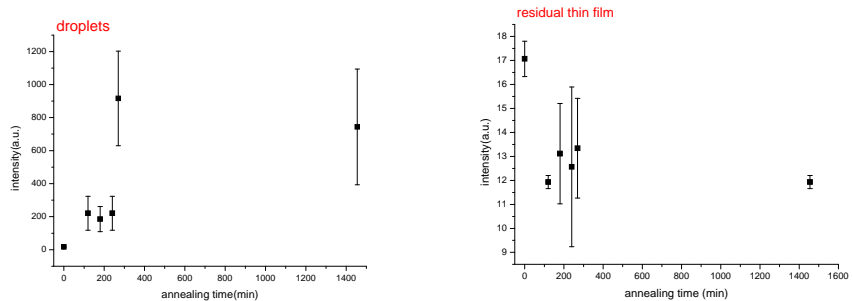


Figure 3. (a) The micro PL spectrum of the dewetting MEH-PPV/PS thin film (droplets), and A, B, C were the three different position.(b) the micro PL spectrum of the dewetting MEH-PPV/PS thin film

(residual thin film), and A, B, C were the three different position. (C) The average and error bar and the maximum intensity of the three different PL spectra

It was observed that the droplets emitted light robustly under the confocal system with a clear blue shift to 543 nm relative to the 550 nm intrachin emission of the initial films. The PL from the residual layer was also very high. The normalized PL intensity from the droplets to the droplet heights, however, was still remarkably smaller than that from the residual layer. Both, nevertheless, were considerably stronger than that from the initial film.

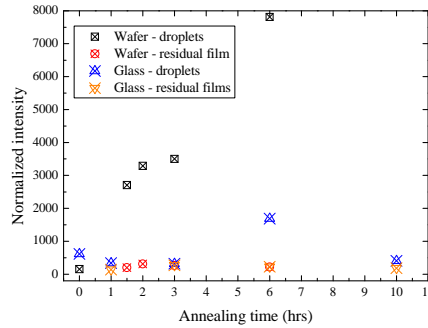


Figure 4. Fluorescent emissions from droplets and residual films in dewetting pattern

The large enhanced PL of the droplets was attributed to the surface layer that was under a strong tension with a dynamic equilibrium with the residual layer on the substrate (Figure 4). In the interior of the droplet, however, the polymer was not stretched such that the PL enhancement in the droplets was smaller than the residual layer. The blue shift of the droplet emissions was attributed to the molecular combing process that had occurred during the dewetting. It is interesting to note that in the polymer thin film system on silicon substrate, the emission peaks were identical at 543 nm for both the droplets and residual layer emissions (Figure 5). It indicates that the molecular separation in both the droplets and residual layer were comparable, suggesting a similar effect of molecular combing in both regions. However, for the polymer films on the glass slips, the residual layer emission was at 550 nm, red-shifted relative to the droplet emissions that were still at 543nm identical to those in the silicon substrate system. This seems to indicate that the initial film before dewetting on the glass slip had very different chain packing distribution particularly in the region next to the substrate. This indicates that dominate role of van der Waals interactions operative during the spin coating processes.

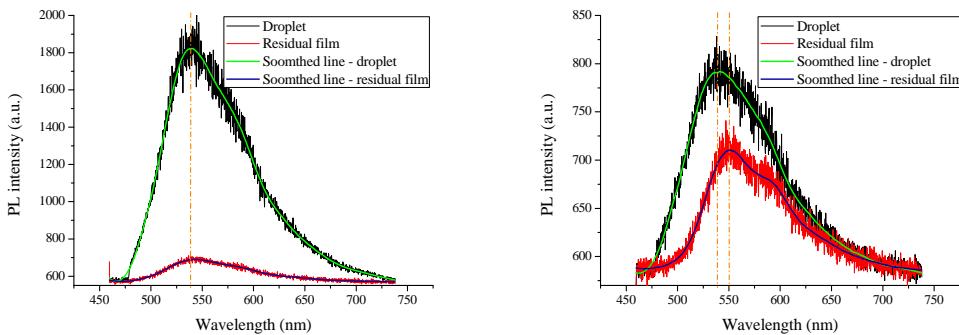


Figure 5. Confocal fluorescent spectra of droplets and residual films on silicon wafer (left) and glass slides (right).

Finally, it is very intriguing that the residual layer emission was essentially independent of the substrate. The bare silicon was known to have a strong quenching effect to the PL of conjugated macromolecules that resided in the as-spun films within 30 nm from the substrate. The quenching effect was arising from the charge injection of the separated excitons across the interface driven by the built in voltage between MEH-PPV and the silicon. This result strongly indicates that when the PL

was substantially enhanced by molecular constraints, the formation of excitons and thus the separation and the injection of the charges were subsequently suppressed. The competition between the time scales of the recombination and the separation of the freshly excited charges plays a deciding role for the ultimately optimized PV performance upon molecular constraints.

### **Conclusions:**

By using a confocal laser system integrated with an AFM, the micro PL behavior of conjugated polymer thin films during dewetting was explored and compared with the previous far-field PL results. The droplets emission was robust, attributing to the stretching of the surface layer on the droplets that was in dynamic mechanical equilibrium with the residual layer. The PL efficiencies of the droplets, however, were still lower than that of the residual layer, obviously due to the existence of the non-stretched volume in the droplet interior. Effects of molecular combing were noted in the droplets as well as the residual layer on bare silicon. The molecular separation in the residual layer on glass slip, however, was insignificant, obviously due to the tight packing of conjugated polymer chain segments near the substrate arising from spin coating. This illustrates the important role played by the van der Waals interactions during macromolecules condensation of the spin coating. Finally, it was observed that when the PL was significantly enhanced, the exciton formation as well as the charge separation and injection driven by the built-in voltage at the substrate surface were substantially suppressed. This has very important implications for the optoelectronic physics and the PV applications of the conjugated polymers.

### **References:**

- [1] G. Gustafsson, Y. Cao, G. M. Treacy, F. Klavetter, N. Colaneri, and A. J. Heeger, *Nature* **357**, 477(1992).
- [2] D. Braun, A. J. Heeger, *Appl. Phys. Lett.* **58**, 1982 (1991)
- [3] G. He, Y. Li, J. Liu, Y. Yang, *Appl. Phys. Lett.* **80**, 22 (2002).
- [4] P. F. Barbara, A. J. Gesquiere, S.-J. Park, Y. J. Lee; *Acc. Chem. Res.* **38**, 602 (2005).
- [5] J. Yu, R. Lammi, A. J. Gesquiere, P. F. Barbara; *J. Phys. Chem. B* **109**, 10025 (2005).
- [6] J. Yu, D. Hu, P. F. Barbara; *Science* **289**, 1327 (2000).
- [7] K. P. Tung, *Master Thesis*, 2008, Department of Materials Science and Engineering, National Tsing Hua University, Taiwan; K. P. Tung, B. J. Chen, C. H. Tsao, T. M. Hong, K. C. Hwang, A. C.-M. Yang, “Large Optoelectronic Enhancement Induced by Molecular Stretching in Conjugated Single Molecule Polymers”, in submission.

## SECTION 4

### Molecular Packing in Spin-Coated Thin Films of Conjugated Polymer and the effect on Photoluminescence

Peiwei Lee, Yi-Chien, Wei-Chen Li, Chih-Hong Chang, Arnold Chang-Mou Yang\*  
Department of Materials Science and Engineering, National Tsing Hua University, Hsinchu 300,  
Taiwan

#### Abstract

The Chain conformation of conjugated polymer MEH-PPV frozen in ultrathin films from spin coating was controlled and its effect on the photoluminescence (PL) was studied by preparing two sample series of varying thickness with either the rotation speed or polymer concentration in the solution changed. The experiment was conducted with substrate varied in order to explore the role of van der Waals interactions between surfaces on the molecular condensation process. First of all, the film thickness decreased exponentially with the spin rate but increased linearly with the polymer concentration, showing no dependence on the substrate for both the sample series. The PL efficiency was found to generally decrease with film thickness, implying that larger frozen molecular deformations, and hence greater residual stresses, gave rise to higher PL efficiencies. The films condensed on the thermodynamically stable surfaces (Hamaker constant:  $A_{eff} < 0$ ) demonstrated significantly lower PL efficiencies than those on the positive  $A_{eff}$  substrates, where the PL efficiencies may vary by a factor of 2 for films of identical thickness but on different substrates. This substrate effect, however, diminished when the film thickness became thicker than ~80 nm. Furthermore, films of same thicknesses but condensed under distinct conditions where the solvent evaporation rate were different, the molecular packing and the PL efficiencies varied significantly for films on unstable surfaces ( $A_{eff} > 0$ ), where the variations may go up to 4 times, but not on the stable surfaces ( $A_{eff} < 0$ ). Finally, substantial PL quenching was observed in the ultrathin films on bare silicon where a strong built-in voltage existed at the film-substrate interface. This quenching effect vanished as the film thickness increased to above ~60nm. Blends of MEH-PPV in polystyrene were also prepared for studying the additional chain conformation effect due to dilution.

#### Introduction

Conjugated polymers have attracted broad interests due to their application potentials in many areas, such as lighting, displays, and photovoltaic cells.[1~4] Recently, important discoveries have revealed the existence of strong effects of chain packing and conformation on the optoelectronic efficiencies of conjugated polymers [5~8]. The root of this effect, however, requires understanding of the molecular condensation processes during the spin coating of the solid films. Spin casting has been the most popular method for preparing thin solid films of polymers. Recently, the processes of spin coating was examined in terms of residual stress and chain conformation and it was concluded that solvent evaporation plays a dominant role in the molecular packing process during the condensation [9~10]. The formation of a skin layer on the film surface during the rapid evaporation of the solvent and the evolutions of chain inter-diffusion or single molecular contraction were proposed to illustrate the complicated chain packing and to explain the intriguing optoelectronic behavior. In this report conjugated polymers thin films were prepared in two independent series by varying either the rotation speed or solution concentration in an effort to reveal the molecular process during the spin casting. In these experiments, the PL behavior was used to monitor the variations of chain packing. It was found that at lower film thicknesses (< ~50 nm), chain conformation and packing varied significantly by spin coating parameters. In addition, the supporting substrate that brought in entirely different van der Waals interactions between interfaces also played a fundamental role for the packing of polymer chains during the fast molecular condensation.

#### Experimental Section

The polymer poly[2-methoxy-5-((2'-ethylhexyl)oxy)-1,4-phenylenevinylene], MEH-PPV, was purchased from Sigma-Aldrich Chemical Co., with a molecular weight  $M_w \sim 200,000$  g/mol and with poly-dispersity ( $M_w/M_n$ ) around 5. Polystyrene was bought from Pressure Chemical Co. with  $M_w =$

2,032 g/mol and molecular weight dispersity  $M_w/M_n \leq 1.06$ . Figure 1 showed the structures of both MEH-PPV and PS. Both of these polymers were dissolved in a blend of solvents comprising equal parts toluene (HPLC/SPECTRO), THF (anhydrous) purchased from TEDIA and cyclohexanone (GC grade) purchased from Sigma-Aldrich.

The solvent system of toluene/THF/cyclohexanone was used to dissolve the mixture of MEH-PPV and PS. Concentration of the solution the mixture of MEH-PPV and PS composed by 1 : 99, 25 : 75, 75 : 25 and 100 : 0 mass ratio was at 1, 3, 6, 9, 12, 15 and 20 mg/ml. In addition, solution was stirred slowly at 50°C between 12 and 15 hours except that 100% MEH-PPV was stirred for 48 hrs and filtered (0.45  $\mu$ m pore size) to remove impurities in solution.

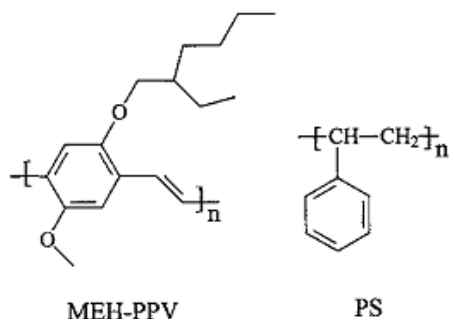


Figure 1 Structures of MEH-PPV and PS.

The polymer solution was then spin-casted on the substrates which were bare silicon wafers with a thin layer of native oxide, silicon wafer with 500 nm silicon oxide and glass cover slips. The film thicknesses, adjusted by changing the rotation speed from 1000 rpm to 7000 rpm or increasing solution concentration in spin coating process. After spin-casted, the films were stored in a box by foil wrapping to prevent light illumination and in vacuum atmosphere for 12 hours to evaporate the residual solvent in the spin-casting process.

After that he prepared films were used to measure the fluorescence by PL spectroscopy (Perkin Elmer) and scan the film morphology by atomic force microscopy (AFM).

## Results and Discussions

Thin films of pristine MEH-PPV were used by spin coating with the film thickness varied by either changing the rotation speed or solution concentration. It was found that the film thickness illustrated an negative exponential dependence on spin speed and a linearly dependence on the solution concentration. On the various substrates of bare silicon wafer, oxide wafer (500nm of SiO<sub>2</sub> on the Si wafer), and the specially treated hydrophobic glass slides, the film thickness demonstrate identical dependence on the spin speed and the polymer concentration, as shown in Figure 2. With the variation in film thickness, the molecular packing in the film changed and the PL spectra were obtained and studied.

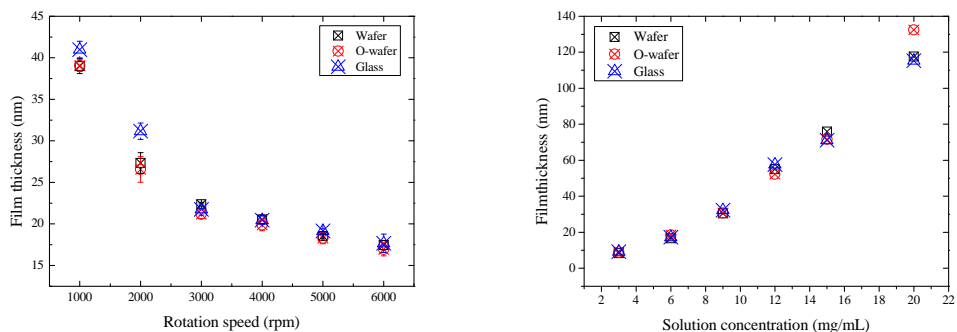


Figure 2. Thicknesses of the pristine MEH-PPV films controlled by varying either the rotation speed or polymer concentration of the solution.

Figure 3 and 4 showed PL emission spectra of 1%, 25%, 75% and 100% MEH-PPV blended thin films at different rotation speed. The PL spectra presented strong rotation rate dependence during spin casting. As can be seen, decreasing the rotation to 2000rpm displays a red shift due to aggregation between polymer chains. Particularly for 1% and 25% MEH-PPV blended films because of diluted effect [11] obviously made red shift by enhanced inter-chain interaction. The pure MEH-PPV thin film was characterized with two main peaks at 583 and 633 nm which were shown in Figure 3 and 4 it was well accepted that the emission peak at 583 nm origin from intra-chain excitons, while those peak or shoulders appearing at longer wavelength, such as 633 nm, are associated with inter-chain excitons. [12~14]

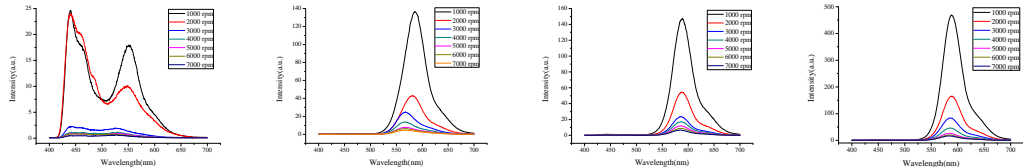


Figure 3. PL spectra of the films with the mass ratios of 1%, 25%, 75%, and 100% MEH-PPV in PS on silicon wafer.

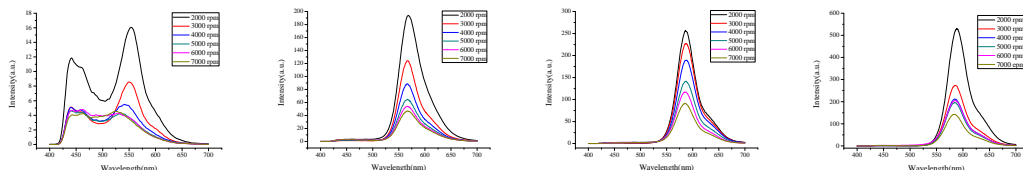


Figure 4. PL spectra of the films with the mass ratios of 1%, 25%, 75%, and 100% MEH-PPV in PS on glass slides.

A detailed fluorescent emission analysis by combining peak position and peak intensity of PL spectra revealed chain conformation affecting photoluminescence emission due to chain packing on different substrates as shown in Figure 5. Whether at lower or higher rotation speed, it showed that peak position will shift to longer wavelength due to lengthening conjugation length and aggregation as increasing the percentage of MEH-PPV in the thin films on silicon wafer and glass slides. In addition, PL intensity enhanced with increasing the percentage of MEH-PPV in the films.

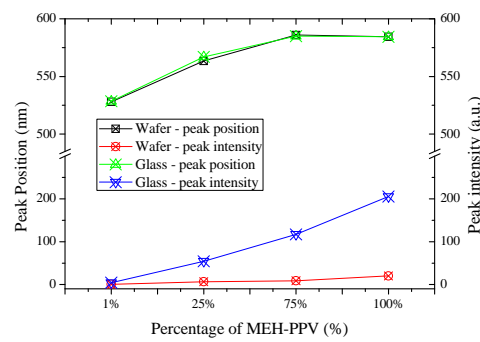


Figure 5 Comparison of percentage of MEH-PPV in the thin film on different substrates.

The photo-luminescence spectra of the neat MEH-PPV films on the various substrates are shown in Figure 6. Unlike the effect of rotation speed, increasing film thickness by raising concentration showed no red shift on wafer and glass except for oxide wafer. It meant that the molecular packing and chain conformation were varied by the changes in the rotation speed and polymer concentration.

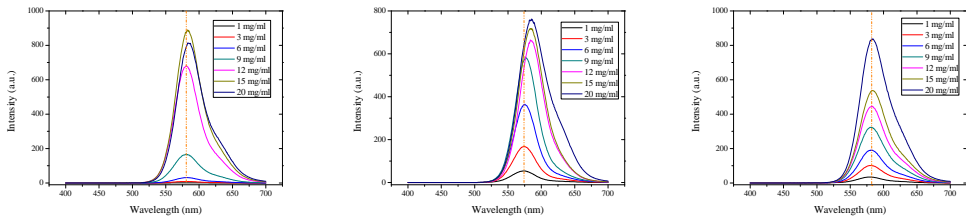


Figure 6. PL spectra from a range of MEH-PPV solution concentration on different substrates. The rotation speed and solution concentration were changed by rotation speed and solution concentration.

The van der Waals interactions between the molecules (solvent and polymer) with substrates played very an important role during the molecular condensation. Changing rotation speed produced change in solvent evaporation rate of the as-deposited liquid films. For higher spin speeds, more opened structures of MEH-PPV resulted that also demonstrated larger molecular strains and residual stresses. These films demonstrate greater PL efficiencies [15].

It was found that the surface energies of these substrates were quite dissimilar. The surface tensions of different substrates were obtained by measurements of the contact angle. The spreading of a film on a substrate could be described in terms of the effective Hamaker constant ( $A_{\text{eff}}$ ). [16]  $A_{\text{eff}} < 0$  corresponds to thermodynamic stability and perfect wetting, and  $A_{\text{eff}} > 0$  implies an attractive force leading to spinodal dewetting. Solvent in solution was uncomfortable on oxide wafer and glass slides that increasing evaporation during the spin coating processes. Solvent escaped from swollen coils, creating a concentration gradient and a skin layer at the top surface. As time gone on, the skin layer thickens, coils contract, and chain inter-diffusion gives rise to chain re-entanglement. When ultra thin films were deposited on oxide wafer and glass that formed a skin layer included constraint coils to enhance photoluminescence.

A hetero-junction was the interface that occurred between two layers or regions of dissimilar semiconductors. For type I, straddling gap, excitons dissociate at interface so that electrons and holes transport from higher energy band gap to lower band gap. Energy and gap of silicon wafer and MEH-PPV polymer are 1.12 eV and 2.34 eV respectively. However, MEH-PPV polymer on oxide wafer and glass slides were displayed reverse structure to MEH-PPV thin films on wafer as shown in Figure 7. Electrons dissociate at interface between film and silicon wafer would transfer to silicon substrate to reduce exciton recombination. Nevertheless, thin films on glass slides and oxide wafer electrons and holes couldn't cross the energy barrier to glass and oxide wafer even excitons would dissociate at interface. Energy transfer at the interface between MEH-PPV thin films and substrate contributes the photoluminescence enhancement due to numbers of exciton recombination.

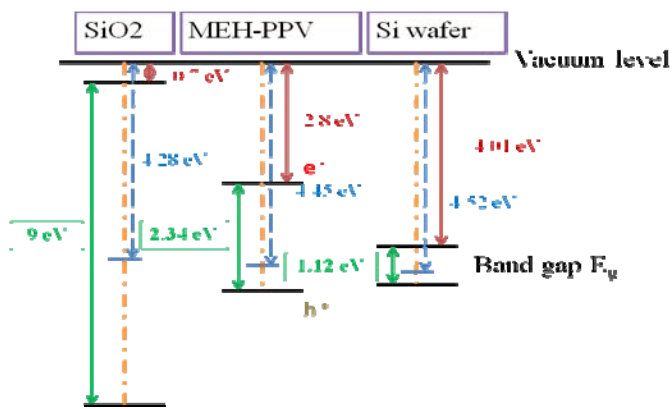


Figure 7 Energy diagram for MEH-PPV thin films on different substrates

The charge transport path and exciton diffusion length of MEH-PPV were 5 to 6 nm [17]. Charge injection at the interface between film and silicon wafer dominated around film thickness of 10 nm as shown in Figure 8. Films on glass and oxide wafer were linearly dependence with film thickness. In

the case of increasing solution concentration normalized PL intensity tended to a constant at higher thickness. For silicon oxide wafer and glass, solvent in liquid film evaporated faster than silicon wafer due to the effective Hamaker constant. Therefore, at lower film thickness there showed higher PL efficiency on silicon oxide wafer and glass resulting from constraint skin layers as overall films. However, effect of charge injection on silicon wafer excitons were transferred to substrates.

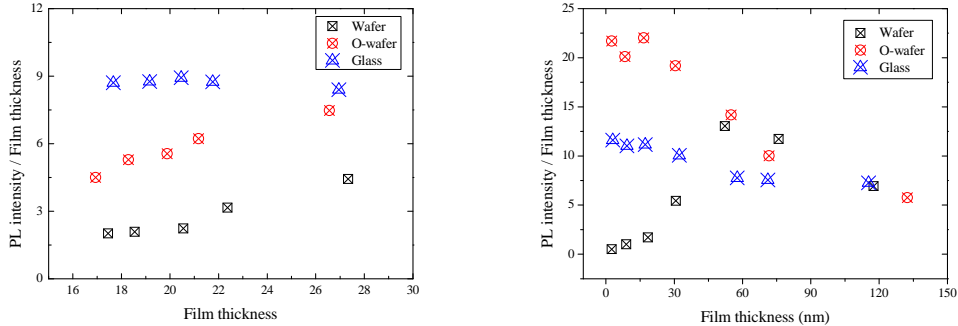


Figure 8 Normalized PL intensity changing by rotation speed (left) and solution concentration (right).

As clearly shown in Figure 8, the PL efficiency was found to decrease with film thickness, implying that larger residual stresses gave rise to higher PL efficiencies. Secondly, the films condensed on the negative  $A_{\text{eff}}$  surfaces demonstrated significantly lower PL efficiencies than those on the positive  $A_{\text{eff}}$  substrates. The PL efficiencies may vary by a factor of 2 for films of identical thickness but on different substrates. This substrate effect, however, diminished when the film thickness became thicker than  $\sim 80$  nm. Furthermore, films of same thicknesses but condensed under either varying concentration or spin speed where the solvent evaporation rate were very different, the molecular packing and the PL efficiencies varied significantly for films on unstable surfaces ( $A_{\text{eff}} > 0$ ), where the variations may go up to 4 times. This effect, however, was not observed in the films on the stable surfaces ( $A_{\text{eff}} < 0$ ). Finally, a large quenching effect on the PL was observed in the ultrathin films on the bare silicon where a strong built-in voltage existed at the film-substrate interface. This quenching effect decreased with film thickness and disappeared as the thickness increased to above  $\sim 60$  nm.

Finally, due to the formation of the skin layer generated during spin coating, it would prevent the residual solvent evaporated from the inner layer. For the thicker film, the more residual solvent would let the polymer chain in the film getting higher entropy, i.e. penetrate each other well. The ratio of PL intensity caused by intra-chain to inter-chain interaction should increase with increasing film thickness. The experiment is shown in figure 9. If we increase the blending ratio of MEH-PPV, then because penetrated conjugated polymer could not inhibit the e-h pair inter-chain interaction. The ratio of PL intensity caused by intra-chain to inter-chain interaction would be constant, as shown in Figure 9.

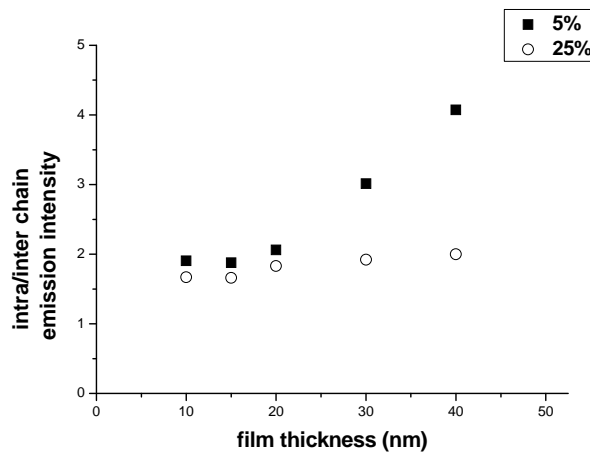


Figure 9: The ratio of PL intensity caused by intra-chain to inter-chain interaction versus film thickness, for low MEH-PPV concentration film, the ratio increase with film thickness; for higher MEH-PPV concentration film, the ratio maintain constant with increasing film thickness.

### Conclusions:

By changing the film thickness using the spin coating parameters of spin speed and solution concentration, the chain conformation of conjugated polymer MEH-PPV in ultrathin films was studied via the corresponding changes of the photoluminescence (PL). The important substrate effect due to van der Waals interactions was also unveiled. First of all, the PL efficiency was found to generally decrease with film thickness, indicating that larger frozen molecular deformations, and hence greater residual stresses, gave rise to higher PL efficiencies. The films condensed on the thermodynamically stable surfaces demonstrated significantly lower PL efficiencies than those on the positive  $A_{eff}$  substrates, indicating the possible influences from partial dewetting of the transient viscous films during the spin coating. The PL efficiencies may vary by a factor of 2 for films of identical thickness but on different substrates. This substrate effect diminished when the film thickness became thicker than ~80 nm. Moreover, films of same thicknesses but condensed under distinct conditions where the solvent evaporation conditions varied, the molecular packing and the PL efficiencies changed significantly (up to 4 times,) for films on unstable surfaces ( $A_{eff} > 0$ ), but not on the stable surfaces ( $A_{eff} < 0$ ). Finally, PL quenching was observed in the films on bare silicon where a strong built-in voltage due to the energy gap difference existed at the film-substrate interface. Blends of MEH-PPV in polystyrene were also prepared for studying the additional chain conformation effect due to dilution.

### References

- [1] G. Gustafsson, Y. Cao, G. M. Treacy, F. Klavetter, N. Colaneri, and A. J. Heeger, *Nature* **357**, 477(1992).
- [2] D. Braun, A. J. Heeger, *Appl. Phys. Lett.* **58**, 1982 (1991)
- [3] D. Braun, A. J. Heeger, *Appl. Phys. Lett.* **58**, 1982 (1991).
- [4] G. He, Y. Li, J. Liu, Y. Yang, *Appl. Phys. Lett.* **80**, 22 (2002).
- [5] G. He, Y. Li, J. Liu, Y. Yang, *Appl. Phys. Lett.* **80**, 4247 (2002).
- [6] P. F. Barbara, A. J. Gesquiere, S.-J. Park, Y. J. Lee; *Acc. Chem. Res.* **38**, 602 (2005).
- [7] J. Yu, R. Lammi, A. J. Gesquiere, P. F. Barbara; *J. Phys. Chem. B* **109**, 10025 (2005).
- [8] J. Yu, D. Hu, P. F. Barbara; *Science* **289**, 1327 (2000).
- [9] P.G. de Gennes, *Eur. Phys. J. E* **6**, 421(2001).
- [10] P.G. de Gennes, *Eur. Phys. J. E* **7**, 31 (2002).
- [11] Gufeng He, Yongfang Li, Jie Liu and Yang Yang, *J. Appl. Phys.*, **80**, 22 (2002)
- [12] M. Yan, L. J. Rotherberg, E. W. Kwock, and T. M. Miller, *Phys. Rev. Lett.*, **75**, 1992 (1995)
- [13] Cole Boulevard, Golden, *Nature Mater.*, **6**, 683-696 (2006)

- [14] Benjamin J. Schwartz, *Nature Mater.*, 7, 427-428 (2008)
- [15] Jean-Luc Brédas, Robert Silbey, *Science*, 323, 348-349 (2009)
- [16] Longjian Xue and Yanchun Han, *Langmuir*, 25, 5135-5140 (2009)
- [17] D. E. Markov, C. Tanase, P. W. M. Blom, and J. Wildeman, *Phys. Rev. B*, 72, 045217 (2005)

## SECTION 5

### The Synthesis and Optoelectronic Behaviour of Conjugated Polymer Poly(3-hexylthiophene) Grafted on the Surface of Multi-Walled Carbon Nanotubes

Anh Phuong Le, Tsai-Ming Huang, Po-Tsun Chen, Arnold Chang-Mou Yang\*

Department of Materials Science and Engineering, National Tsing Hua University, Hsinchu 300, Taiwan

#### Abstract

A nanocomposite of multi-walled carbon nanotubes (MWCNTs) and poly (3-hexylthiophene) (P3HT) was prepared by grafting P3HT uniformly on the surface of CNTs (P3HT/P3HT-g-CNT) via a “grafting from” method with the coating thicknesses controlled. It was found that as the coating thickness decreased, the crystallinity of the P3HT decreased, along with significant red-shifting of Raman that signified alterations of chain conformation. Furthermore, although the photoluminescence peak remained unchanged when grafted on CNTs, modifications of P3HT energy gap was observed, indicating variations of vibronic levels arising from the grafting. Moreover, broadening of the PL emission took place that suggested decreasing of lifetimes of the photo-generated species when grafted on CNTs. Bilayer photovoltaic devices with the [6,6]-phenyl C<sub>61</sub>-butyric acid methyl ester (PCBM) as the electron acceptor have shown that the nanocomposite P3HT/P3HT-g-CNT performed much more efficiently as the electron donor, in both photocurrent density and power conversion efficiency, compared to the neat P3HT.

**Keywords:** Poly(3-hexylthiophene), Multi-walled carbon nanotubes, photovoltaic behavior.

#### Introduction

During the past decade, carbon nanotubes (CNTs), including multiwalled carbon nanotubes (MWCNTs) and single-walled carbon nanotubes (SWCNTs), have been used in numerous applications of many different fields due to their unique physical and mechanical properties, exceptional electrical conductivity, thermal stability and ultrahigh dimensional aspect ratio [1-5]. CNTs are insoluble in most solvents and polymer matrices due to the strong Van der Waal attractive force between CNTs [6]. This complicates efforts to utilize their outstanding physical properties in nanocomposites. To improve the dispersion of CNTs in solvents and polymer matrices, two main methods are employed to be a physical method and a chemical modification/functionalization. For the chemical method, molecules are grafted on the surface of CNTs [7]. The dispersion of CNTs can be improved by the interaction force between molecules and solvent. Among more successful approaches for the dispersion, various polymers were applied to CNT for yielding CNT-polymer hybrid composites, which exhibit better dispersion in polymer matrix and solvents [8].

The discovery of conducting polymers during the 1970s resulted in intense research by the possible replacement of conventional inorganic or metallic components in a wide range of applications, such as sensors, energy storage, corrosion inhibitors, enzyme activity, electronic and optoelectronic devices [9-11]. Among the various conducting polymers, poly (3-hexylthiophene) P3HT have attracted considerable attention in recent years because of its solubility, high carrier mobility, ease of doping, good thermal and electrical stability [8-9,12-14]. Hybridization of polythiophene and functional nanomaterials usually enhances the combined attributes of each components, such as conducting properties, optical properties and donor-acceptor properties [14].

Conducting polymer/CNTs composites have attracted more attentions due to their promising applications in nanoscale photoactive materials. Both SWCNTs and MWCNTs have been found to enhance the conductivity of CNTs/polymer composites many times [15]. Lately, S. J. Henley et al. presented that MWCNTs improved the performance of organic solar cell (OSC) and

electroluminescent devices due to emission quenching by MWCNTs [16-17]. Moreover, B. Philip et al. [12] have demonstrated that grafting conducting polymer on CNTs produces a better performance than that of the composite made by simply blending. Recently, Dai et al. [18] also reported that the soluble P3HT-grafted carbon nanotubes via a “grafting to” method with the esterification reaction. The photovoltaic device based on P3HT-grafted carbon nanotubes showed a higher short-circuit current and open-circuit voltage than its counterparts based on pure P3HT or mixture of P3HT and MWCNTs [18].

Herein, P3HT grafted on the surface of MWCNTs (P3HT-g-CNT) were carried out via the surface “grafting from” method to investigate the effect of different coating thickness of polymer chains attached on CNTs to their optoelectronic properties. In this, we report the synthesis, the characterization and the optoelectronic behaviour of P3HT-g-CNT.

## Experimental Section

### *Polymer grafted on MWCNTs via a “grafting method”*

1 g purified sample of MWCNTs were refluxed in 20ml concentrated nitric acid HNO<sub>3</sub> (16M)/ 30 ml concentrated sulfuric acid H<sub>2</sub>SO<sub>4</sub> (98%) (v/v=3/2) at 150°C for 1.5 hours, resulting in attachment of carboxylic acid groups (—COOH) on the surface of MWCNTs. After acid treatment, the acid-treated MWCNTs (CNT-COOH) were added to a great deal of deionized water and then purified via vacuum-filtering through a 0.2 µm polytetrafluoroethylene (PTFE) membrane. The solid was washed with deionized water repeatedly until the pH of the filtrate reached 7. After this step, CNT-COOH was dried at 80 °C in the vacuum oven. To determine the total percentage of acidic sites in the MWCNTs, the acid-base titration method was used [19]. The density of surface acidic groups in the treated MWCNTs is about 3%.

To prepare for the anchoring reaction, the CNT-COOH was converted to acylchloride (CNT-COCl) in thionyl chloride (SOCl<sub>2</sub>) (3ml) at 70°C for 1 hour. After the reaction, the excess SOCl<sub>2</sub> was removed under vacuum. The residue was flushed with nitrogen. Then, CNT-COCl was added into the reactor with 0.1 ml pyridine and reacted with monomer 3TE (0.1ml) in 10ml chloroform (CHCl<sub>3</sub>) at 50°C for 24 hours to eliminate HCl. The resulting viscous solution was washed in CHCl<sub>3</sub> with sonication and then vacuum-filtered through a 0.2 µm PTFE membrane to yield MWCNTs functionalized with 3TE (3TE-g-CNT).

The synthesis of poly(3-hexylthiophene) grafted on MWCNTs (Step I) was carried out as following procedures: 7.5 ml of acetonitrile (CH<sub>3</sub>CN) containing 1 mg of 3TE-g-CNT was sonicated for 4 hours at the room temperature. Then adding 0.16 ml monomer 3-hexylthiophene (3HT) in a dispersion of 3T E-g-CNT in CH<sub>3</sub>CN and this mixture was sonicated for 30 minutes. This solution was added to a 100 ml, double-necked, round-bottom flask equipped with a magnetic stir bar. FeCl<sub>3</sub> (0.325 g) dissolved in 2.5 ml CH<sub>3</sub>CN was added gradually to the solution. 30ml CHCl<sub>3</sub> solvent was then added to the solution and stirred for 30 minutes at 2°C. The resultant mixture was precipitated in methanol. This was filtered off and washed with methanol to remove FeCl<sub>3</sub>. After that, using ammonia dedoping to remove C l<sup>-</sup> and ethylenediamine tetraacetic acid (EDTA) to remove Fe<sup>3+</sup>, as suggested by Anderson et al. [20], and then carefully using centrifuge to remove free polymer by washing in toluene repeatedly and dried to yield P3HT grafted on MWCNTs (P3HT-g-CNT).

The polymerization of Poly(3-hexylthiophene) from the product of step I (Step II) was done as following steps: The product of step I, P3HT-g-CNT, was collected and dispersed in CHCl<sub>3</sub> in an ultra-sonic bath. Monomer 3-hexylthiophene (3HT) was then added in a dispersion of P3HT-g-CNT in CHCl<sub>3</sub>. Table 1 shows the summary of reaction conditions to synthesize P3HT grafting on the surface of MWCNTs. For step II-A, 0.325 g of FeCl<sub>3</sub> in 0.4 ml CH<sub>3</sub>CN and 2.1 ml CHCl<sub>3</sub> was sonicated for 10 mins to dissolve FeCl<sub>3</sub> before added into a dispersion of P3HT-g-CNT/monomer in CHCl<sub>3</sub>. For

step II-B, 10ml of CHCl<sub>3</sub> containing 0.65 g of FeCl<sub>3</sub> was sonicated for 2 hours at room temperature to disperse FeCl<sub>3</sub>. Then, adding 1ml FeCl<sub>3</sub>/CHCl<sub>3</sub> every 5 minutes into a dispersion of P3HT-g-CNT in CHCl<sub>3</sub>. The resulting reaction mixture was poured into methanol, and a precipitate was formed. This was filtered off and washed with methanol, ammonia, EDTA to remove FeCl<sub>3</sub> as above.

For the preparation of P3HT, monomer 3HT (0.16 ml) was added to a suspension of anhydrous FeCl<sub>3</sub> (0.65 g) in 10 ml CHCl<sub>3</sub>, and then the mixture was stirred at 2°C. After 30 mins, the reaction mixture was poured into methanol and a precipitate formed. This was filtered off and washed with methanol many times. The resulting polymer was then completely dedoped by stirring the polymer in chloroform and concentrated ammonia as suggested by Anderson et al. [20]. The dried polymer was then used to measure the head-tail regioregularity by proton NMR spectroscopy by dissolving in CDCl<sub>3</sub>. The regioregularity was calculated from the <sup>1</sup>H NMR spectra by comparing the relative integrations of the signals at chemical shifts of ca. 2.80 [head-to-tail (H-T)] and 2.58 [head-to-head (H-H)] ppm as Han et al. reported [21].

For defunctionalization of P3HT-g-CNT, 5 mg sample of as-prepared P3HT-g-CNT was dissolved in 10 ml of THF in a 25 mL round flask fitted with a condenser. Then 2.5 ml of 1M KOH/ethanol solution was added to the flask. The content of the flask were boiled under reflux for 72 h, resulting in the defunctionalized MWCNTs and detached P3HT. The solution phase was filtered and evaporated to dryness. Polymer was dissolved in THF and then precipitated by adding acidified methanol and dried in a vacuum.

Polymer solar cells using ITO (Indium tin oxide) as an anode and LiF/Al as a cathode were prepared according to the following procedure: The ITO-coated glass substrate (~13 ohm/square) was cleaned with detergent (purchased from Merck Taiwan Ltd.), deionized water, acetone and isopropyl alcohol in ultrasonication for 10 minutes, respectively, and subsequently dried in a vacuum overnight. In order to hole transport and modification of ITO surface, poly(3,4-ethylenedioxythiophene):poly(styrenesulfonate) (PEDOT:PSS) was spin coated on the ITO substrate (3000 rpm) with a thickness of ~40 nm and dried in a vacuum oven to remove solvent. The active layer was then spin coated on top of the PEDOT layer. The thickness of the active layer was controlled about 130 nm. For the bilayer solar cells, the active layer of controlled device was spin-coated by 4% of P3HT from chlorobenzene (~110 nm) first and then coated by 5% of PCBM from dichloromethane (~110 nm). Finally, the layers of LiF (0.7 nm) and Al (150 nm) were deposited by thermal evaporation method. The effective area of the device was 0.25 cm<sup>2</sup>. The power conversion efficiency of the PV cells was calculated using the following equations

$$FF = \frac{V_m \times I_m}{V_{OC} \times I_{SC}} \quad (1)$$

$$\eta = \frac{P_{OUT}}{P_{IN}} = \frac{FF \times V_{OC} \times I_{SC}}{P_{IN}} = \frac{V_m \times I_m}{P_{IN}} \quad (2)$$

where  $V_{OC}$  and  $I_{SC}$  are the open circuit voltage and short circuit current, respectively.  $V_m$  and  $I_m$  are the voltage and current at the maximum output power point, respectively, and  $P_{IN}$  is the incident light power.

#### Instrumentation

The average molecular weights of the defunctionalized P3HT and neat P3HT were determined by using gel permeation chromatography (GPC) using a Waters binary HPLC pump and THF as a solvent. Polystyrene was used as a standard for molecular weight measurement. The FTIR spectra of the samples were performed from a KBr pellet of the samples in a Horiba FTIR instrument [FTIR-730 HORIBA]. Spectra over the range 4000-400 cm<sup>-1</sup> were recorded by the co-addition of 20 scans operated at a resolution of 4 cm<sup>-1</sup> and a scan speed 5.0 cm<sup>-1</sup>/s. The morphology of MWCNTs-g-P3HT was studied using a transmission electron microscope (TEM JEOL, 2010EX) operated at an accelerated voltage of 200 kV. Samples for TEM measurements were prepared by diluted solutions and drop casting on a carbon-coated copper grid.

The polymer content grafted on the surface of CNTs was measured by thermogravimetric analysis (TGA). TGA/Perkin-Elmer Thermal Analyst Pyris system equipped with a thermogravimetric analyzer was used and operated at a heating rate of  $10^0 \text{C} \cdot \text{min}^{-1}$  and an argon flow rate of  $100 \text{ ml} \cdot \text{min}^{-1}$ . The wide-angle X-ray scattering (WAXS) experiments were carried out by using a X-ray diffraction method (Rigaku D-max). The instrument was operated at a 30 kV voltage and a 20 mA current. Nickel-filtered copper  $\text{K}\alpha$  radiation ( $\lambda = 0.154 \text{ nm}$ ) was used. The samples were scanned from  $2\theta = 2^\circ$  to  $30^\circ$  at the step scan speed  $2^\circ/\text{min}$ , and the diffraction pattern was recorded using a scintillation counter detector. For Raman spectroscopy a small amount of sample was placed on a polished metal surface on the stage of Leica microscope. Raman spectra were excited at 630 nm of laser radiation. Spectra were typically taken from 1800 to  $1100 \text{ cm}^{-1}$ .

The photoluminescence and photoluminescence excitation experiments were performed on a Perkin-Elmer instrument (LS55 luminescence spectrometer). The excitation wavelength was used at 350 nm. The current-voltage (I-V) characteristics of the photovoltaic devices were examined with a computer-controlled Keithley 2400 source measurement system and a fiber optic illuminator (Fiber-lite Model 190) under an illumination ( $18 \text{ mW cm}^{-2}$ ).

## Results and Discussions

The P3HT grafted on carbon nanotubes became highly soluble in various good solvents for P3HT, including chloroform, toluene and 1,4-dichlorobenzene.

The polymer P3HT grafted from the surface of CNTs was proved by microscopic and spectroscopic measurements in this study.

FTIR spectra of CNT-COOH, CNT-COCl and 3TE-g-CNT are shown in Fig. 1. There are several peaks in the range of 2800-3000  $\text{cm}^{-1}$  which can be attributed to the C-H stretching vibrations [8]. The  $798 \text{ cm}^{-1}$  peak of CNT-g-COCl corresponds to the stretching frequency of C-Cl bond and the  $1450 \text{ cm}^{-1}$  peak of 3TE-g-CNT corresponds to the stretching vibration of thiophene ring [9]. The C-S bending mode was identified at approximately  $726 \text{ cm}^{-1}$ , which indicates the presence of a thiophene monomer [8]. From the Fig. 1, the OH stretching frequency at approximately  $3400 \text{ cm}^{-1}$  shows in CNT-COOH sample and disappears in CNT-COCl, 3TE-g-CNT are observed. It is clear that every -COOH group on MWCNTs grafted with monomer 3TE.

Fig. 2 shows the TEM micrographs of samples of step I (P3HT-g-CNT-2), step II-A (P3HT-g-CNT-4), and step II-B (P3HT-g-CNT-8) with the coating thickness about 2.1 nm, 3.6 nm and 8.3 nm, respectively. The error bar of every thickness was calculated by the average of 48 points taken from different pictures. The coating thicknesses of P3HT grafted on the surface of CNTs are well-controlled and obviously increases from 2.1 nm to around 8.3 nm. TEM micrographs reveal that MWCNTs are coated uniformly by P3HT via the “grafting from” method.

The TGA thermograms of P3HT and the P3HT-g-CNT with different coating thickness of P3HT are shown in Fig. 3. From TGA, it is observed that P3HT is decomposed from  $100^0\text{C}$  to  $250^0\text{C}$ . For P3HT-g-CNT with 3 kinds of coating thickness, there're also obvious weight changes in the same range. At  $250^0\text{C}$ , the weight losses of samples P3HT-g-CNT-2, P3HT-g-CNT-4 and P3HT-g-CNT-8 were calculated to be 23%, 27% and 50%, respectively. The coating thickness of P3HT was calculated based on the weight ratio between P3HT and CNTs. Table 1 showed the consistency of P3HT coating thicknesses calculated from TEM and TGA data.

Fig. 4 presents the X-ray diffraction patterns for P3HT with three kinds of molecular weight  $1.4 \times 10^4 \text{ g/mole}$ ,  $3.2 \times 10^4 \text{ g/mole}$  and  $6.5 \times 10^4 \text{ g/mole}$ , CNT-COOH, P3HT-g-CNT-2, P3HT-g-CNT-4 and P3HT-g-CNT-8. From the Fig. 4, it is clear that CNT-COOH has a diffraction peak at  $2\theta = 25.9^\circ$ , corresponding to the plane 002 reflection, which is developed from the graphite-like structure [22]. For neat P3HT with different kinds of molecular weight, they show an interchain lamella peak corresponding to d-spacing  $\sim 17 \text{ \AA}$  ( $2\theta = 4.8^\circ \sim 5.5^\circ$ ) [9,11]. Besides, in amorphous region at a wide angle, P3HT has a peak at  $2\theta \sim 23.5^\circ$  (d-spacing  $3.8 \text{\AA}$ ), which represents the stacking distance of the

thiophene rings. P3HT-g-CNT-2 has only 1 peak at wide angle, corresponding to an amorphous region and the interchain lamella peak isn't observed. On the other hand, it is shown that P3HT-g-CNT-4 and P3HT-g-CNT-8 have the weak interchain lamella peak at  $2\theta = 4.8^\circ \sim 5.0^\circ$ . When the thickness increases, the effect of CNTs decreases; therefore, the crystalline peak can be observed. Besides, with the presence of CNTs, the peaks of amorphous region of P3HT shift from  $23.5$  to  $25.9^\circ$ . Therefore, it can be claimed that there is a decrease in the crystallization of P3HT with the presence of CNTs, leading to a more disordered structure for P3HT chains grafted on the surface of CNTs. This is consistent with a decreased melting point which Dai et al. [18] reported to indicate that CNTs inhibited the crystallization of P3HT.

Raman spectroscopy is a powerful technique to probe the structure – property relationship in both carbon nanotubes and conjugated polymers [23]. In Fig. 5, the typical Raman spectra of acid-treated MWCNTs (MWCNTs-COOH), P3HT-g-CNT with different coating thickness of P3HT and neat P3HT are presented. The Raman spectrum of MWCNTs shows two distinct peaks at  $1327\text{ cm}^{-1}$  and  $1587\text{ cm}^{-1}$ . The  $1587\text{ cm}^{-1}$  peak is termed G band, which characterizes the Raman-allowed phonon mode ( $E_{2g}$ ) of the graphite ring ( $sp^2$  carbon); whereas the  $1327\text{ cm}^{-1}$  peak is termed D band, which characterizes the disorder-induced phonon mode due to infinite size of crystals and defects [23-24]. In general, Raman spectra of the polythiophene family show the main dominant peak which is around  $1500$  to  $1450\text{ cm}^{-1}$  ( $C=C$  stretching region), which are totally symmetric, in-phase vibrations of the thiophene rings that spread over the whole polymer chain [25-26]. Here, P3HT spectrum is characterized by 2 peaks: one peak at  $1377\text{ cm}^{-1}$  related to  $C - C$  stretching and  $C - H$  bending and the other peak at  $1445\text{ cm}^{-1}$  related to  $C = C$  stretching. For P3HT-g-CNT with different coating thickness, it is observed that there're 3 peaks which are from the P3HT and MWCNTs. There's a shift of neat P3HT peak at  $1445\text{ cm}^{-1}$  to the peak at  $1430\text{ cm}^{-1}$  of P3HT grafted on MWCNTs. This observations may be related to the polymer conformation which is modified by  $\pi-\pi$  interaction with CNTs.

P3HT has a photoluminescence property [9]. Fig. 6 presented the photoluminescence spectra of P3HT with 3 kinds of molecular weight  $1.4 \times 10^4$ ,  $3.2 \times 10^4$  and  $6.5 \times 10^4$ , P3HT-g-CNT with 3 kinds of polymer coating thickness in solution. For an excitation wavelength of  $350\text{ nm}$  the solutions showed an emission at about  $539$ ,  $563.5$  and  $569\text{ nm}$  for P3HT-g-CNT-2, P3HT-g-CNT-4 and P3HT-g-CNT-8, respectively. When the coating thickness was increased, PL and PLE spectra had red-shifts due to the increase of molecular weight of P3HT grafted on CNTs (Fig. 6d). There's no difference between the PL peaks' positions of P3HT grafted on CNTs and neat P3HT with the same molecular weight. It indicates that P3HT before and after grafted on MWCNTs had the same luminescent centers which were responsible for the PL emission. However, the energy gap of the P3HT changed when grafted on CNTs, indicating variations of the vibronic energy levels of the molecularly constrained P3HT. Moreover, with the presence of CNTs, P3HT-g-CNT showed a significant blue-shifted broadening of the PL peaks compared to neat P3HT with the same molecular weight. It indicated the decrease of the lifetimes of the P3HT photoexcited species on CNTs that in turn suggested the increase of quantum efficiencies of the PL processes.

We have fabricated photovoltaic cells based on single layer pure P3HT or P3HT-g-CNT blended with P3HT (P3HT-g-CNT/P3HT), and bilayer photovoltaic cells consisting P3HT or P3HT-g-CNT/P3HT a nd PCBM as Fig. 7a. Any concentration of P3HT-g-CNT higher than 10% gave non-functional solar c ell due to the short circuit caused by MWCNTs. Fig. 7b describes the band gap diagram of the bilayer device. Fig. 7c and d shows the current-voltage ( $I-V$ ) curves for photovoltaic cells (PVs). The photovoltaic characteristics are listed in Table 2. The grafting P3HT on the surface of MWCNTs can be easily dispersed in the P3HT polymer matrix. Therefore, it can give the better performance for devices. Compared to PVs based on the pure P3HT, the P3HT/P3HT-g-CNT photovoltaic devices show an increased short circuit current ( $I_{SC}$ ) and open circuit voltage ( $V_{OC}$ ). However, the very small photocurrent is observed for the devices based on P3HT/P3HT-g-CNT. Once excitons in the P3HT phase diffuse and are dissociated at interfaces with the metallic tubes, they maybe undergo enhanced recombination within the tube due to the lack of an electronic band gap of MWCNTs.

To get a high efficiency, electron-hole dissociation plays an important role. From the charge separation's point of view, the bilayer structure device consisting of a p-type polymer P3HT or P3HT

blended with P3HT-g-CNT and an n-type ([6,6]-phenyl C61-butyric acid methyl ester) (PCBM) was fabricated. Figure 7d shows the *I-V* curves of devices with the bilayer film. The controlled bilayer cells fabricated here present higher performance. Compared to the device based on the pure P3HT, the devices based on P3HT/P3HT-g-CNT show an increased  $I_{SC}$  and  $V_{OC}$ . It was reported that MWCNTs can help the hole transport and may reduce the possibility for electron-hole recombination [15], so  $V_{OC}$  is increased from 0.3 to 0.35 V. As a result of increased  $I_{SC}$  and  $V_{OC}$ , the cell efficiency is enhanced. From 1% to 10% P3HT-g-CNT-2, the short circuit current is increased with the more content of CNTs, so the efficiency is also improved. The device based on 10% P3HT-g-CNT-2 shows an increase of 6 times power conversion efficiency compared to the device based on pure P3HT. The critical factors that affect the increase of efficiency of the devices in this report are the effective area of devices [27], the light source [27], the regioregularity of P3HT [22]. Structural regioregularity plays an important role in enhancing PV performance because the regioregularity of the polymer structure determines the photon absorption, exciton separation and carrier transportation in the active layer [22]. The regioregularity of P3HT which is synthesized here is 80% (Fig. S2). The relatively low fill factor and efficiency for these devices indicate that it's important to improve the device performance.

## Conclusions

Poly (3-hexylthiophene) (P3HT) grafted on the surface of multiwalled carbon nanotubes (MWCNTs) via the surface “grafting from” method is successful. Different coating thickness of P3HT grafted on MWCNTs is obtained by using the chemical oxidative polymerization with controlling different reaction condition. The P3HT grafted on MWCNTs can be well dispersed in common organic solvents and the P3HT polymer matrix. Raman spectra present that maybe the polymer conformation is modified by  $\pi$ - $\pi$  interaction with carbon nanotubes which causes a shift of P3HT peak from  $1445\text{ cm}^{-1}$  to  $1430\text{ cm}^{-1}$ . It has been demonstrated that the P3HT/P3HT-g-CNT/PCBM bilayer structure solar cells has shown an increase of 6 times power conversion efficiency. Therefore, conjugated polymer grafted on CNTs could be a very useful material for further optoelectronic applications.

## Acknowledgments

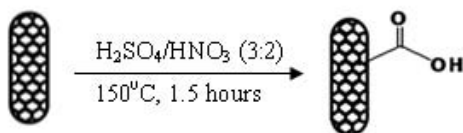
This work is supported by National Science Council, Taiwan and the US Air Force Office of Science and Research (AFOSR-AOARD).

## References

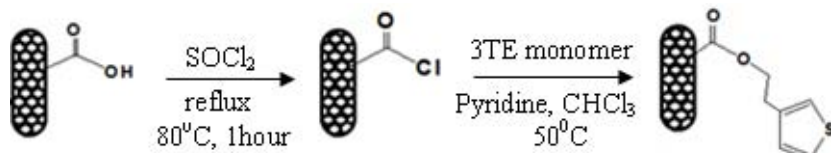
- [1] Jiang XW, Bin YZ, Matsuo M. Polymer 2005;46:7418-24.
- [2] Ounaies Z, Park C, Wise KE, Siochi EJ, Harrison JS. Composites Science and Technology 2003;63:1637-46.
- [3] Reich S, Thomsen C, Robertson J. Physical Review Letters. 2005;308:838.
- [4] Baibarac M, Romero PG. Journal of Nanoscience and Nanotechnology 2006;6:1-14.
- [5] Lin CW, Huang LC, Yang A CM. Macromolecules 2008;41:4978-88.
- [6] Lin Y, Zhou B, Fernando KAS, Liu P, Allard LF, Sun YP. Macromolecules 2003;36:7199-204.
- [7] Hirsch A, Angewandte Chemie International Edition 2002;41:1853-59.
- [8] Karim MR, Yeum JH, Lee MS, Lim KT. Materials Chemistry and Physics 2008;112:779-82.
- [9] Kuila BK, Malik S, Batabyal SK, Nandi AK. Macromolecules 2007;40:278-87.
- [10] Manceau M, Rivaton A, Gardette JL, Guillerez S, Lemaitre N. Polymer Degradation and Stability 2009;94:898-907.
- [11] Musumeci AW, Silva GG, Liu JW, Martens WN, Waclawik ER. Polymer 2007;48:1667-78.
- [12] Philip B, Xie J, Chandrasekhar A, Abraham J, Varadan VK. Smart Materials and Structures 2004;13: 295-8.

- [13] Karim MR, Lee CJ, Lee MS. *Journal of Polymer Science, Part A: Polymer Chemistry* 2006;44:5283-90.
- [14] Geng J, Kong BS, Yang SB, Youn SC, Park S, Joo T, Jung HT. *Advanced Functional Materials* 2008;18:2659-65.
- [15] Wu MC, Lin YY, Chen S, Liao HC, Wu YJ, Chen CW, Chen YF, Su WF. *Chemical Physics Letters* 2009;468:64-8.
- [16] Curran SA, Ajayan PM, Blau WJ, Carroll DL, Coleman JN, Dalton AB, Davey AP, Drury A, McCarthy B, Maier S, Strevens A. *Advanced Materials* 1998;10:1091-3.
- [17] Ago H, Shaffer MSP, Ginger DS, Windle AH, Friend RH. *Physical Review B* 2000;61:2286-90.
- [18] Kuila BK, Park K, Dai LM. *Macromolecules* 2010;43:6699-705.
- [19] Hu H, Bhowmik P, Zhao B, Hamon MA, Itkis ME, Haddon RC. *Chemical Physics Letters* 2001;345:25-8.
- [20] Andersson MR, Selse D, Berggren M, Jarvinen H, Hjertberg T, Inganas O, Wennerstrom O, Osterholm J.E. *Macromolecules* 1994;27:6503-6.
- [21] Han YK, Lee YJ, Huang PC. *Journal of the Electrochemical Society* 2009;156:37-43.
- [22] Liu SL, Yue J, Wehmschulte R. *Journal of Nano Letters* 2002;2:1439-41.
- [23] McCarthy B, Coleman JN, Czerw R, Dalton AB, Panhuis M, Maiti A, Drury A, Bernier P, Nagy JB, Lahr B, Byrne HJ, Carroll DL, Blau WJ. *Journal of Physical Chemistry B* 2002;106:2210-16.
- [24] Costa S, Palen EB, Kruszynska M, Bachmatiuk A, Kalenczuk RJ. *Materials Science-Poland* 2008;26:433-41.
- [25] Pron A, Louran G, Lapkowsky M, Zagorska M, Glowczyk-Zubek J, Lefrant S. *Macromolecules* 1995;28:4644-9.
- [26] Louran G, Trznadel M, Buisson JP, Laska J, Pron A, Lapkowsky M, Lefrant S. *Journal of Physical Chemistry* 1996;100:1232.
- [27] Law M, Greene LE, Johnson JC, Saykally R, Yang P. *Nature materials* 2005;4:455-9.

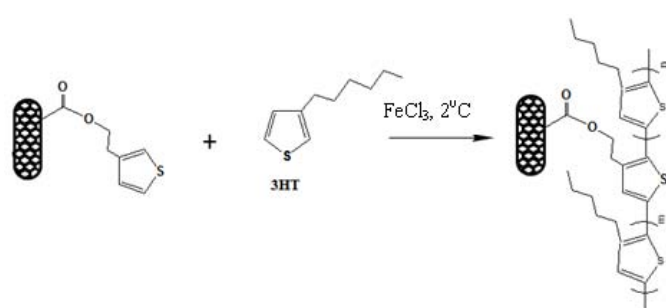
**Scheme 1. Acid treatment of MWCNTs**



**Scheme 2. Reaction scheme for Functionalization of CNTs with 3TE**



**Scheme 3. Reaction scheme for the polymerization of P3HT on the surface of CNTs**



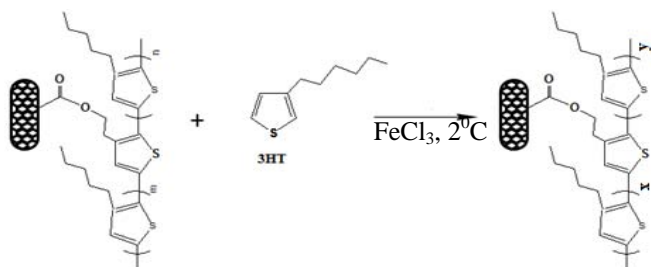


**Table 1**

Summary of conditions  
to synthesize P3HT grafted from CNTs to obtain different coating thickness and the band gap of

| Sample                    | Monomer volume (ml) | The amount of FeCl <sub>3</sub> (g) | Volume of CH <sub>3</sub> CN (ml) | Volume of CHCl <sub>3</sub> (ml) | Mol wt (Mw) × 10 <sup>-4</sup> | The coating thickness (nm) |                     | Bandgap (eV) |
|---------------------------|---------------------|-------------------------------------|-----------------------------------|----------------------------------|--------------------------------|----------------------------|---------------------|--------------|
|                           |                     |                                     |                                   |                                  |                                | Calculated from TEM        | Calculated from TGA |              |
| P3HT-g-CN T-2 (Step I)    | 0.16                | 0.325                               | 10                                | 30                               | 1.3                            | 2.1                        | 2.7                 | 2.58         |
| P3HT-g-CN T-4 (Step II-A) | 0.16                | 0.325                               | 0.4                               | 39.6                             | 3.0                            | 3.6                        | 3.5                 | 2.48         |
| P3HT-g-CN T-8 (Step II-B) | 0.16                | 0.65                                | 0                                 | 40                               | 6.6                            | 8.3                        | 7.9                 | 2.43         |

**Table 2**

The performance of photovoltaic cells based on P3HT, P3HT/P3HT-g-CNT and bilayers of P3HT/P3HT-g-CNT and PCBM.

| Samples                    | V <sub>OC</sub> (V) | J <sub>SC</sub> (mA/cm <sup>2</sup> ) | FF   | PCE (η) (%)           |
|----------------------------|---------------------|---------------------------------------|------|-----------------------|
| P3HT                       | 0.55                | 4.6*10 <sup>-4</sup>                  | 0.20 | 2.81*10 <sup>-4</sup> |
| P3HT/1% P3HT-g-CNT-2       | 0.66                | 8.4*10 <sup>-4</sup>                  | 0.23 | 7.08*10 <sup>-4</sup> |
| P3HT/5% P3HT-g-CNT-2       | 0.34                | 1.1*10 <sup>-3</sup>                  | 0.26 | 5.4*10 <sup>-4</sup>  |
| P3HT/10% P3HT-g-CNT-2      | 0.58                | 2.36*10 <sup>-3</sup>                 | 0.23 | 1.73*10 <sup>-3</sup> |
| P3HT/1% P3HT-g-CNT-4       | 0.39                | 1.04*10 <sup>-3</sup>                 | 0.22 | 4.96*10 <sup>-4</sup> |
| P3HT/5% P3HT-g-CNT-4       | 0.24                | 1.48*10 <sup>-3</sup>                 | 0.26 | 5.13*10 <sup>-4</sup> |
| P3HT/10% P3HT-g-CNT-4      | 0.3                 | 1.32*10 <sup>-3</sup>                 | 0.25 | 5.5*10 <sup>-4</sup>  |
| P3HT/1% P3HT-g-CNT-8       | 1                   | 1.48*10 <sup>-3</sup>                 | 0.18 | 1.48*10 <sup>-3</sup> |
| P3HT/5% P3HT-g-CNT-8       | 1                   | 1.32*10 <sup>-3</sup>                 | 0.16 | 1.17*10 <sup>-3</sup> |
| P3HT/10% P3HT-g-CNT-8      | 1.02                | 1.28*10 <sup>-3</sup>                 | 0.16 | 1.16*10 <sup>-3</sup> |
| P3HT/PCBM                  | 0.3                 | 0.0052                                | 0.18 | 0.0016                |
| P3HT/1% P3HT-g-CNT-2/PCBM  | 0.35                | 0.022                                 | 0.19 | 0.008                 |
| P3HT/10% P3HT-g-CNT-2/PCBM | 0.35                | 0.03                                  | 0.21 | 0.012                 |

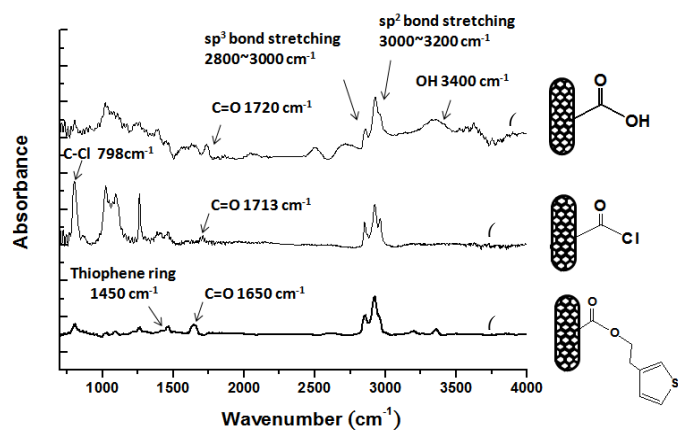


Fig. 1. FT-IR spectra of (a) CNT-COOH, (b) CNT-COCl, (c) 3TE-g-CNT.

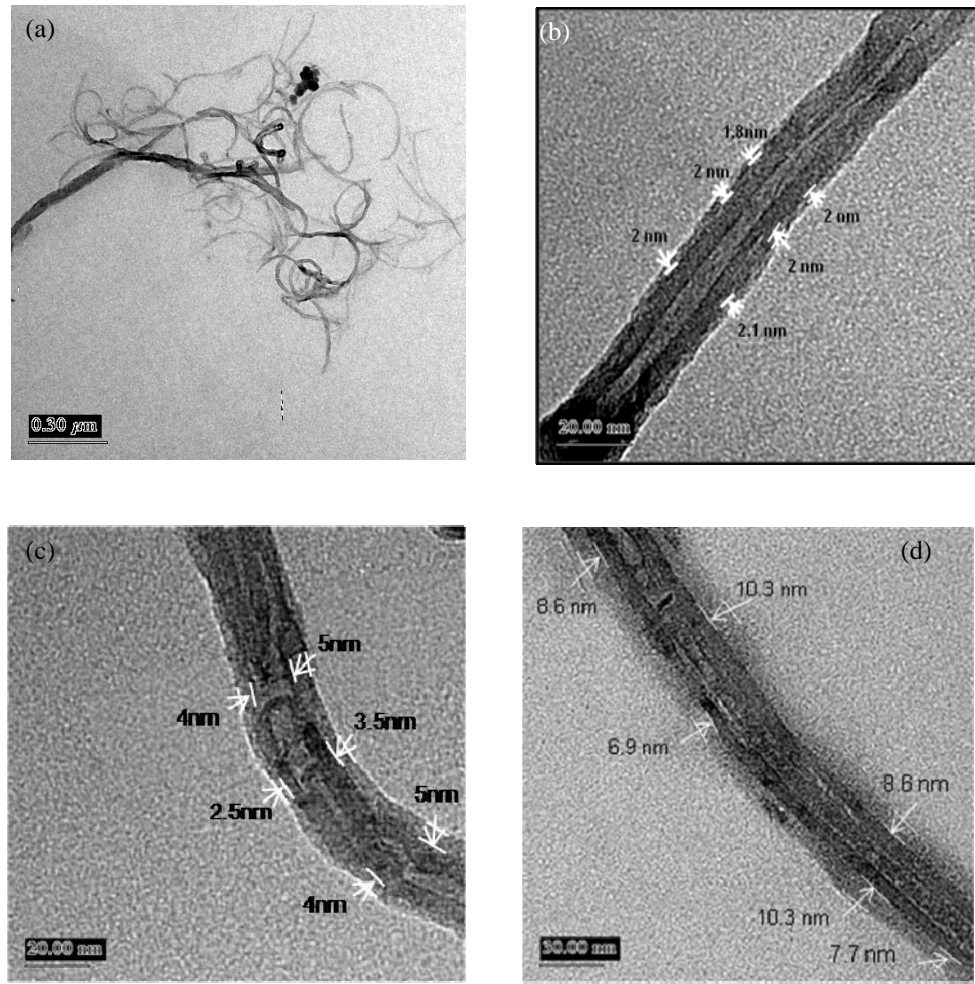


Fig. 2. TEM micrographs of P3HT-g-CNT (a) P3HT-g-CNT-2 (b) as for (a) but under a higher

magnification (c) P3HT-g-CNT-4 (d) P3HT-g-CNT-8 (the arrows point to the P3HT coating along the nanotube length).

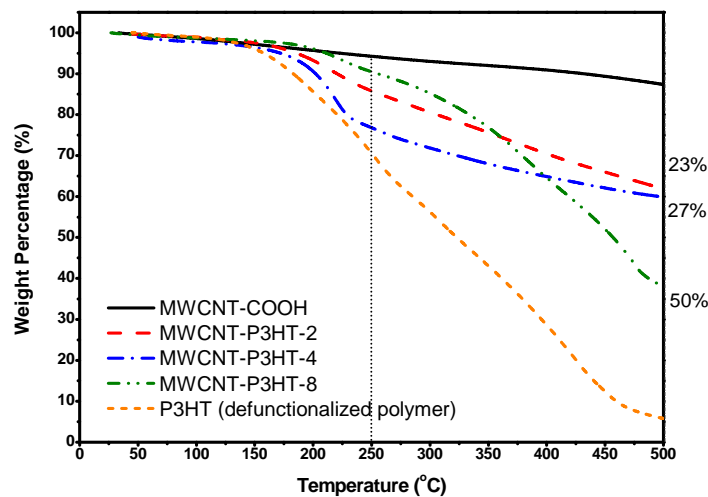


Fig. 3. TGA thermogram of acid treated CNTs, defunctionalized P3HT, P3HT-g-CNT-2, P3HT-g-CNT-4 and P3HT-g-CNT-8.

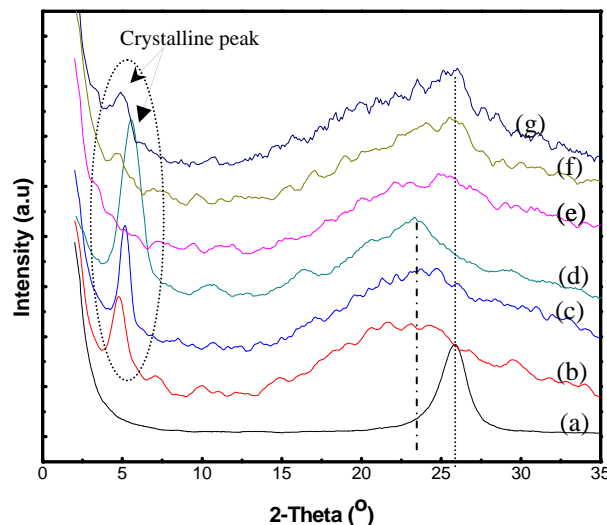


Fig. 4. WAXS patterns of (a) CNT-COOH, (b) P3HT (Mw:  $1.4 \times 10^4$ ), (c) P3HT (Mw:  $3.2 \times 10^4$ ), (d) P3HT (Mw:  $6.5 \times 10^4$ ), (e) P3HT-g-CNT-2, (f) P3HT-g-CNT-4, (g) P3HT-g-CNT-8.

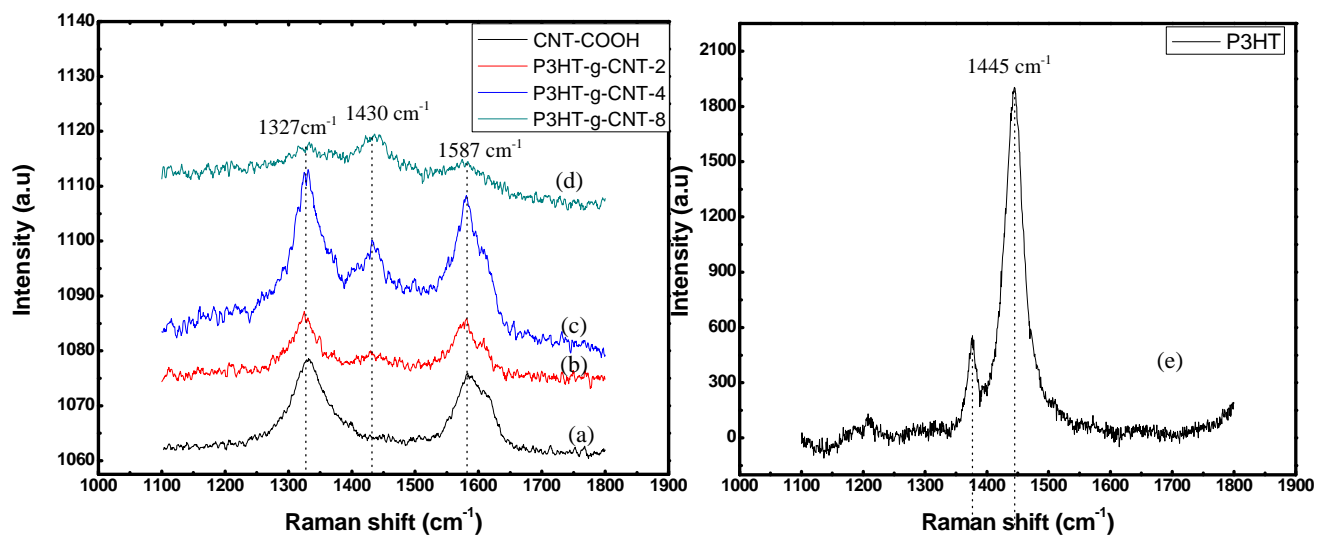


Fig. 5. Raman spectra of (a) acid treated CNTs, (b) P3HT-g-CNT-2, (c) P3HT-g-CNT-4, (d) P3HT-g-CNT-8 and (e) P3HT

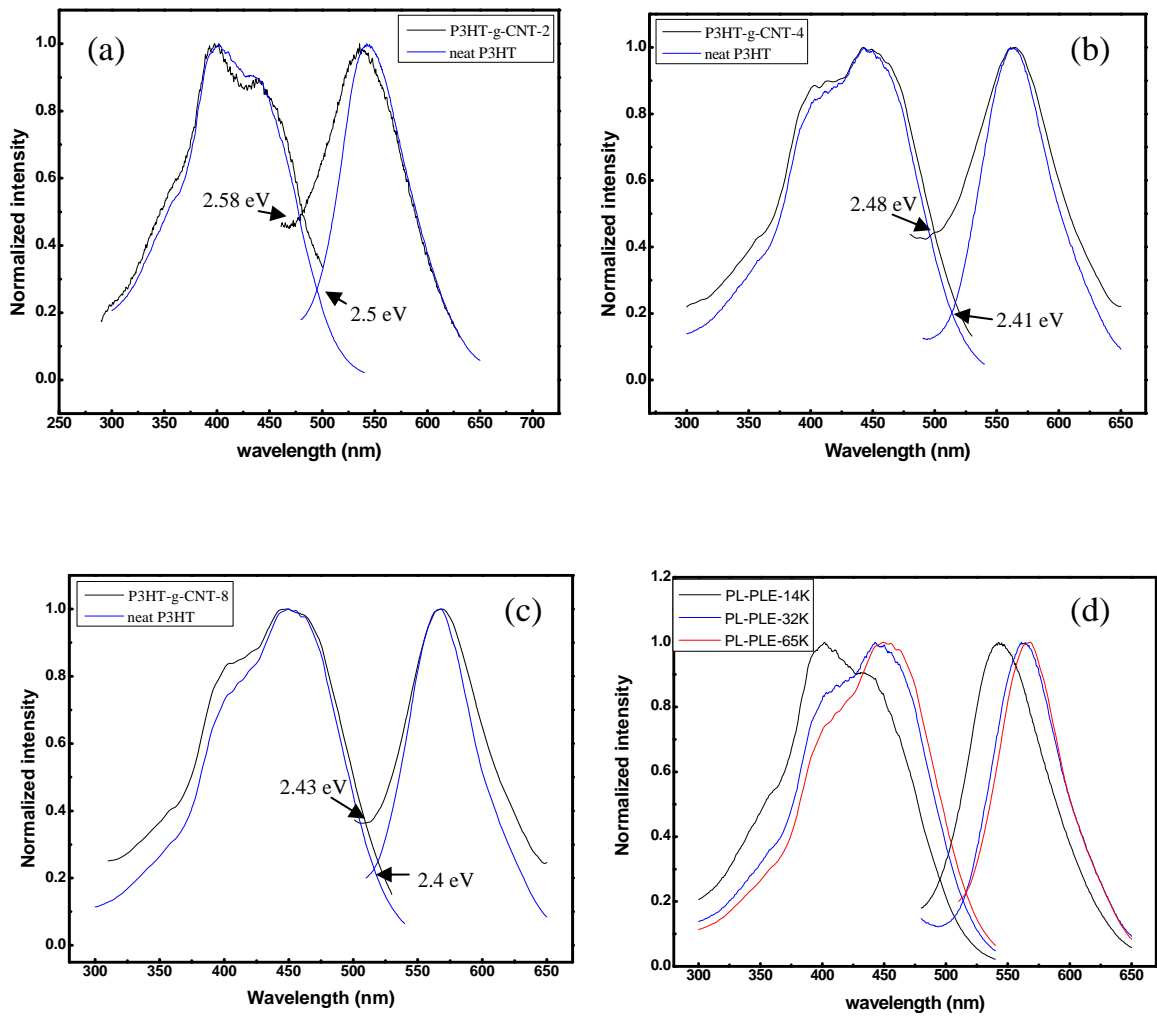


Fig. 6. Photoluminescence spectra and photoluminescence excitation spectra of (a) P3HT (Mw:  $1.4 \times 10^4$ ) and P3HT-g-CNT-2, (b) P3HT (Mw:  $3.2 \times 10^4$ ) and P3HT-g-CNT-4, (c) P3HT (Mw:  $6.5 \times 10^4$ ) and P3HT-g-CNT-8 in toluene solution at  $25^\circ\text{C}$ , (d) P3HT with Mw:  $1.4 \times 10^4$ ,  $3.2 \times 10^4$  and  $6.5 \times 10^4$ .

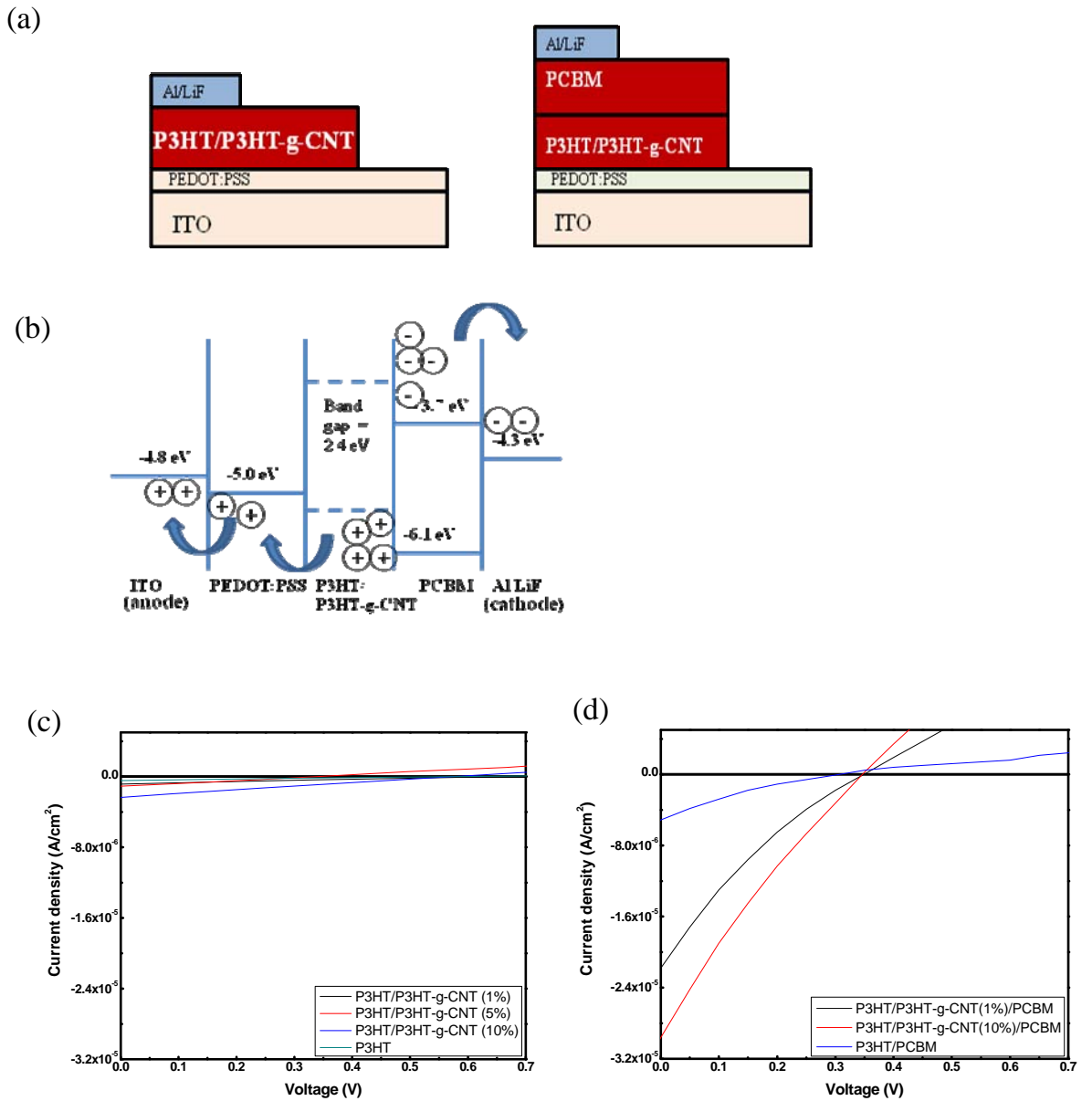


Fig. 7. (a) Schematic diagram of the proposed device structure (b) Band gap diagram of the bilayer device. (c)  $I$ - $V$  characteristics for solar cells based on P3HT and P3HT/P3HT-g-CNT-2 (1%, 5% and 10%), (d)  $I$ - $V$  characteristics for bilayer solar cells based on P3HT/PCBM and P3HT/P3HT-g-CNT-2 (1% and 10%)/PCBM.

## Supporting information

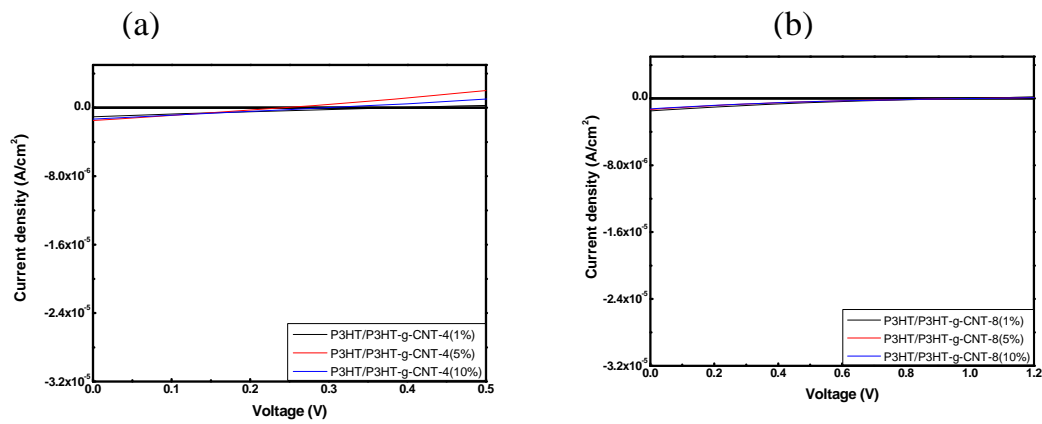


Fig. S1. (a)  $I$ - $V$  characteristics for solar cells based on P3HT/P3HT-g-CNT-4 (1%, 5% and 10%), (b)  $I$ - $V$  characteristics for solar cells based on P3HT/P3HT-g-CNT-8 (1%, 5% and 10%).

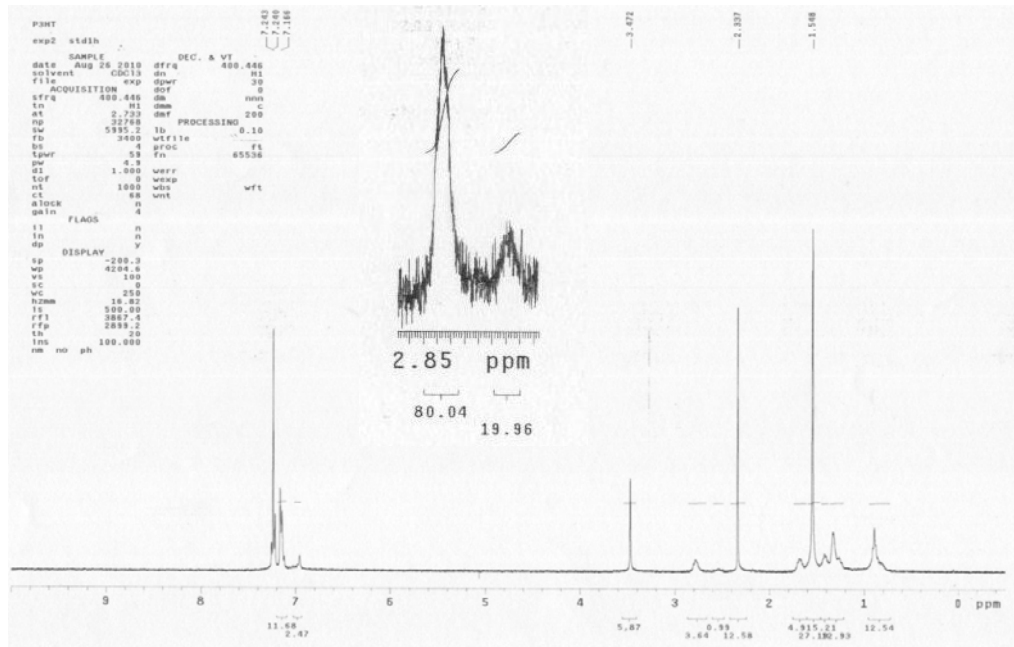


Fig. S2.  $^1\text{H}$  NMR spectra of P3HT

## SECTION 6

### Electric Conductivity of Polymeric Nanolayers Grafted on Multi-walled Carbon Nanotubes in Nanocomposites

Tsai-Ming Huang, Chih-Wei Lin, Yen-Hui Liu, Le Anh Phuong, Arnold C.-M. Yang\*  
Department of Material and Engineering, National Tsing Hua University, Hsinchu, Taiwan

#### Abstract

The conductive property of poly(3-hexylthiophene) (P3HT) grafted on multi-walled carbon nanotube (MWCNT) was studied in the research. The MWCNTs coated with different thickness P3HT nanolayers were blended with polystyrene (PS) to measure the resistivity of the P3HT-grafted MWCNT/PS composites. Owing to the orientation of P3HT-grafted MWCNTs, the resistivity and percolation threshold of the P3HT-grafted MWCNT/PS composites in vertical direction were much higher than them in horizontal direction. The resistivity of the grafted P3HT nanolayers was approximated by Boltzmann distribution and the resistivity of composites in the vertical and horizontal direction. Due to that the electron hopping mechanism dominated the conductive behavior of nano-thin films, the resistivity of grafted P3HT nanolayers exponentially decreased with reducing coating thickness and was lower than the resistivity of P3HT bulk, which consisted with the spin-coated P3HT thin films (5~100 nm). By studying the resistivity of P3HT nanolayers coated on MWCNTs, a method for measuring the conductivity of nano-thin films was provided and the possible dominating mechanism for the conductive behavior of nano-thin films was also figured out.

#### Introduction

Due to their high aspect ratio, nano-size, high flexibility, high mechanical strength, high electrical and thermal conductivity, carbon nanotubes (CNTs) are often used to make CNT/polymer composites to improve the physical properties of polymeric devices, such as transparent conductive films<sup>1</sup>, flexible solar cells<sup>2</sup> and flexible light-emitting diodes (LEDs)<sup>3</sup>. However, the strong van der Waal attractive force between CNTs makes CNTs aggregate and hard to disperse in polymer matrix. Therefore, the effect of the additional CNTs will be limited. To solve this problem, the surface of CNTs<sup>4</sup> are modified with molecules. By the interaction between the solvent and the molecules on CNT, the CNTs can be dispersed well in the CNT/polymer nanocomposites.

In the CNT/polymer composites, CNTs will form the percolation networks if the amount of the CNTs is higher than percolation threshold. These percolation networks provide express accesses for electrons to transport. Therefore, the resistivity of CNT/polymer composites is determined by the resistance of these CNT networks. The resistance of the CNT networks consists of two sources: (1) the intrinsic resistance of CNTs ( $R_{\text{CNT}}$ ) and (2) the contact resistance from the electrons migrating between two contacted CNTs ( $R_c$ )<sup>5</sup>. Comparing with  $R_{\text{CNT}}$ ,  $R_c$  is much larger than  $R_{\text{CNT}}$ <sup>6</sup>. Thus, the resistivity of CNT/polymer composites is mainly dominated by the contact resistance,  $R_c$ . The surface of the modified CNTs is covered with the molecules, however, which strongly affect the migration of the electrons between two contacted CNTs and  $R_c$  will increase. These coating molecules consume excess energy when the electrons transport in CNT/polymer composites and reduce the energy conversion efficiency of CNT/polymer devices such as solar cells and LEDs. Consequently, the electrical property of the coated molecules is an important issue to study.

Many mechanisms have been discussed for the conductive properties of nano-thin films. Electron tunneling effect was the mechanism often used to interpret the high conduction phenomenon in ultra-thin films of 1~3 nm<sup>6-8</sup>. However, the additional current was also found in the thin films of 70~400 nm, which was reported by T. Liang and Y. Makita<sup>9</sup>. They claimed that the additional current was coming from the leakage current effect, which was dominated by Schottky emission and Poole-Frenkel emission. Both of electron tunneling and the Schottky emission were also found in the research of Y. Miyoshi and K. I. Chino<sup>10</sup>. Besides the electron tunneling and the leakage current effect, M. Pollak and J. J. Hauser also developed the electron hopping mechanism to interpret the particular electric properties of thin film<sup>11</sup>. Their theory could describe well for conductivity of the 25~400 nm thin films under different temperature. In this study, the thickness of polymer films was adjusted to discuss the dominating mechanism of electron conduction in the coated polymer nanolayers.

In this research, poly(3-hexylthiophene) (P3HT), which is a common conjugated polymer for solar cells and LEDs, was grafted on the surface of the multi-walled carbon nanotubes (MWCNTs). By adjusting the reaction condition, different P3HT coating thickness of P3HT-grafted MWCNTs were synthesized to study (1) the conductivity and the percolation properties of P3HT-grafted MWCNT/PS composites with different P3HT coating thickness, (2) the P3HT coating thickness effect on contact resistance and (3) the conductive behavior of P3HT layers in nanoscale.

## Experimental

### Materials

The MWCNTs, whose purity is 95 % and the conductivity is higher than  $10^{-2}$  S/cm, were purchased from the Applied Nanotechnologies Inc. to make CNT/polymer composites. The 2-(3-thienylethanol) (3TE) (99%) and the 3-hexylthiophene (3HT) (98%) purchased from Acros Organics were grafted on MWCNTs to study the coating thickness effect on conductivity. The polystyrene (PS) produced by the Pressure Chemical Company was used as the matrix of composites was and the molecular weight is 2M.

### Synthesis of P3HT-grafted MWCNTs

#### Oxidation of MWCNTs<sup>12</sup>

The MWCNTs (1 g) was mixed with  $H_2SO_4$  (95%, 30 ml) and  $HNO_3$  (70%, 20 ml), and refluxed at 150 °C for 1.5 hours to create the carboxyl group (-COOH) on the surface of MWCNTs. The products were washed with deionized water (DI water) until it became neutral and dried in the oven at 80 °C.

#### Grafting 3TE on MWCNTs<sup>13</sup>

The acid-treated MWCNTs (100 mg) were mixed with thionyl chloride ( $SOCl_2$ ) and refluxed at 70 °C for 30 minutes. After taking out the surplus  $SOCl_2$ , 3TE (0.1 ml), pyridine (0.1 ml) and DMAc (10 ml) were added into the flask and reacted for 1 day at 90 °C (Figure 1-a). The products were washed with toluene and chloroform, and then were dried in the oven at 80 °C.

#### Grafting P3HT on MWCNTs

3TE grafted MWCNT (5 mg) and 3HT (0.16 ml) was dispersed in 7.5 ml acetonitrile by ultrasonic cleaner for 3 hours and added into the  $FeCl_3$  (0.325 g) solution which had been dispersed in 2.5 ml acetonitrile. Extra 30 ml chloroform was added into the flask and reacted at 2 °C for half hour. The products were precipitated and washed with methanol to remove the unreacted substance, and then the washed products were dissolved in toluene to remove the ungrafted P3HT. After taking out the ungrafted P3HT by centrifuge, the P3HT-grafted MWCNTs were obtained and the sample name was MWCNT-P3HT-2.

#### Increasing the P3HT coating thickness of P3HT-grafted MWCNTs

MWCNT-P3HT-2 (2 mg) was dispersed in 30 ml chloroform by ultrasonic cleaner for 30 minutes. The  $FeCl_3$  which was dissolved in the mixing solvent of acetonitrile and chloroform was added in the dispersed MWCNT-P3HT-2 solution and reacted at 2 °C. Two different P3HT coating thickness of P3HT-grafted MWCNTs, MWCNT-P3HT-4 and MWCNT-P3HT-8, were produced in this step. For sample MWCNT-P3HT-4, the amount of  $FeCl_3$  is 0.32g, the solvent ratio of acetonitrile to chloroform is 1 to 99 and the reaction time is 30 minutes; for sample MWCNT-P3HT-8, the amount of  $FeCl_3$  is 0.64g, the solvent is chloroform and the reaction time is 24 hours. The products were precipitated and washed with methanol to remove the unreacted substance, and then the washed products were dissolved in toluene to remove the ungrafted P3HT. After taking out the ungrafted P3HT by centrifuge, the thicker P3HT coating MWCNTs, MWCNT-P3HT-4 and MWCNT-P3HT-8, were obtained.

### Characterization of P3HT-grafted MWCNTs and P3HT-grafted MWCNT/polymer composites

The P3HT coating thickness of P3HT-grafted MWCNTs was measured from Perkin-Elmer thermogravimetric analyzer (TGA) and JEOL JEM-2010 transmission electron microscopy (TEM). The P3HT-grafted MWCNTs were blend with different amount of PS ( $M_w = 2M$ ) and drop casted on the conductive indium tin oxide (ITO) glass to measure the resistivity of composites' vertical direction by sandwiching the composite films with another parallel ITO glass. On the other hand, the composites with different amount of PS were also prepared on glass slides to measure the resistivity of

composites' horizontal direction with 4-point probe. The resistivity measurements were carried out with the Keithley 2400 source meter.

## Results and discussion

### *Microscopic observation of P3HT-grafted MWCNTs*

The morphology and the P3HT coating thickness of P3HT-grafted MWCNTs were observed by TEM, which are showed in Figure 2. The grafted P3HT uniformly covers the surface of MWCNTs as polymer thin films and the coating thickness of MWCNT-P3HT-2, MWCNT-P3HT-4 and MWCNT-P3HT-8 are around  $2.1 \pm 0.6$  nm,  $3.6 \pm 1.1$  nm and  $8.3 \pm 1.3$  nm respectively. TGA was used to measure the weight percentage of P3HT and estimate the average P3HT coating thickness. For MWCNT-P3HT-2, MWCNT-P3HT-4 and MWCNT-P3HT-8, the weight percentage of P3HT are 23 wt%, 27 wt% and 50 wt% separately (Figure 3). The average P3HT coating thickness which were estimated from the weight percentage of P3HT are 2.7 nm, 3.5 nm and 7.9nm separately, which are similar to the P3HT coating thickness measured from TEM.

### *Anisotropic properties of P3HT-grafted MWCNT/PS composite films*

The resistivity of P3HT-grafted MWCNT/PS composite films in vertical and horizontal direction with different percentage of P3HT-grafted MWCNTs were measured and fitted with percolation scaling law<sup>14</sup>,

$$\rho = \rho_0 (\phi - \phi_c)^{-t} \quad (1)$$

where  $\rho$  is the resistivity of composite films,  $\rho_0$  is the resistivity of net P3HT-grafted MWCNT films,  $\phi$  is the weight percentage of P3HT-grafted MWCNTs,  $\phi_c$  is the percolation threshold of composite films and  $t$  is the conductivity exponent. The fitting results are showed in Figure 4 and Figure 5, and the number of fitted  $\rho_0$ ,  $\phi_c$  and  $t$  are summarized in Table 1 and 2. There are two different properties of composites in vertical and horizontal direction. Firstly, the resistivity of composites in vertical direction is 3 orders higher than it in horizontal direction. Secondly, the percolation threshold of composites in vertical direction is higher than it in horizontal direction.

For the SEM cross-section micrographs of MWCNT/PS composite films, which are showed in Figure 6-a and 6-b, the film surface is indicated on the top right of the micrograph and the P3HT-grafted MWCNTs are exposed on the cross-section of composite. Under higher magnification, we found that the orientation of P3HT-grafted MWCNTs in the composites is not isotropic but parallel to the film surface. Due to the horizontal arrangement of P3HT-grafted MWCNTs, the density of contact points in vertical direction is higher than it in horizontal direction, which means that electrons have to pass through more contact points of P3HT-grafted MWCNTs when electrons transport along the vertical direction of composite films (Figure 6-c and 6-d). Therefore, the resistivity of vertical direction is much higher than it of horizontal direction. For the same reason, since the P3HT-grafted MWCNTs lay on the horizontal plane of composites, they easily form a percolation cluster to connect two boundaries of composites in horizontal direction. In vertical direction, however, the percolation clusters are hard to form by the horizontally arranged P3HT-grafted MWCNTs. Therefore, the percolation threshold of vertical direction is higher than it of horizontal direction.

### *The P3HT coating thickness effect on the resistivity of P3HT-grafted MWCNT/PS composite films*

To study the P3HT coating thickness effect on the resistivity of composite films, the resistivity of P3HT-grafted MWCNT films in different directions ( $\rho_{0,v}$  and  $\rho_{0,h}$ ) are showed as a function of P3HT coating thickness. From Figure 7, the resistivity of P3HT-grafted MWCNT films exponentially increases with P3HT coating thickness. Assume the resistivity of composite films is mainly dominated by the contact resistance ( $R_c$ ). Contact resistance is consisted of the resistance of coated P3HT ( $R_{P3HT}$ ), which is proportional to the P3HT coating thickness ( $t_{P3HT}$ ). Therefore, the resistivity of composites should be proportional to the P3HT coating thickness.

$$\rho_{\text{composite}} \propto R_c \approx R_{P3HT} \propto t_{P3HT} \quad (2)$$

In Figure 7, however, the resistivity of composites is not proportional but exponential to the P3HT coating thickness. We think this phenomenon may come from the variation of the resistivity of P3HT in the nanoscale. To figure out the physical origin of this phenomenon, the electrical resistivity of grafted P3HT nanolayers was discussed in the following.

In order to estimate the resistivity of grafted P3HT nanolayers, contact resistance has to be calculated first. By dividing the number of contact points, contact resistance could be obtained from the resistance of percolation cluster. The resistance of percolation cluster was estimated from the resistivity of P3HT-grafted MWCNT films. Therefore, the resistivity of grafted P3HT nanolayers could be obtained.

To estimate the number of contact points, the orientation of the P3HT-grafted MWCNTs was considered. Considering a CNT in the three-dimensional space (Figure 8-a), X-Y plane is the plane paralleling to the film surface, Z axis is vertical to the film surface,  $\varphi$  is the angle between Z axis and the CNT,  $\theta$  is the angle between X axis and the CNT projection on X-Y plane, and  $l_i$  is the length of the CNT. The Boltzmann distribution, which is often used to describe the orientation distribution of stretched polymer segments, was used to describe the distribution of orientation angle,  $\varphi$ , in the films. The possibility distribution is given by

$$p \propto e^{\frac{E_i}{kT}} \quad (3)$$

$p$  is the possibility,  $E_i$  is the applied energy,  $k$  is the Boltzmann constant and  $T$  is the temperature. Assume there is the tensile force on X-Y plane ( $F_{xy}$ ) which let CNT lie on the X-Y plane. The energy  $E_i$  which is provided by  $F_{xy}$  is

$$-F_{xy} l_i / \cos(90^\circ - \varphi) \quad (4)$$

The number of contact points per unit length along a specific direction is similar to the number of CNTs per unit length along that specific direction. The reciprocal of the number of CNTs per unit length is the projection length of one CNT along that specific direction. Therefore, if the projection length is estimated, the number of contact points per unit length along the specific direction could be obtained. Considering the Boltzmann distribution of orientation, the average projection length along Z axis,  $\langle l_{i,z} \rangle$ , is

$$\langle l_{i,z} \rangle = \frac{\int_0^\pi l_i |\cos \varphi| \cdot \exp(-F_{xy} l_i |\sin \varphi| / kT) \cdot (2\pi \sin \varphi) d\varphi}{\int_0^\pi \exp(-F_{xy} l_i |\sin \varphi| / kT) \cdot (2\pi \sin \varphi) d\varphi} \quad (5)$$

and the average projection length along any direction on X-Y plane,  $\langle l_{i,xy} \rangle$ , is

$$\langle l_{i,xy} \rangle = \frac{\int_0^{2\pi} \int_0^\pi l_i |\sin \varphi| \cdot \exp(-F_{xy} l_i |\sin \varphi| / kT) \cdot (2\pi \sin \varphi) \cdot \cos \theta d\varphi d\theta}{\int_0^{2\pi} \int_0^\pi \exp(-F_{xy} l_i |\sin \varphi| / kT) \cdot (2\pi \sin \varphi) d\varphi d\theta} \quad (6)$$

Therefore, the number of contact points per unit length along Z axis and any direction on X-Y plane could be estimated.

The CNTs were stacked to simulate a percolation cluster in composite films along Z axis (Figure 8-b), the height of the percolation cluster is  $L_z$  and the diameter of the percolation cluster is about  $\langle l_{i,xy} \rangle$ . Therefore, the resistance of a percolation cluster along Z axis was estimated by

$$R_z = \rho_{0,z} \frac{L_z}{A_{xy}} = \rho_{0,z} \frac{L_z}{(\langle l_{i,xy} \rangle / 2)^2 \pi} \quad (7)$$

The resistance of a percolation cluster is dominated by contact resistance and the number of contact points along Z axis is  $L_z / \langle l_{i,z} \rangle$ . Therefore, the resistance of a percolation cluster along Z axis could also be expressed by

$$\rho_{0,z} \frac{L_z}{(\langle l_{i,xy} \rangle / 2)^2 \pi} = \frac{L_z}{\langle l_{i,z} \rangle} \cdot R_c \quad (8)$$

and the contact resistance was obtained. By the same method, the resistance of a percolation cluster along X-Y plane was given by

$$\rho_{0,xy} \frac{L_{xy}}{\langle l_{i,xy} \rangle \langle l_{i,z} \rangle} = \frac{L_{xy}}{\langle l_{i,x} \rangle} \cdot R_c \quad (9)$$

However,  $R_c$  which was estimated from different direction should be the same.  $F_{xy}$  was adjusted to approximate  $R_c$  from vertical and horizontal direction of composite films. Due to contact resistance is consisted of coated P3HT, the resistivity of grafted P3HT nanolayers ( $\rho_{P3HT}$ ) was calculated from  $R_c = \rho_{P3HT} (2t_{P3HT}/A_{contact})$ ,  $t_{P3HT}$  is the P3HT coated thickness and  $A_{contact}$  is the contact area of CNTs,

which is approximated by the square of MWCNTs' diameter<sup>6</sup>. The estimated  $R_c$  and  $\rho_{P3HT}$  are showed in Table 3. The  $R_c$  of CNTs without P3HT coating is the contact resistance of CNTs. The contact resistance that we estimated is similar to the contact resistance which was reported<sup>15</sup>. Plotting the resistivity of grafted P3HT nanolayers as a function of coating thickness (Figure 9), we found that the resistivity of grafted P3HT nanolayers exponentially decrease with reducing coating thickness and it is lower than the resistivity of bulk P3HT<sup>16,17</sup>.

On the other hand, P3HT thin films were prepared on conductive ITO glass by spin coating. The resistivity of P3HT films in vertical direction was measured by sandwiched with conductive ITO glasses, which was used to simulate the situation of grafted P3HT. In Figure 10, the resistivity of spin-coated P3HT thin films exponentially decrease with reducing the film thickness from 100 nm to 5nm and it is also lower than the resistivity of P3HT bulk. Therefore, we infer that variation of resistivity is because of the films thickness effect.

The electron vertical hopping conduction of the thin film was introduced by Pollack and Hauser<sup>11</sup> and developed by Raikh and Ruzin<sup>18</sup>. In their study, the resistivity of thin films in vertical direction is mainly consisted by the resistance of each hopping and the developing possibility of conductive percolation clusters in thin film<sup>18</sup>. The developing possibility of conductive percolation cluster exponentially increases with reducing film thickness and more electrons can pass through the thin film. Therefore, the resistivity of thin films is decreasing. The conductivity of thin films in vertical direction is described by

$$\sigma = \sigma_0 \exp(-2\sqrt{\frac{2L\lambda_T}{a}}) \quad (10)$$

where  $\sigma_0$  is the conductivity prefactor (for P3HT,  $\sigma_0 = 1.6 \times 10^4$  S/cm)<sup>19</sup>,  $L$  is the film thickness,  $\lambda_T = \ln \lambda_T - \ln(g_0 k T a L^2) \approx -\ln(g_0 k T a L^2)$ ,  $g_0$  is the density of localized states,  $k$  is the Boltzmann constant,  $T$  is the temperature and  $a$  is the localization radius. After rearranging, the equation (10) becomes

$$\frac{[\ln(\sigma/\sigma_0)]^2}{L} \approx -\frac{16}{a} \ln L - \frac{8}{a} \ln(g_0 k T a) \quad (11)$$

The resistivity of grafted P3HT nanolayers and spin-coated P3HT thin films were used to plot  $[\ln(\sigma/\sigma_0)]^2/L$  as a function of  $\ln L$  and fitted with straight lines. The result is showed in Figure 11. From the slope of straight fitting line, the localization radius,  $a$ , was obtained. The localization radius for grafted P3HT nanolayers is 0.8 nm and for spin-coated P3HT thin films is 0.7 nm, and both of them are compatible with the localization radius of P3HT that has been reported<sup>20-22</sup>. Thus, the conductive behavior of the P3HT grafted on MWCNT is mainly dominated by the electron hopping mechanism. The little difference between the resistivity of grafted P3HT nanolayers and spin coated P3HT may come from the interaction between P3HT and MWCNT<sup>16,23</sup>. This interaction will affect the localization situation of P3HT grafted MWCNTs<sup>24</sup>, and therefore the resistivity of grafted P3HT nanolayers and spin-coated P3HT thin films are little different. In addition of electron hopping mechanism, electron tunneling, Schottky emission and Poole-Frenkel emission, which are usually considered for conductive behavior of electric device, were also discussed for our system.

The tunneling current at the contact point of two CNTs is given by

$$I_i = c \rho_A \rho_B \exp(-Lk) \quad (12)$$

where  $c$  is a constant,  $\rho_A$  and  $\rho_B$  are the density of states for the two contacted CNTs,  $L$ , which is the double of coating thickness, is the distance between the contacted CNTs and  $k$  is given by

$$k = \frac{\sqrt{2m(V_0 - E)}}{\hbar} \quad (13)$$

where  $m$  is the electron mass,  $V_0$  is the energy barrier between two CNTs,  $E$  is the active energy. Therefore, the contact resistance ( $R_c$ ) is described by

$$R_c = \frac{V_i}{I_i} = \frac{V_i}{c \rho_A \rho_B e^{-Lk}} = a e^{Lk} \quad (14)$$

where  $a$  is the constant. After rearranging, equation (14) becomes

$$\ln(R_c) = kL + \ln(a) \quad (15)$$

The  $\ln(R_c)$  was plotted as a function of  $L$  and fitted by the straight line to obtain the slope  $k$ . The slope ( $k$ ) of fitting straight line is 0.62 (Figure 12). The work function of MWCNT is 5.2 eV and the lowest

unoccupied molecular orbital (LUMO) of P3HT is 3.2 eV. Thus, the energy barrier  $V_0$  is about 2 eV. Converted with  $k$ , the active energy  $E$  for one electron is 1.93 eV. In other words, the voltage difference at the contact point between two contacted MWCNTs is 1.93 V, which is much higher than the applied voltage (0.1 mV). The fitted result is unreasonable. Therefore, electron tunneling is not the main mechanism which dominates the conductive behavior of grafted P3HT nanolayers.

The current of Schottky emission is described by<sup>25</sup>

$$I \propto \exp\left[\frac{-q\Phi_B + q\sqrt{qV/4\pi L\epsilon_0\epsilon_r}}{kT}\right] \propto \frac{1}{R_c} \quad (16)$$

For Poole-Frenkel emission, the current is described by

$$I \propto \frac{1}{L} \exp\left[\frac{-q\Phi_B + q\sqrt{qV/\pi L\epsilon_0\epsilon_r}}{kT}\right] \propto \frac{1}{R_c} \quad (17)$$

where  $I$  is the current,  $q$  is the electron charge,  $\Phi_B$  is the energy barrier,  $V$  is the voltage,  $L$ , which is the double of coating thickness, is the distance between contacted CNTs,  $\epsilon_0$  is the vacuum permittivity ( $8.85 \times 10^{-12}$  A·s/(V·m)),  $\epsilon_r$  is the relative permittivity of P3HT,  $k$  is the Boltzmann constant and  $T$  is the temperature. After arranging, the equation (16) becomes

$$\ln\left(\frac{I}{R_c}\right) = \frac{q\sqrt{qV/4\pi\epsilon_0\epsilon_r}}{kT} \cdot \frac{1}{\sqrt{L}} + \text{constant} \quad (18)$$

For Poole-Frenkel emission, the equation (17) becomes

$$\ln\left(\frac{L}{R_c}\right) = \frac{q\sqrt{qV/\pi\epsilon_0\epsilon_r}}{kT} \cdot \frac{1}{\sqrt{L}} + \text{constant} \quad (19)$$

$\ln(I/R_c)$  and  $\ln(L/R_c)$  was respectively plotted as a function of  $L^{-1/2}$  and fitted by the straight lines. For Schottky emission, the slope of the fitting straight line is 32.6; for Poole-Frenkel emission, the slope of the fitting straight line is 26.9 (Figure 13). Since the  $\epsilon_r$  of P3HT is 6.5<sup>26</sup>, the required voltage for Schottky emission and Poole-Frenkel emission was obtained from the slope of fitting line. For Schottky emission, the required voltage is 54.5 V; for Poole-Frenkel emission, the required voltage is 82.6 V. Both of them are higher than the applied voltage. Therefore, the Schottky emission and Poole-Frenkel emission were also not the main mechanism that dominated the conductive behavior of grafted P3HT nanolayers. In conclusion, electron tunneling, Schottky emission and Poole-Frenkel emission would not dominate the conduction of grafted P3HT nanolayers.

## Conclusions

Different thickness of P3HT nanolayers were coated on MWCNTs by two steps synthesis and controlling the reaction condition. The resistivity of P3HT-grafted MWCNT/PS composites in vertical and horizontal direction were measured and described by percolation scaling law. Since the P3HT-grafted MWCNTs lied on the horizontal plane of composite films, the resistivity of composites in vertical direction was three orders higher than it in horizontal direction. In addition, the percolation threshold of composites in vertical direction is also higher than it in horizontal direction. By the Boltzmann distribution and the unit projection length, the contact resistance was approximated from the resistivity of composites in vertical and horizontal direction, and the resistivity of grafted P3HT nanolayers was also obtained. The resistivity of grafted P3HT nanolayers for the thickness of 2.1 nm, 3.6 nm and 8.3 nm was  $7.0 \times 10^2$  Ω·cm,  $5.5 \times 10^3$  Ω·cm and  $1.1 \times 10^6$  Ω·cm respectively, which exponentially decreased with reducing the coating thickness and was lower than the resistivity of the P3HT bulk. The same conductive behavior was also found in spin-coated P3HT thin films. This phenomenon was due to that the electron hopping mechanism dominated the conductive behavior of polymer films in nanoscale, and the possibility of forming electron percolation routes exponentially increases when the electron transport distance (i.e. the film thickness) reduced. This research provided not only a method to measure the resistivity of polymer nano-thin films, but also the possible dominating mechanism of the conductive behavior in nanoscale thin films, which may assist us to figure out the electrical properties of polymer thin film devices such as thin-film transistors (TFTs), solar cells and LEDs.

## References

1. Wu, Z. C.; Chen, Z. H.; Du, X.; Logan, J. M.; Sippel, J.; Nikolou, M.; Kamaras, K.; Reynolds, J. R.; Tanner, D. B.; Hebard, A. F.; Rinzler, A. G. *Science* **2004**, *305*, 1273.
2. Raffaele, R. P.; Landi, B. J.; Harris, J. D.; Bailey, S. G.; Hepp, A. F. *Mat Sci Eng B-Solid* **2005**, *116*, 233.
3. Zhang, M.; Fang, S. L.; Zakhidov, A. A.; Lee, S. B.; Aliev, A. E.; Williams, C. D.; Atkinson, K. R.; Baughman, R. H. *Science* **2005**, *309*, 1215.
4. Hirsch, A. *Angew Chem Int Edit* **2002**, *41*, 1853.
5. Hecht, D.; Hu, L. B.; Gruner, G. *Appl. Phys. Lett.* **2006**, *89*.
6. Li, C. Y.; Thostenson, E. T.; Chou, T. W. *Appl. Phys. Lett.* **2007**, *91*.
7. Beyer, V.; Schmidt, B.; Heinig, K. H.; Stegemann, K. H. *Appl. Phys. Lett.* **2009**, *95*.
8. Glezos, N.; Argitis, P.; Velessiotis, D.; Diakoumakos, C. D. *Appl. Phys. Lett.* **2003**, *83*, 488.
9. Liang, T.; Makita, Y.; Kimura, S. *Polymer* **2001**, *42*, 4867.
10. Miyoshi, Y.; Chino, K. I. *Jpn J Appl Phys* **1967**, *6*, 181.
11. Pollak, M.; Hauser, J. J. *Phys. Rev. Lett.* **1973**, *31*, 1304.
12. Lin, T. S.; Cheng, L. Y.; Hsiao, C. C.; Yang, A. C. M. *Mater. Chem. Phys.* **2005**, *94*, 438.
13. Philip, B.; Xie, J. N.; Chandrasekhar, A.; Abraham, J.; Varadan, V. K. *Smart Materials & Structures* **2004**, *13*, 295.
14. Stauffer, D.; Aharony, A. *Introduction to percolation theory* Taylor and Francis: 1994.
15. Fuhrer, M. S.; Nygard, J.; Shih, L.; Forero, M.; Yoon, Y. G.; Mazzoni, M. S. C.; Choi, H. J.; Ihm, J.; Louie, S. G.; Zettl, A.; McEuen, P. L. *Science* **2000**, *288*, 494.
16. Kuila, B. K.; Malik, S.; Batabyal, S. K.; Nandi, A. K. *Macromolecules* **2007**, *40*, 278.
17. Musumeci, A. W.; Silva, G. G.; Liu, J. W.; Martens, W. N.; Waclawik, E. R. *Polymer* **2007**, *48*, 1667.
18. Altshuler, B. L.; Lee, P. A.; Webb, R. A. *Mesoscopic Phenomena in Solids* 1991; Vol. 30.
19. Meijer, E. J.; Tanase, C.; Blom, P. W. M.; van Veenendaal, E.; Huisman, B. H.; de Leeuw, D. M.; Klapwijk, T. M. *Appl. Phys. Lett.* **2002**, *80*, 3838.
20. Emelianova, E. V.; van der Auweraer, M.; Adriaenssens, G. J.; Stesmans, A. *Org. Electron.* **2008**, *9*, 129.
21. Arkhipov, V. I.; Heremans, P.; Emelianova, E. V.; Adriaenssens, G. J.; Bassler, H. *Appl. Phys. Lett.* **2003**, *82*, 3245.
22. Shimotani, H.; Diguet, G.; Iwasa, Y. *Appl. Phys. Lett.* **2005**, *86*.
23. Geng, J. X.; Zeng, T. Y. *J. Am. Chem. Soc.* **2006**, *128*, 16827.
24. Dobrosavljevic, V.; Stratt, R. M. *Phys Rev B* **1987**, *35*, 2781.
25. Chiu, F. C.; Wang, J. J.; Lee, J. Y.; Wu, S. C. *J. Appl. Phys.* **1997**, *81*, 6911.
26. Estrada, M.; Mejia, I.; Cerdeira, A.; Iniguez, B. *Solid-State Electronics* **2008**, *52*, 53.

| Sample                      | $\rho_{0,v}$ ( $\Omega\text{-cm}$ ) | $\phi_{c,v}$ (wt%) | $t_v$ |
|-----------------------------|-------------------------------------|--------------------|-------|
| <b>MWCNT</b>                | $9.2 \times 10^1$                   | 8.1                | 3.4   |
| <b>MWCNT-P3HT-2 (2.1nm)</b> | $4.2 \times 10^5$                   | 9.1                | 3.4   |
| <b>MWCNT-P3HT-4 (3.6nm)</b> | $4.5 \times 10^6$                   | 9.4                | 2.3   |
| <b>MWCNT-P3HT-8 (8.3nm)</b> | $7.1 \times 10^8$                   | 9.4                | 1.4   |

Table 1. The  $\rho_0$ ,  $\phi_c$  and  $t$  of composites in vertical direction

Table 2. The  $\rho_0$ ,  $\phi_c$  and  $t$  of composites in horizontal direction

| Sample                      | $\rho_{0,h}$ ( $\Omega\text{-cm}$ ) | $\phi_{c,h}$ (wt%) | $t_h$ |
|-----------------------------|-------------------------------------|--------------------|-------|
| <b>MWCNT</b>                | $4.9 \times 10^{-2}$                | 0.005              | 3.2   |
| <b>MWCNT-P3HT-2 (2.1nm)</b> | $1.9 \times 10^2$                   | 0.001              | 3.2   |
| <b>MWCNT-P3HT-4 (3.6nm)</b> | $2.0 \times 10^3$                   | 0.003              | 3.2   |
| <b>MWCNT-P3HT-8 (8.3nm)</b> | $8.0 \times 10^5$                   | 0.001              | 2.3   |

| <b>Coating Thickness</b> | <b><math>R_c (\Omega)</math></b> | <b><math>\rho_{P3HT} (\Omega\cdot\text{cm})</math></b> |
|--------------------------|----------------------------------|--|
| <b>0 nm</b>              | $1.2 \times 10^4$                |  |
| <b>2.1 nm</b>            | $5.0 \times 10^7$                | $7.0 \times 10^2$                                      |
| <b>3.6 nm</b>            | $5.3 \times 10^8$                | $5.5 \times 10^3$                                      |
| <b>8.3 nm</b>            | $1.3 \times 10^{11}$             | $1.1 \times 10^6$                                      |

Table 3. The  $R_c$  and  $\rho_{P3HT}$  for different P3HT coating thickness

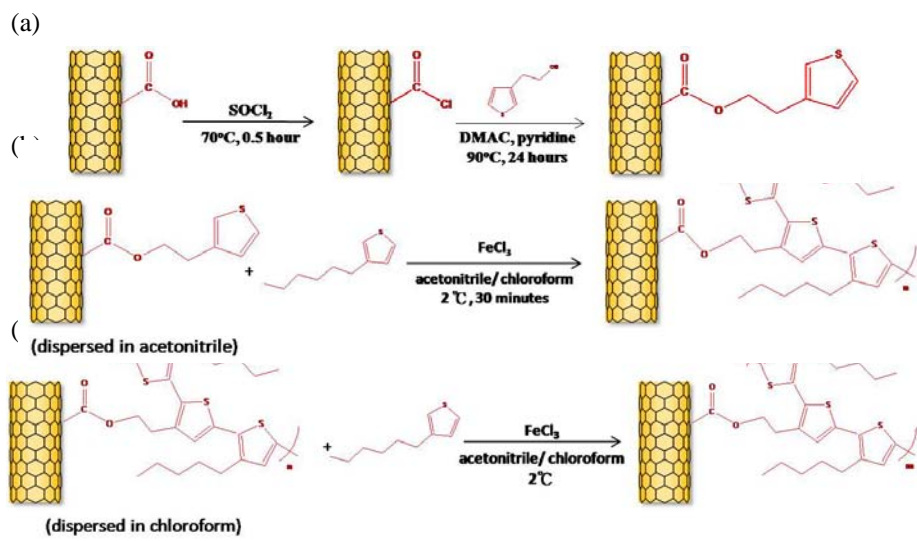


Figure 1. (a) Grafting 3TE on MWCNTs (b) Grafting P3HT on MWCNTs (sample: MWCNT-P3HT-2) (c) Increasing the P3HT coating thickness of P3HT-grafted MWCNTs (sample: MWCNT-P3HT-4 and MWCNT-P3HT-8)

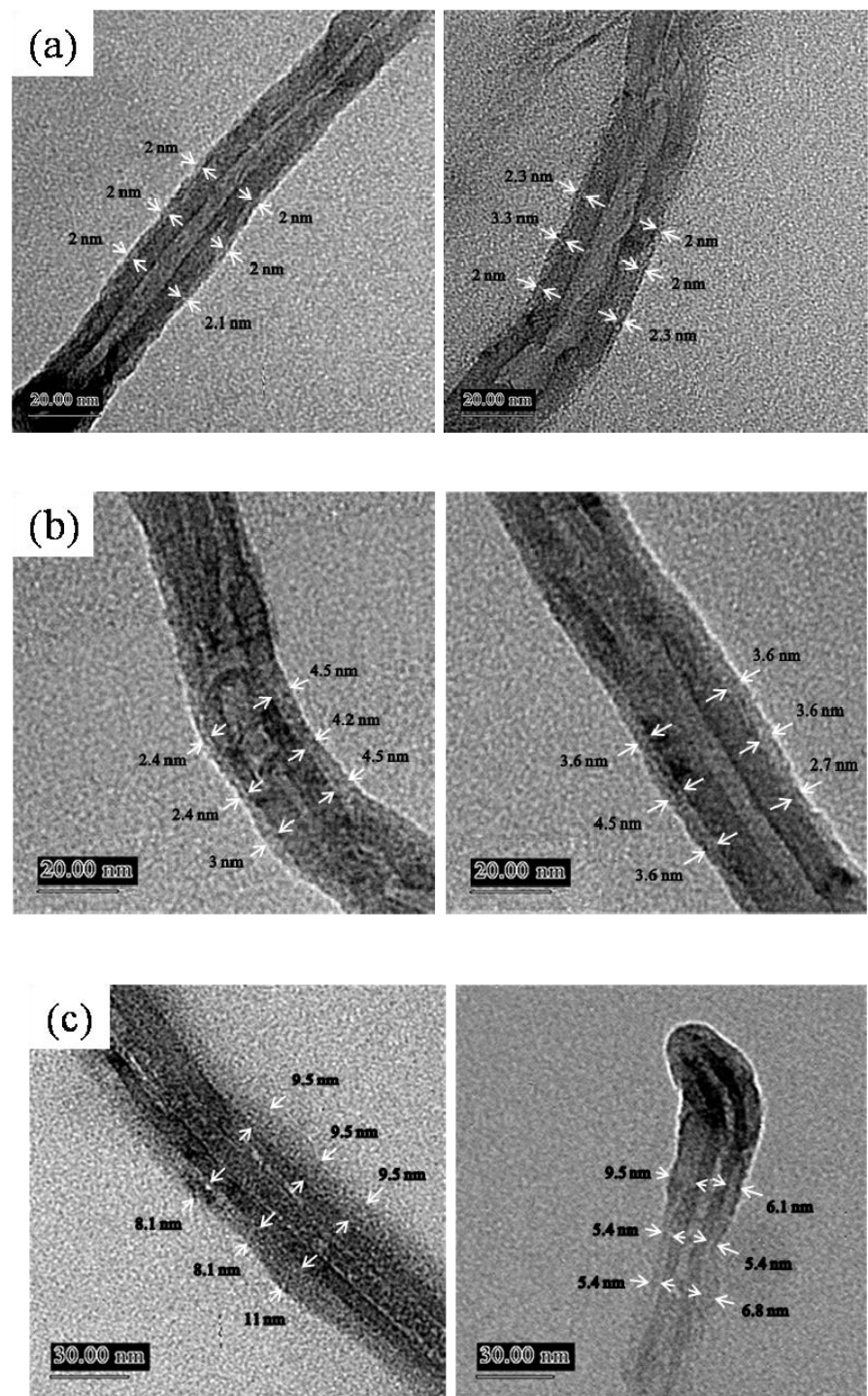


Figure 2. TEM micrographs of the P3HT-grafted MWCNTs (a) MWCNT-P3HT-2 (b) MWCNT-P3HT-4 (c) MWCNT-P3HT-8.

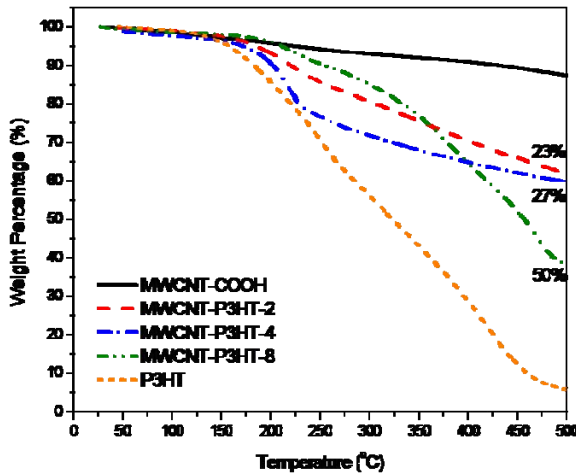


Figure 3. TGA curves of acid-treated MWCNT (MWCNT-COOH), MWCNT-P3HT-2, MWCNT-P3HT-4, MWCNT-P3HT-8 and P3HT with a heating rate of 10 °C / min under argon.

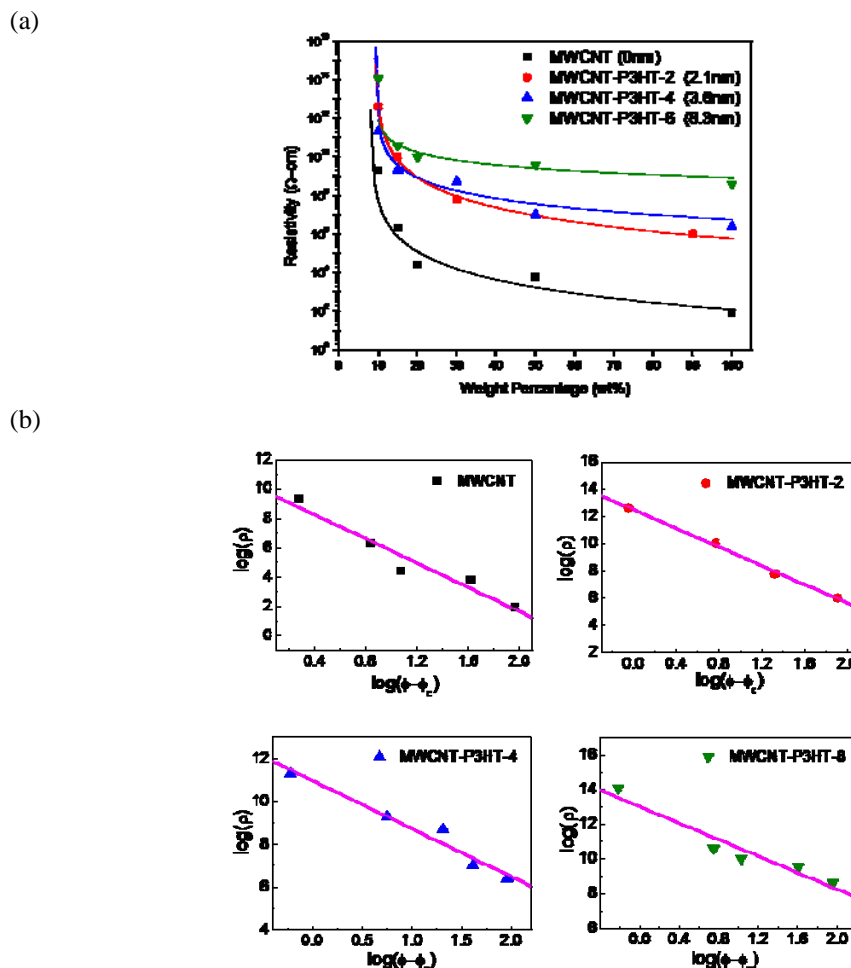
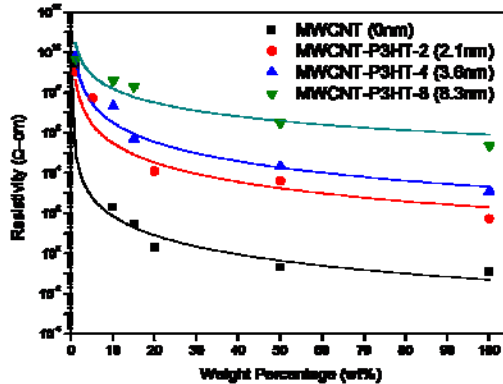


Figure 4. (a) The semi-log plot shows the resistivity of composite films in vertical direction as a function of weight percentage of P3HT-grafted MWCNTs. (b) The plots, which were fitted with percolation scaling law, show  $\log \rho$  of vertical direction as a function of  $\log (\phi - \phi_c)$  for different P3HT coating thickness.

(a)



(b)

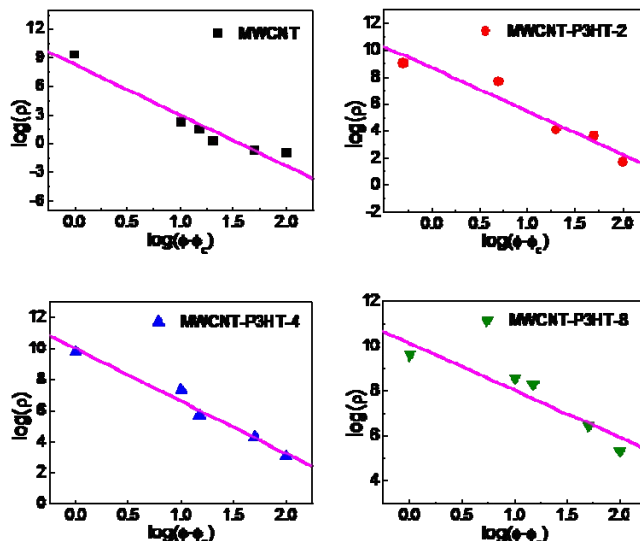


Figure 5. (a) The semi-log plot shows the resistivity of composite films in horizontal direction as a function of weight percentage of P3HT-grafted MWCNTs. (b) The plots, which were fitted with percolation scaling law, show  $\log \rho$  of horizontal direction as a function of  $\log (\phi - \phi_c)$  for different P3HT coating thickness.

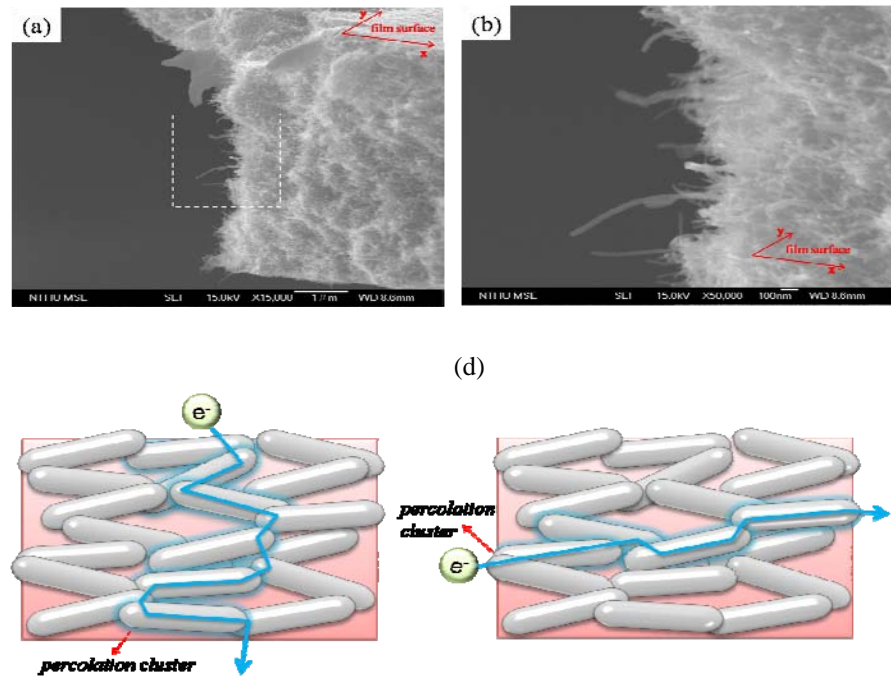


Figure 6. (a) The SEM micrograph shows the cross-section of the composite with 90wt% P3HT-grafted MWCNTs and the film surface is indicated on the top right of the micrograph (b) Under higher magnification, the micrograph shows that the P3HT-grafted MWCNTs are parallel to the film surface. (c) The conductive and percolation properties of P3HT-grafted MWCNT/PS composite films for electrons transporting along the percolation cluster in vertical direction (d) for electrons transporting along the percolation cluster in horizontal direction.

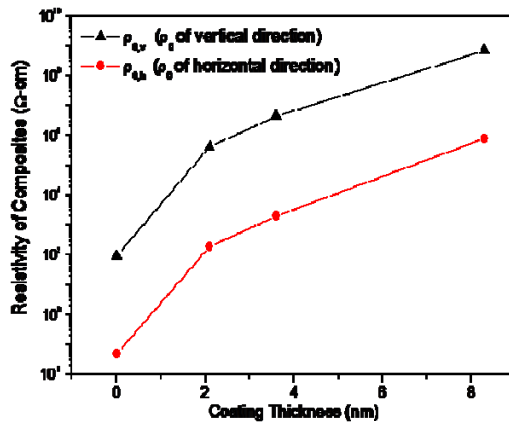


Figure 7. The resistivity of P3HT-grafted MWCNT films in vertical and horizontal direction are showed as an exponential function of P3HT coating thickness.

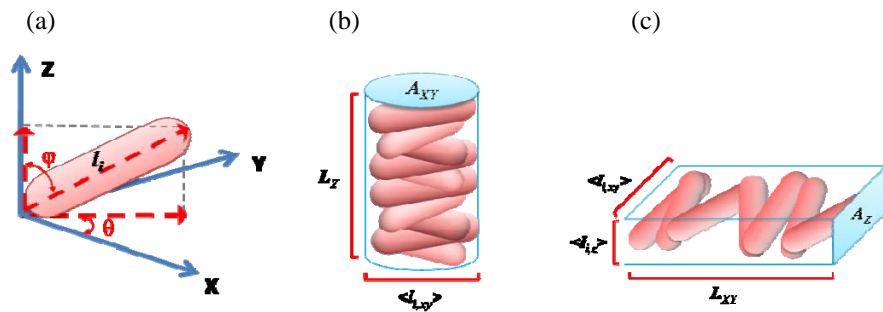


Figure 8. (a) The CNT in 3-D space: X-Y plane is the plane paralleling to the film surface, Z axis is vertical to the film surface,  $\phi$  is the angle between Z axis and the CNT,  $\theta$  is the angle between X axis and the CNT projection on X-Y plane, and  $l_i$  is the length of the CNT. (b) The CNTs are stacked to simulate a percolation cluster in composite films along Z axis and (c) X-Y plane.

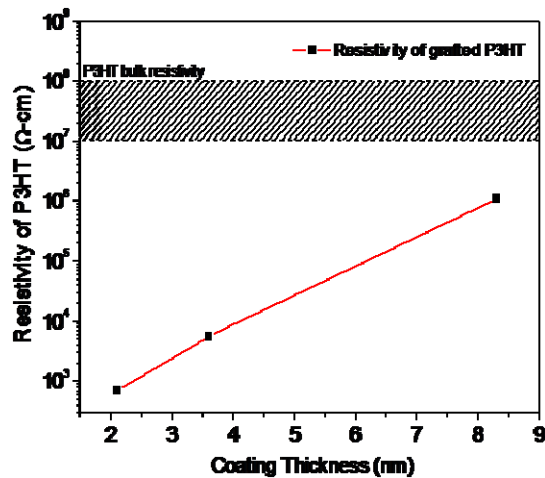


Figure 9. The resistivity of grafted P3HT nanolayers is showed as a function of coating thickness: the resistivity exponentially decreases with reducing the coating thickness and it is lower than the resistivity of bulk P3HT.

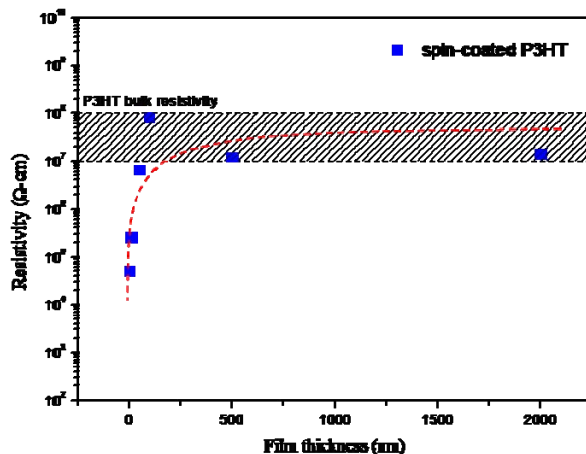


Figure 10. The semi-log plot shows the resistivity of spin-coated P3HT thin films as a function of film thickness: the resistivity exponentially decreases with reducing the film thickness from 100 nm to

5nm and it is also lower than the resistivity of P3HT bulk.

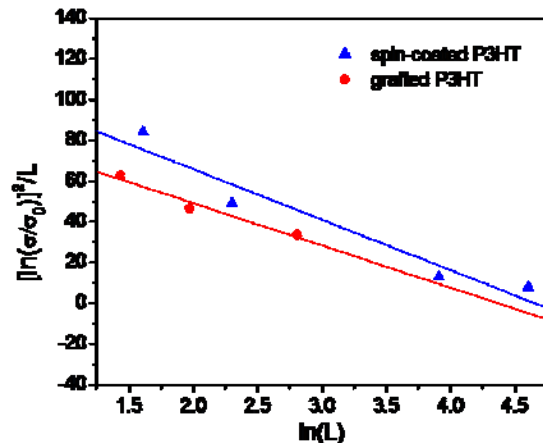


Figure 11. The resistivity of grafted P3HT nanolayers and spin-coated P3HT thin films were used to plot  $[\ln(\sigma/\sigma_0)]^2/L$  as a function of  $\ln L$  and fitted by straight lines. The slope of fitting line for spin-coated P3HT thin films is -24 and for grafted P3HT nanolayers is -20.

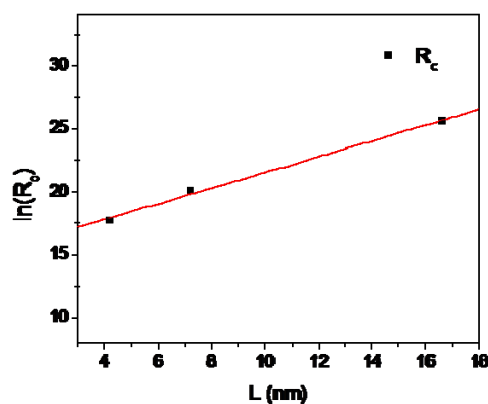


Figure 12. The  $\ln(R_c)$  was plotted as a function of  $L$  and fitted by the straight line. The slope ( $k$ ) of the fitting straight line is 0.62.

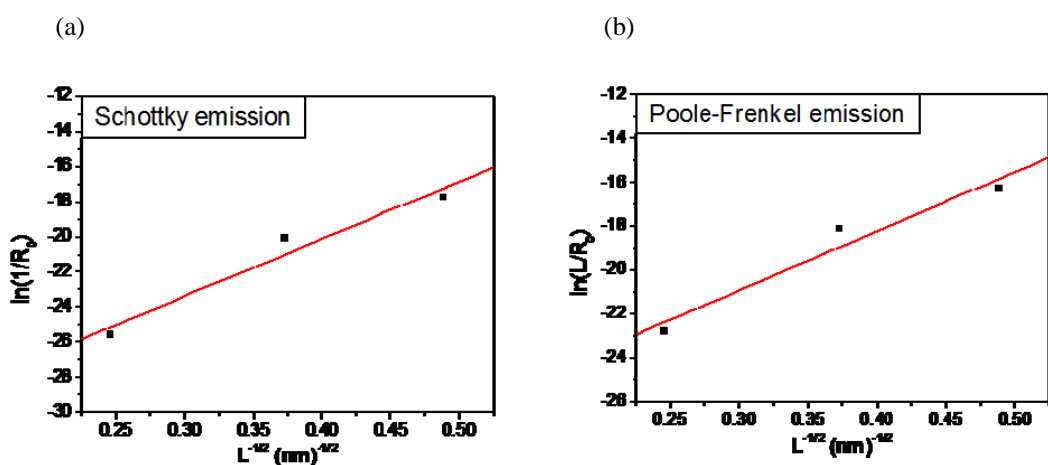


Figure 13.  $\ln(I/R_c)$  and  $\ln(L/R_c)$  was respectively plotted as a function of  $L^{-1/2}$  and fitted by the straight lines. The slope of plot (a) is 32.6 and it of plot (b) is 26.9.

## SECTION 7

### Nano-Plastic Flows in Rigid-Rod Polybenzoxazole and the Molecular Reinforcement via Interactions with Surface-Grafted Carbon Nanotubes

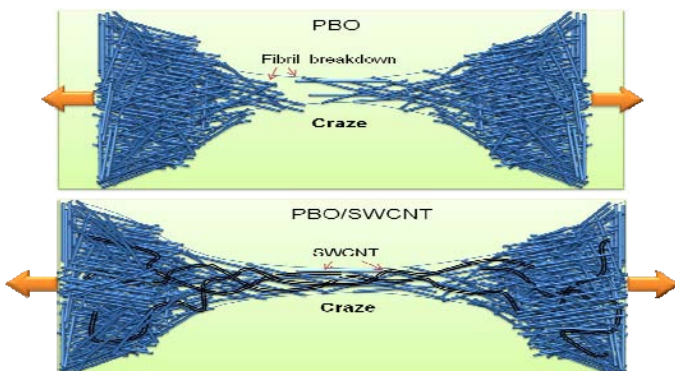
Chih-Wei Lin<sup>1</sup>, Anthony C.-Y. Chou<sup>1</sup>, Steve L.-C. Hsu<sup>2</sup>, Arnold C.-M. Yang<sup>1\*</sup>

<sup>1</sup>Department of Materials Science and Engineering National Tsing Hua University, Hsinchu, Taiwan

<sup>2</sup>Department of Materials Science and Engineering National Cheng Kung University, Tainan, Taiwan

#### Abstract:

Despite the ultrahigh glass transition temperature well over 600°C, the wholly aromatic rigid-rod polybenzoxazoles (PBO) (M.W.= 43kg/mol.) flowed into large deformations (~300%) when stressed at ambient condition, forming local deformation zones of crazes. Local drawing in the amorphous regions by a stress determined to be ~3 GPa was observed to dominate the nano-plastic flows. The drawing stress, however, was insufficient to separate the crystalline chain segments. The nano-plastic flows were soon superseded by fibril breakdown, manifesting low extensibilities below 2%. Yet, the crystallites were not sources of weakness as craze fibril stability remained unchanged in the quasi-amorphous films. When incorporated with the surface-grafted carbon nanotubes (CNTs), polymer-CNT interactions took place that extensively modified the crystalline structures. While no reinforcement effects were observed by the multi-walled (MWCNTs) that were too rigid to take part in the flows, the flexible single-walled CNTs (SWCNTs) advanced dramatically the extensibility of the rigid chains via a CNT-mediated chain-coupling effect. This work illustrates the important role of CNT-polymer interactions during the nano-plastic flows for the molecular reinforcement in rigid-rod glassy polymers.



#### Introduction

Noted for their extremely high elastic modulus (>270 GPa), excellent chemical resistance, outstanding fiber-drawing capability, and exceptional thermal stability with decomposition temperature above 650°C, the aromatic polybenzoxazoles (PBOs) have attracted intense interest for advanced applications.<sup>1-5</sup> The polymers exhibit excellent chain ordering in thin solid films owing to their rigid molecular architectures while their glass transition and melting points are very close to their thermal decomposition ones. PBOs were prepared by one-step polycondensation of bis(o-aminophenol)s with aromatic diacid in poly(phosphoric acid) (PPA), or a two-step process of thermal cyclization from polyhydroxyamides (PHAs).<sup>6-10</sup> Owing to the solubility difference between the bi-functional monomers (e.g., diol and diacid) in polymerization solvents (e.g., PPA), high molecular weights of PBO's were generally difficult to obtain.<sup>7,9,10</sup>

Despite their superior strength, the rigid-rod polymers manifest low elongations at break (around 1-2%), making them highly susceptible to brittle fracturing under large stresses. Generally, glassy polymers are known to undergo plastic deformation upon stretching by growing tiny local deformation zones after passing the brief elastic regime. During the chain flowing processes, the polymer chains are drawn by local necking to large molecular strains limited by chain entanglement networks. When these deformation zones breakdown to initiate voids, catastrophic fractures soon ensue.<sup>11-20</sup> Obviously, the stability of the nano-plastic processes dictates the mechanical stability of the

glassy polymers. In the past, with PBOs of strong chain-ordering characteristics almost intractable for film preparation, no prior work has been directed to reveal their intrinsic nano-plastic flow properties.<sup>5,21-26</sup>

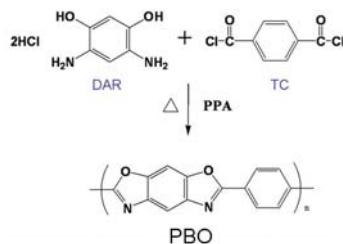
Using carbon nanotubes (CNTs) to reinforce polymers has long been attempted.<sup>5,21-26</sup> The detailed interactions between CNTs and glassy polymer chains were investigated,<sup>18-20</sup> as a function of chain entanglement density ( $\nu_e$ ), in the brittle (crazing<sup>18-20</sup>) and ductile (shear yielding<sup>19-20</sup>) nano-plastic flows using polystyrene (PS) and polyphenylene oxide (PPO) respectively as the model polymers. It was found that CNTs incorporation always enhanced the elastic modulus and the materials strength, but only strain-hardened chains were able to pull CNTs into the nano-plastic flows for effective load-bearing and hence reinforcement.<sup>19</sup> Within the time and space scales allowed during the micro-necking of local deformation at the ambient condition, the critical condition for strain hardening seemed to occur only in the polymers of higher  $\nu_e$ 's. For polymers of low  $\nu_e$ 's, the nano-plastic flows in the nanocomposite that contained multiwalled CNTs (MWCNTs) were restricted to the strain-softening regime due to the strong strain delocalization effect,<sup>19</sup> thus the polymer chains in the flows slipped around the bulky MWCNTs, rendering CNT reinforcements ineffective. For the soft single-walled CNTs (SWCNTs), although they fully participated with the polymer chains in the nano-plastic flows, chain entanglement clustering of the low- $\nu_e$  polymer chains made the SWCNTs behave as "phantom CNTs",<sup>20</sup> during the plastic flows, and thus produced no effect on the fibril drawing process.

Prior reinforcement attempts<sup>5,26</sup> for PBOs using non-treated CNTs produced only moderate enhancement for elastic performance while incurred virtually no effects in the plastic regime. In this study, the CNTs were surface-grafted with PBO chains and the nano-plastic interactions between the CNTs and the rigid-rod polymer matrix were systematically studied. The results reported here reveal this important knowledge and provide the essential information for further successful development of novel nanocomposites based on CNTs and aromatic rigid-rod polymers.

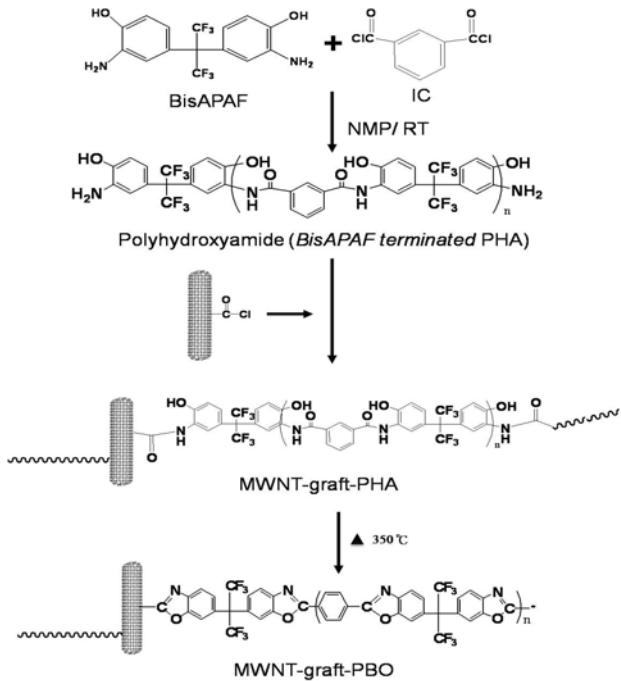
## Experimental Section

**Raw Materials.** The CNTs were purchased and used as received for subsequent surface functionalization. Their geometric dimensions were 10-35 nm (average outer diameter) and 10-30 $\mu\text{m}$  (length) for MWCNTs (DESUNNANO Co., Taiwan) and 1-1.5 nm (average outer diameter) and 10-20  $\mu\text{m}$  (average length) for SWCNTs (AETC Co., Taiwan), as determined by TEM. The monomers, reactants, and solvents, 2,2-bis(3amino-4-aminophenol)hexafluoropropane (BisAPAF), 4,6-diaminoresorcinal dihydrochloride (DAR), isophthaloyl chloride (IC), terephthaloyl chloride (TC), anhydrous N-methylpyrrolidone (NMP), 1-pyrenebutyric acid (pyrene-COOH), poly(phosphoric acid) (PPA) and  $\text{P}_2\text{O}_5$ , were obtained from Aldrich Chemicals and used without further purification.

**Synthesis of PBO.** The method by Kumar et al.<sup>5</sup> was modified and used here: 1,4-diaminoresorcinal dihydrochloride (DAR) (852.24 mg, 0.004 mol), terephthaloyl chloride (TC) (812.1 mg, 0.004 mol), and 2.494 g of phosphoric acid (85%) were poured into a glass flask equipped with a mechanical stirrer. The synthesis was carried out in the  $\text{N}_2$  atmosphere: the mixture was heated at 65°C for 16 h for de hydrochlorination followed by heating at 80°C for 4 h with the addition of the catalyst  $\text{P}_2\text{O}_5$  (1.608 g) and then kept at 80°C for another 2 h to form the poly(phosphoric terephthalic anhydride).<sup>3,7</sup> After 2 h, more  $\text{P}_2\text{O}_5$  (1.43 g) was added and the reactant content was 23wt %. The polymerization temperature was then slowly increased to 160°C for 16 h under steady stirring. The mixture was then heated to 19 0°C and stirred for an additional 4 days. Finally, the polymer was obtained by solution precipitation (S cheme 1), washing in deionized water, and drying under vacuum at 100°C for 24 h. The molecular weight of the PBO was determined to be  $M_v \approx 43\text{kg}/\text{mole}$  from the intrinsic viscosity of 61 dL/g measured in methane sulfonic acid at 30°C.



Scheme 1. Synthesis of PBO by polycondensation.

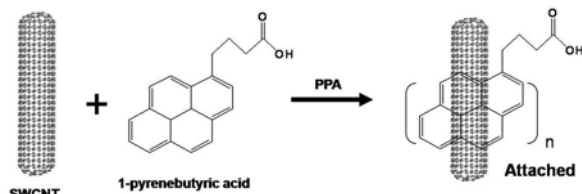


Scheme 2. Synthesis of MWCNT-g-PHA.

**CNTs Surface-Grafting.** For enhancing the matrix compatibility for uniform dispersion, the MWCNTs were surface grafted with PBO chains (MWNTs-g-PBO) by the two-step synthesis scheme in that PHA was first grafted on the MWNTs via a polycondensation reaction<sup>8</sup> and then subsequently converted into PBO by heating at 350°C for 4h. Before grafting, the MWCNTs were surface functionalized by first refluxing the as-received MWCNTs in concentrated nitric acid/sulfuric acid (3:1 in volume) at 50°C for 1.5h to anchor carboxylic acid groups onto the MWCNTs (MWCNTs-COOH).<sup>27</sup> Following the subsequent thorough washing with deionized water and complete drying, the MWCNTs-COOH were put in SOCl<sub>2</sub> and converted to MWCNT-COCl at 80°C for 2 h. The PHA grafting started with dissolving 2,2-bis(3amino-4-aminophenol) hexafluoropropane (BisAPAF) (377.58 mg, 1mmole), into anhydrous NMP (4 ml) with anhydrous pyridine (162.89 mg, 2mmole) in a dry 25ml glass flask under the N<sub>2</sub> environment. Then the solution was cooled to 5°C in an ice/water bath followed by slowly adding isophthaloyl chloride (IC) (203.12mg, 0.98mmole) and then kept stirring at 5°C for 2- 3 h. Then, still stirring, the temperature was returned slowly to room temperature for 16 h to form BisAPAF-terminated PHA. The surface-functionalized MWCNTs (MWCNT-COCl) were then added into the solution to react with BisAPAF-terminated PHA for 16 h, grafting the PHA on the MWCNTs (Scheme 2). The resulted viscous solution was washed in NMP by sonication and then vacuum-filtered through a 0.2μm PTFE membrane to remove the un-anchored PHA. The solid filtrate on the PTFE membrane (MWNTs-g-PHA) was then dried at 150°C for 3 h, followed by further annealing at 350°C to convert into MWNTs-g-PBO. The grafted PBO weight fraction on MWCNTs was determined from thermogravimetric analysis (TGA) to be approximately 55 wt%. For SWCNTs, a non-covalent grafting of pyrenes was used for improving the dispersion<sup>28</sup> by mixing the SWCNTs with an equal amount of 1-pyrenebutyric acid in PPA (0.5 mg/ml) stirred for 8 h at 120°C (Scheme 3).

**Preparation of Thin Film Samples.** The dry powder of functionalized MWCNTs was mixed with PBO in PPA at 160°C for 24 h to obtain the MWCNTs/PBO solution. For SWCNTs, PBO was blended into the PPA solution of SWCNTs and 1-pyrenebutyric acid to make the SWCNTs/PBO solution. Thin films of pristine semi-crystalline PBO polymer and the CNT-PBO nanocomposites were spun cast from their solutions onto clean glass plates. The film was floated off the substrate on distilled water and immersed in the water for 2 days to remove the PPA for which a FT-IR spectrometer was used to make certain the complete PPA removal. The film was then picked up by an

epoxy-coated copper grid and annealed at 120°C for 12h following an overnight drying in the ambient condition. The film thickness was controlled to be around 3 $\mu$ m. The fraction of CNTs ( $c_0$ ) in the films ranged from 0 to 10 wt%. Samples of pristine PBO were prepared by following the above procedures with  $c_0 = 0$ . These films were semi-crystalline. For the purpose of comparison, quasi-amorphous films of PBO were specially prepared by immersing the spin-coated film in H<sub>2</sub>SO<sub>4</sub>/ water (1:1 in volume) solution for 2 days for coagulation, and then rinsed in a water bath to remove any residual H<sub>2</sub>SO<sub>4</sub>.<sup>29</sup>



Scheme 3. Synthesis of Pyrene-SWCNTs.

**Nano-Mechanical Characterization.** The specimen was then mounted in a strain jig and stretched under an optical microscope to observe the growth of local deformation zones.<sup>12-17</sup> The stretched samples were further examined under an AFM (Veeco, Nanoscope IIIa) to obtain the topography (e.g., depth profiles) of the deformation zones.<sup>16-19,27</sup> The AFM topographic data were then used to calculate the local stress and strain distributions within the deformation zones. A transmission electron microscope (TEM, JOEL JEM-2010, 200 KeV.) and a field-emission scanning electron microscope (FE-SEM, JEOL JSM 6500) were also used to study the deformation zones. Wide-angle x-ray diffraction (WAXD) was performed to obtain information of the polymer crystalline structures in a Rigaku D-Max diffractometer (Cu-K $\alpha$ ) with a scanning speed of 2° min<sup>-1</sup>. Crystallinity of PBO from WAXD was determined using the software XPSPEAK 4.1 for peak fitting and integration.

## Results and Discussions

**Pristine PBO Films.** The pristine semi-crystalline PBO films revealed a morphology that contained broadly distributed second-phase crystallites of stick shapes with the dimensions of ~ 1-2  $\mu$ m in length, ~0.5-0.8 $\mu$ m in width, and ~0.3-0.5 $\mu$ m in height (Fig. 1b-c,d). In good agreement with the reported monoclinic unit cell (Figure 1g:  $a = 0.56$  nm for PBO molecules side to side packing,  $b = 0.35$  nm for PBO molecules face to face packing,  $c = 1.17$  nm,  $\alpha = \beta = 90^\circ$  and  $\gamma = 102.5^\circ$ )<sup>30</sup>, the WAXD patterns of the pristine PBO films (Figure 1g) illustrated four peaks at around  $2\theta = 15.8^\circ$ ( $d=0.56$ nm),  $18^\circ$ ( $d=0.49$ nm),  $22.6^\circ$ ( $d=0.40$ nm) and  $25.4^\circ$ ( $d=0.35$ nm), corresponding respectively to (100), (101), (003) and (010) lattice planes. This is also consistent with the selection area electron diffraction (SAED) results of these crystalline sticks within the broken crazes (Figure 2f). The WAXD pattern of the quasi-amorphous PBO films manifested no peaks (Figure 1f) and the film topography was much smoother than the regular PBO films (Figure 1e). Using the WAXD of the quasi-amorphous PBO films as the background, the crystallinity of the regular pristine PBO films was determined<sup>31</sup> to be around 33%.

Upon applying a strain ( $e$ ) to the sample, local deformation zones started to nucleate at  $e \sim 0.5\%$ . These deformation zones quickly underwent local break down at approximately  $e = 1.8\%$  (Figures 2a-c). These local deformation zones were crazes as they clearly illustrated fibrils that bridged between the two plates at the gaps, as shown in the micrographs of TEM and SEM (Figures 2d, e, and g).<sup>11-19,27</sup> The craze microstructure in the regular semi-crystalline PBO films was generally identical to that in the quasi-amorphous PBO films (Figures 2h and 2i). As revealed by SEM, these crazes typically underwent local break down as the craze width grew to around 1  $\mu$ m (Figures 2 e,f). These crazes were winding in the amorphous areas between the crystalline sticks and upon further deformation broke down at the edges of these second phase sticks that were generally too big to fit into the small fibrils (~5-10 nm in diameter) for micro-necking. This observation clearly indicated that the drawing stress of the nano-plastic flows was not strong enough to separate the tightly packed chains in the ordered phase. Yet, quite surprisingly, the amorphous PBO chains at a temperature about 600°C below their glass transition were so fibrillated into well-interconnected fibrils (Figures 2g-i). However, in this fully extended state, the chains within the fibrils were still amorphous, as unveiled by the SAED patterns on the fibrils (Figures 2g, inset). Due to the existence of broadly distributed

crystallites that could not be fibrillated, the craze widths ( $w$ ) and depth ( $d$ ) measured from the AFM topography of the semi-crystalline PBO films manifested large fluctuations such that the data scattered significantly in the plot of  $d$  versus  $w$ . The data fluctuation in the plot of  $d$  versus  $w$  decreased substantially in the quasi-amorphous films, however, clearly illustrating a micro-necking characteristic in that  $d$  increased linearly with  $w$  until a threshold above which  $d$  leveled (Figure 4a). Evidently, the plastic flow of the amorphous PBO chains followed a micro-necking process.

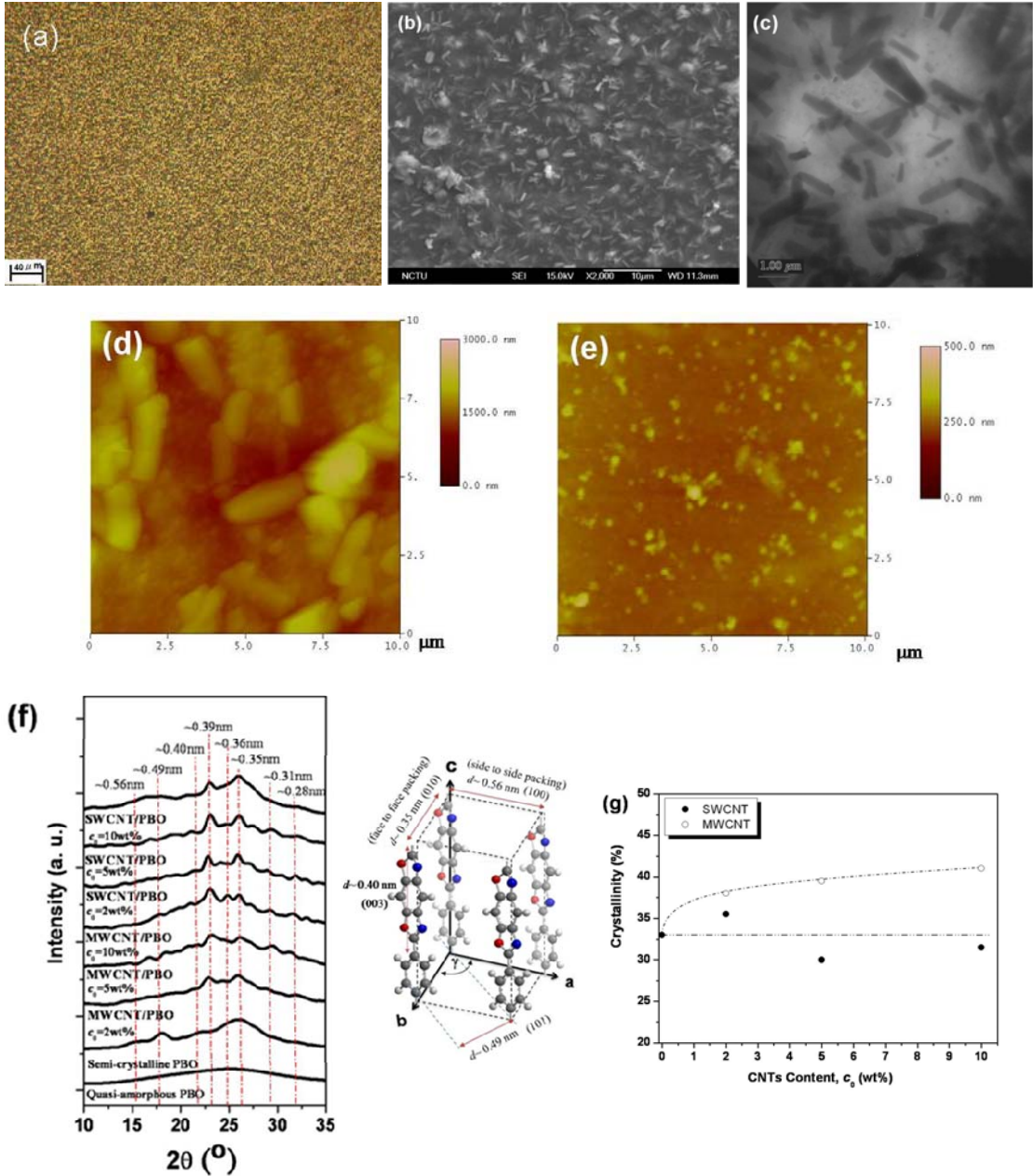


**Figure 1.** (a) Optical (b) SEM and (c) TEM micrographs of pristine semi-crystalline PBO films. AFM micrographs of (d) semi-crystalline and (e) the quasi-amorphous PBO films. (f) Wide angle X-ray diffraction patterns of PBO and CNTs/PBO films. g) The crystallinity of CNTs/PBO nanocomposites films versus CNTs content.

The craze extension ratio,  $\lambda_{\text{craze}}$ , was estimated from the AFM craze topography and the fibril packing density  $v_f(x)$  by  $\lambda_{\text{craze}} = 1 + \{2\ln [t_0/t(x)] - 2/3\ln[v_f(x)]\}$  where  $t_0$  is the original film thickness

and  $t(x)$  is the film thickness within the craze.<sup>16-17</sup> The value of  $v_f$  at the steady-state necking regime (i.e.  $w > w_c$ ) was taken to be a constant equal to 0.8 (corresponding to the closest packing of cylinders).<sup>16-17</sup> Therefore,  $\lambda_{\text{craze}}$  was calculated to be 4.3. The local drawing stress  $\tau$  within crazes in the films was determined from the AFM craze topography based on the Bridgeman necking plasticity.<sup>16-17</sup> At  $w > w_c$ , the value of  $\tau$  was about 3.3 GPa for pristine amorphous PBO films (Figure 4b).<sup>16-17</sup>

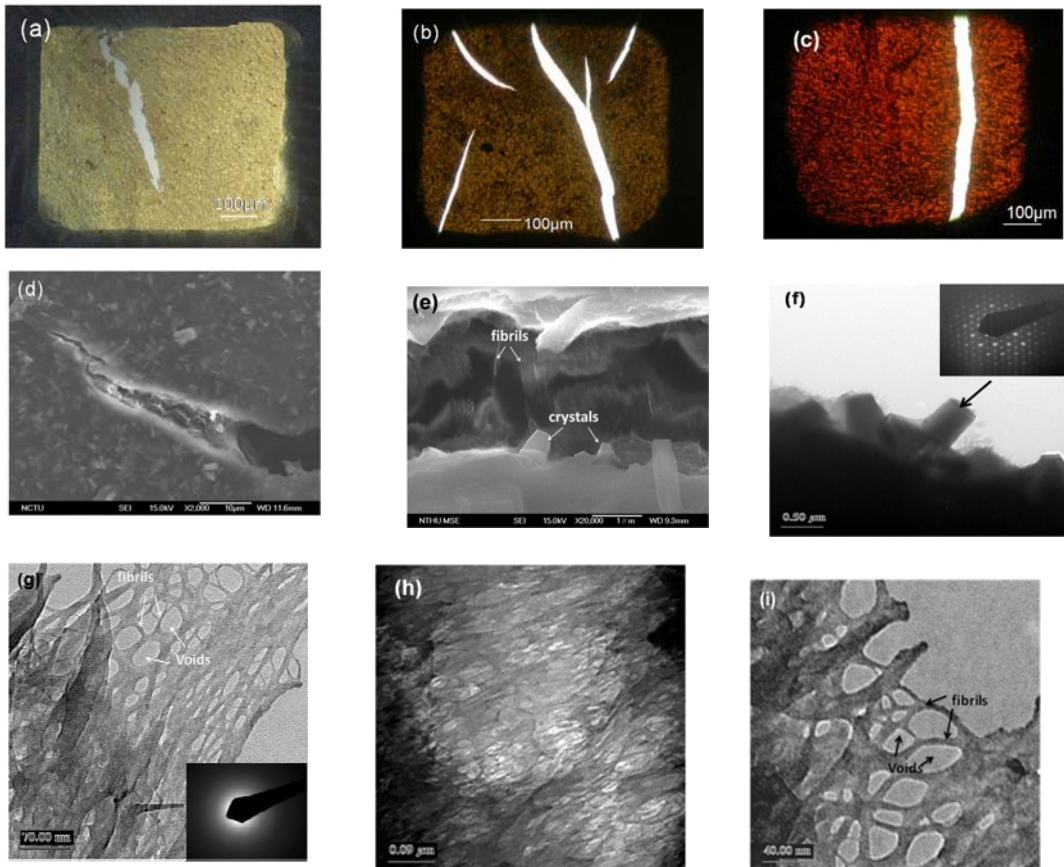


**Figure 2.** Optical micrograph of (a) pristine PBO,  $e = 3.0\%$  (b) MWCNT/PBO,  $c_0 = 2\text{wt}\%$ ,  $e = 2.5\%$ , (c) SWCNT/PBO,  $c_0 = 2\text{wt}\%$ ,  $e = 5.4\%$ ; SEM micrographs of pristine PBO films with craze (d-e); TEM micrographs of crazes in the pristine PBO films: (f) the broken edge within a craze, inset: the SAED pattern of the remaining PBO crystallite at the craze boundary; (g) broken craze fibrils, inset: SAED pattern of the craze fibrils, (h) crazes in the quasi-amorphous PBO films; (i) fibril breakdown in the quasi-amorphous PBO films.

**MWCNT/PBO Composite Films.** The PBO crystalline structure underwent extensive, but moderate, changes when the surface-grafted MWCNTs were blended into the rigid-rod chains. The high-angle peaks at  $2\theta = 22.6^\circ$  and  $25.4^\circ$ , corresponding to  $d$ -spacing = 0.39 nm and 0.36 nm, rose in intensity as the fraction of MWCNTs ( $c_0$ ) increased. At the same time, the low-angle peaks at  $2\theta = 15.8^\circ$  and  $18^\circ$  decreased in intensity. Besides, four new diffraction peaks emerged at  $2\theta = 22.6^\circ$ ,  $24.9^\circ$ ,  $29.0^\circ$  and  $32.0^\circ$  ( $d$ = 0.39, 0.36, 0.31 and 0.28 nm respectively) in the nanocomposite films, in addition to the reflection corresponding to the interlayer spacing of MWCNTs  $20\sim26.0^\circ$  ( $d$ -spacing = 0.34 nm)<sup>32</sup> which overlapped the (010) lattice plane of the semi-crystalline PBO (Figure 1f). The structural modifications of the crystallites were consistent with the revelations by other works<sup>31,33,34</sup> that carbon nanotubes served not only as nucleation sites but also templates for chain crystallization. The newly introduced interactions represented the local engagements, likely via the  $\pi-\pi$  interactions, between the matrix PBO segments, the grafted PBO chains, and the surfaces of MWCNTs that reduced the free energy of the system. The free energy reduction ( $\Delta G$ ) effectively provided new

bonding between the CNTs and the PBO chains.

The crystallinity in the MWCNTs/PBO films, determined from the WAXD curves corrected with  $c_0$ , increased slightly with  $c_0$  from 33% at  $c_0 = 0$ , and 38% for  $c_0 = 2$  wt%, to 41% for  $c_0 = 10$  wt % (Figure 1g).

The MWCNTs/PBO films underwent nanoplastic flows to grow crazes when stretched, but the number of crazes increased significantly as compared to the neat PBO resin (Figure 2 a,b). Clearly, this was due to the strain delocalization effect that was also present in other CNT/polymer systems.<sup>18,20</sup> Closer inspections under a SEM revealed a “blunted” stress concentration ahead of the craze propagation in that multiple crazes were nucleated in the vicinity of a major craze (Figure 3e). This is a noteworthy departure from results in neat PBO films where only one craze dominated the fracturing process (Figure 2d). Furthermore, extensive “pull-out” of the MWCNTs was observed in the broken crazes (Figure 3f), which in theory would contribute to the increase of fracture toughness. However, the pile-up of MWCNT at craze boundaries that prevailed in the PS/MWCNTs systems<sup>18,19</sup> was not observed here, evidently due to the fact that all the crazes in the PBO/MWCNTs films had been too narrow (< 1 micron in width) for this to be documented.

**SWCNT/PBO Composite Films.** Similar changes in crystalline structures to those in MWCNT/PBO films, as revealed by the WAXD patterns (Figure 1g), were observed when SWCNTs were introduced into the PBO matrix. The peaks at  $2\theta = 22.6^\circ$  and  $25.4^\circ$  increased in intensity, along with the emergence of the four new peaks at  $2\theta = 22.6^\circ$ ,  $24.9^\circ$ ,  $29^\circ$  and  $32^\circ$  ( $d = 0.39$ ,  $0.36$ ,  $0.31$  and  $0.28$  nm respectively). Owing to bundling of the SWCNTs, the interlayer spacing of CNTs  $20\text{--}26^\circ$  ( $d$ -spacing = 0.34 nm)<sup>32</sup> still appeared in the WAXD pattern. To the same degree, these changes in the crystalline structure revealed the new interactions (likely the  $\pi$ - $\pi$  interactions between aromatic groups) introduced between the SWCNTs and the matrix PBO segments. For SWCNT/PBO films, however, the crystallinity of PBO remained almost constant in a narrow range between 30 and 35 % for all  $c_0$ 's from 2 to 10 wt% (Figure 1g) as estimated from the WAXD results.

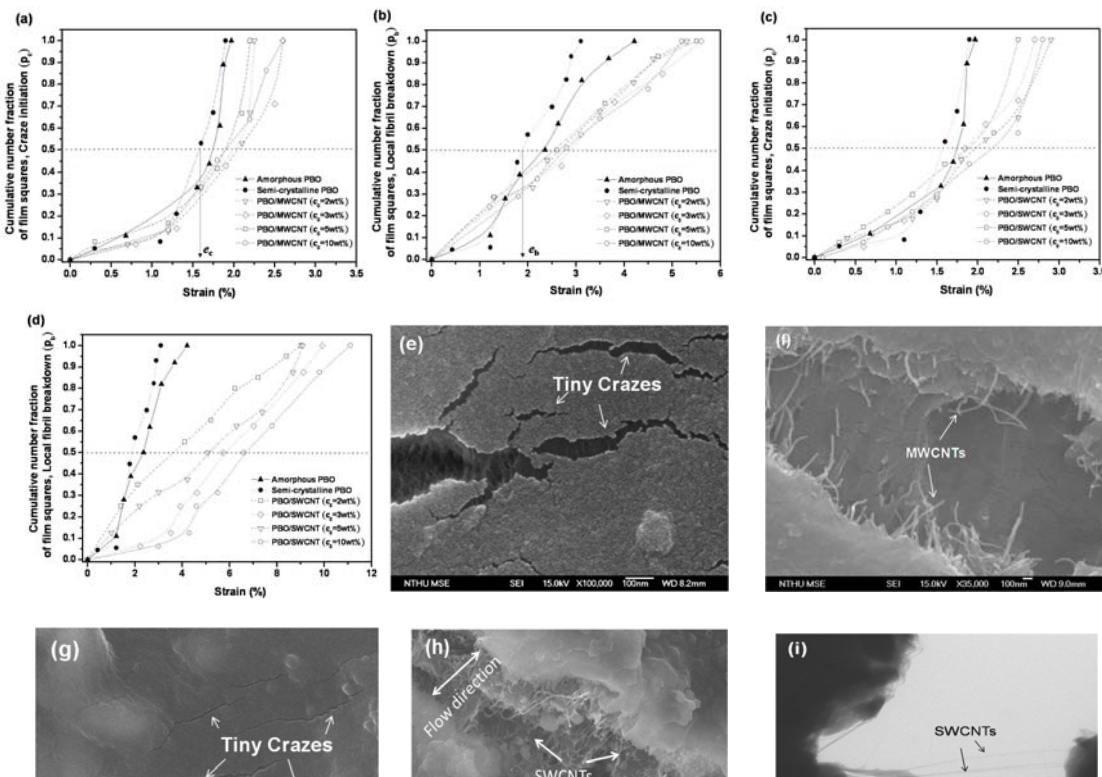


**Figure 3.** Cumulative number fraction of film squares that have craze initiation ( $p_c$ ) and craze fibril breakdown ( $p_b$ ) versus tensile strain in CNT/PBO films (a,b) MWCNT and (c,d) SWCNT. SEM micrographs of (e,f,g) MWCNT/PBO film (c<sub>0</sub>=2wt%), (c,d) SWCNT/PBO film (c<sub>0</sub>=2wt%), (i) TEM mi-

crographs of crazes in the SWCNTs/PBO films ( $c_0=2\text{wt\%}$ ).

The craze morphology changed significantly as the SWCNTs were dispersed in the PBO matrix. The crazes became notably shorter and narrower (Figure 3g). The fracture strain increases to  $e \sim 4.5\%$  for  $c_0 = 2\text{wt\%}$  (Figure 2c). A strain delocalization effect was also observed in that a multitude of tiny crazes preceding the advance of the dominant craze were noticed (Figure 3g). Similar to the craze breakdown in the MWCNTs/PBO systems, extensive CNT pull-out (Figure 3h) was observed in the SWCNTs reinforced systems. In fact, SWCNTs were drawing into the crazes (Figure 3i), similar to the loose entanglement system of SWCNTs/PS films,<sup>20</sup> and may contribute to the increase of craze fibril stability.

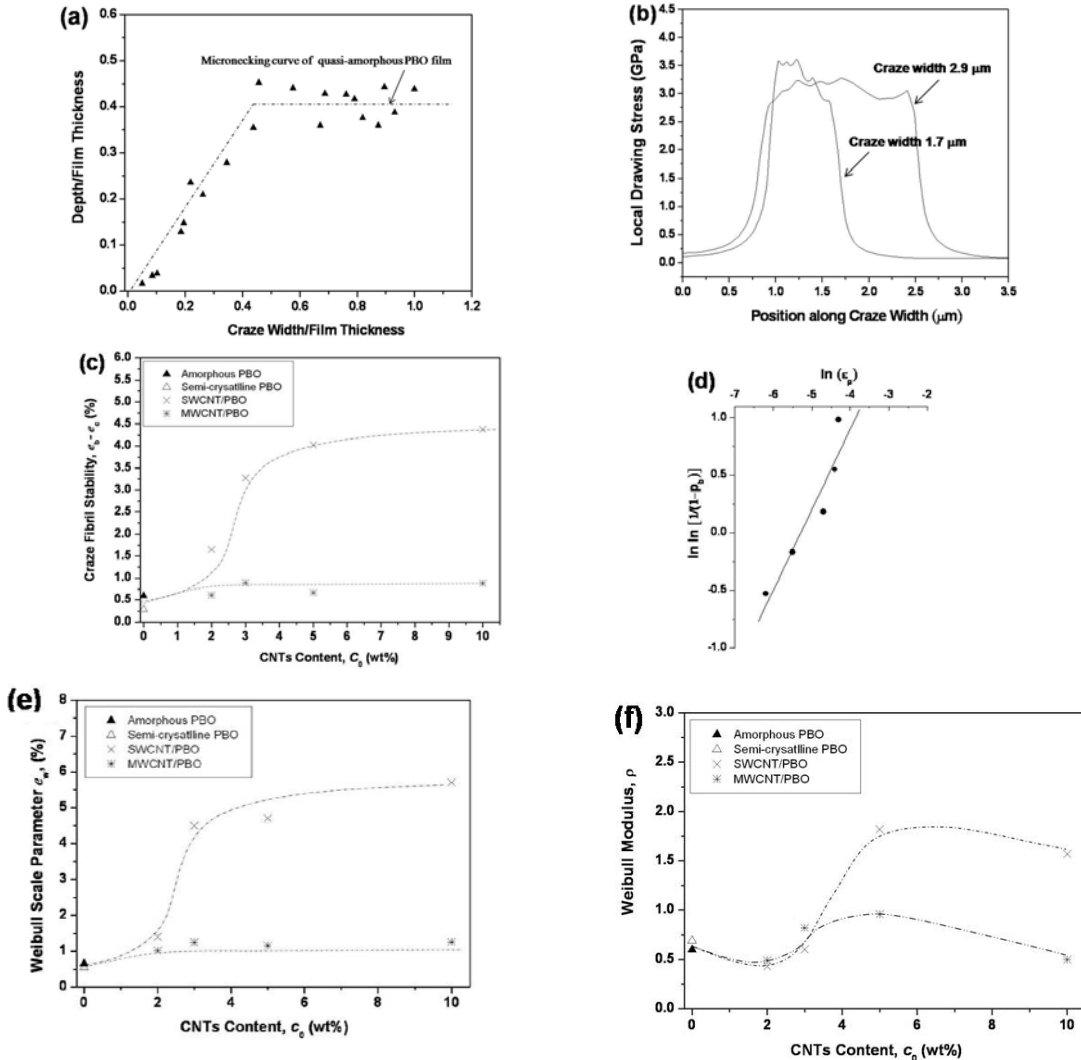


**Figure 4.** Plot of (a) craze depth ( $d$ ) versus craze width ( $w$ ) for PBO and CNTs/PBO films, (b) local stress distribution within a craze across the craze width for quasi-amorphous PBO film, (c) fibril stability ( $e_b - e_c$ ) vs.  $c_0$  for CNTs/PBO films. (d) Typical Weibull plot for craze fibril breakdown in semi-crystalline PBO film ( $\varepsilon_p \equiv e - e_c$ ). (e) The Weibull scale parameter  $e_w$  vs.  $c_0$ . (f) The Weibull modulus  $\rho$  vs.  $c_0$ .

**Weibull Analysis.** The reinforcement effect arising from interactions of CNTs with the nano-plastic flows was evaluated by following the method by E. J. Kramer on brittle PS films.<sup>11,12</sup> The treatment was detailed elsewhere,<sup>12</sup> thus it is only briefly described here. The polymer film was supported by the copper grids and effectively sub-divided into many independent film squares, allowing the cumulativ

e number fractions of film squares, that had undergone craze initiation ( $p_c$ ) and fibril breakdown ( $p_b$ ), to be recorded as function of applied strain ( $e$ ) (Figs. 3a and 3b). The median strains ( $e_c$  and  $e_b$ ), corresponding to the statistical medians respectively for craze initiation ( $p_c = 0.5$ ) and local craze breakdown ( $p_b = 0.5$ ) were determined, and the data of  $p_c(e)$  and  $p_b(e)$  were analyzed by the Weibull statistics. The plastic strain limit in which the craze fibril maintained mechanical stability ( $e_b - e_c$ ) was defined as the craze fibril stability.<sup>12</sup>

It was found that the crystallinity of PBO produced negligible effects on the crazing strain  $e_c$  and the breakdown strain  $e_b$  as the curves of  $p_c$ , or  $p_b$ , for the semicrystalline PBO and the quasi-amorphous PBO were very similar to each other. Upon the introduction of MWCNTs, the median strain of craze initiation increased from  $e_c \sim 1.6\%$  (for neat PBO) to  $e_c \sim 2.0\%$  while the breakdown strain  $e_b$  increased from  $\sim 1.9\%$  to  $\sim 2.8\%$ , with both  $e_c$  and  $e_b$  largely independent of  $c_0$  for all  $c_0$ 's from 2 to 10 wt%. The result clearly indicates that the MWCNT-polymer interactions had produced no significant effects in this  $c_0$  range on the LOCAL elastic properties that dictated the onset of crazing. Furthermore, the increase of  $e_b$ , or craze fibril stability ( $e_b - e_c$ ),<sup>12</sup> was small, illustrating that during the nano-plastic flows the CNT-polymer interactions had produced only modest influences on the fibril drawing behavior considering that MWCNT pull-out (Figure 3f) had contributed to increased mechanical stability during the failure process of crazes.

For the SWCNTs/PBO films, in contrast, although the increase of the median strain for craze initiation  $e_c$  was small, from  $e_c \sim 1.6\%$  (for pristine semi-crystalline PBO) to about  $e_c \sim 2.2\%$ , which was also approximately independent of  $c_0$  (Figure 3c), the median strain for fibril breakdown  $e_b$  increased steadily with  $c_0$ , from  $e_b \sim 1.9\%$  (for neat PBO) to  $\sim 6.7\%$  for  $c_0 = 10\text{ wt\%}$  (Figure 3d). Correspondingly, the craze fibril stability increased significantly from 0.29% (for  $c_0 = 0$ ) to 4.25% (for  $c_0 = 10\text{ wt\%}$ ), an increase of over 10 fold (Figure 4c). This strongly indicates that the interactions of SWCNTs and the plastically flowed polymer chains significantly enhanced the mechanical stability during fibril drawing. This type of interaction was not observed in that between the MWCNTs and the glassy polymer chains.

The fibril breakdown statistics  $p_b(e)$  was then analyzed with the Weibull model,  $p_b(e) = 1 - \exp\{- (V_0/V_b)[(e - e_c)/e_w]^\rho\}$ , and the Weibull scale parameter  $e_w$  (an alternative measure for craze fibril stability) and the Weibull modulus  $\rho$  (a parameter for the breadth of failure distribution) was determined from the Weibull plot of  $\ln\ln[1/(1 - p_b)]$  versus  $\ln(e - e_c)$  (Figure 4d).<sup>12,35</sup> The volume parameters  $V_0$  and  $V_b$  are, respectively, the sample volume and the characteristic volume of which a single event of fibril breakdown may take place. As affirmation to the previous results, the Weibull scale parameter  $e_w$  of the SWCNTs/PBO films increased from  $e_w \sim 0.54\%$  (pristine PBO) to  $e_w \sim 5.7\%$  for SWCNT/PBO ( $c_0 = 10\text{ wt\%}$ ), consistent with the  $\sim 10$  fold increase in craze fibril stability (Figure 4e). In contrast,  $e_w$  varied negligibly with  $c_0$  in the MWCNTs/PBO films, increasing slightly from  $\sim 0.54\%$  (pristine PBO) to about  $\sim 1\%$  for  $c_0 > 1\%$  (Figure 4e). The Weibull modulus  $\rho$ , on the other hand, lay between 0.5 and 1 for the MWCNTs/PBO films while in the SWCNTs/PBO films increased significantly to  $\sim 1.75$  for  $c_0 > 3\text{wt\%}$  (Figure 4f). The increase in  $\rho$  seems to indicate that the SWCNTs-chains interactions,  $\Delta G$ , that had enhanced craze fibril stability broke down in the high strain regime within a narrower strain range, as a higher  $\rho$  indicates a narrower distribution.

**Interaction between PBO Crystals and Nano-plastic Flows.** It is quite intriguing that the glassy rigid-rod PBO chains were drawn up to a molecular strain around 330% into craze fibrils even at a temperature about 600°C below the glass transition. It appears that the “loose” entanglements of the rigid-rod PBO chains had provided the condition for coordinated chain clustering upon stretching, for crazing to take place.<sup>20</sup> The low craze fibril stability, on the other hand, could well have been due to the intrinsically short chain lengths of the PBO macromolecules.

In the SWCNTs/PBO systems, engagements via the  $\pi-\pi$  interactions between the PBO chains and the SWCNTs ( $\Delta G$ ) created quasi-crosslinks between the polymer chains. Hence, the craze fibril stability increased substantially. This crosslink effect, however, only became operative when the CNTs participated in the nano-plastic process, which is the case for SWCNTs, such that the effect of the greater effective molecular weights of the flowing polymer chains was manifested. In contrast, when the CNTs were too rigid to participate in the nano-plastic flows, such as the cases of MWCNTs,<sup>21</sup> the PBO chains only drained through the MWCNTs and the quasi-crosslinking effect due to  $\Delta G$  was rendered inoperative.

In further detail, the chain unfolding force of the PBO crystallites  $f_{unfold}$  can be calculated from  $f_{unfold} = -U/S$  where  $U$  is the minimum chain packing energy of the PBO crystals ( $U = -5.7$  Kcal/mole) and  $S$  is the critical chain displacement for cleaving the crystal.<sup>30,36</sup>  $S$  can be further related to the elastic limit ( $e_e$ ) of the crystals and the packing chain spacing ( $l$ ) within-in by  $S = l \bullet e_e$  and was calculated to be 6.8 nN ( $e_e \sim 1\%$  and  $l = 0.56$  nm).<sup>30,36</sup> On the other hand, the fibrillation stress  $f$  exerting on a single PBO crystal along the direction of the weakest strength during nano-plastic flows can be estimated from  $f = \tau A_{crystal}$  where  $\tau$  is craze drawing stress<sup>19,20</sup> and  $A_{crystal}$  is the cross-section area of the crystal unit cell in the weakest strength direction (along the  $a$  axis). Since  $\tau$  was determined<sup>16,17,19,20</sup> to be 3.3 GPa from the AFM craze topography and  $A_{crystal}$  was previously obtained to be around 0.41 nm<sup>2,36,37</sup> the fibrillation stress  $f$  was calculated to be  $f = 1.36$  nN, significantly smaller than  $f_{unfold}$ . This result is consistent with the fact that the tightly packed chains in the order phase are difficult to be fibrillated during the nano-plastic process.

## Conclusions

The wholly aromatic rigid-rod PBO polymers underwent large plastic deformation to a draw ratio around 4.3 in the form of crazes when stretched in ambient conditions. The nano-plastic flows took place by drawing the amorphous chains following micro-necking mechanics in which the shearing stress was determined to be around 3 GPa from AFM topography and necking plasticity. The drawing stress, however, had not been large enough to fibrillate crystalline chain segments, leaving the crazes restricted in width and winding between crystallites. The nano-plastic flows were soon superseded by fibril breakdown, manifesting low extensibilities below 2%. The craze fibril stability was found to remain constant in the films where virtually all crystallites were removed, indicating that the crystallites were not sources of weakness. In an attempt to reinforce the mechanical stability through intervene of the nano-plastic flows, surface-grafted CNTs were added into the rigid-rod polymers. It was found that new interactions between the CNTs and the ordered PBO chains emerged that extensively alter the crystalline structures. The CNTs-chains interactions were found to have a strong reinforcement effect in the SWCNTs/PBO samples where the craze fibril stability increased dramatically. This reinforcement was attributed to the chain-coupling effect provided by the SWCNTs during the nano-plastic flows. On the other hand, the bulky MWCNTs which did not participate in the chain flowing processes produced no effects.

## Acknowledgments

We thank the financial supports by both the National Science Council of Taiwan and the US Air Force Office of Scientific Research through the Taiwan-US Air Force Nanoscience Initiative Program (AOARD-084125, -094024).

## References

- (1) Zhang, H.; Farris, R. J.; Westmoreland, P. R. *Macromolecules* **2003**, 36, 3944.
- (2) Chae, H. G.; Kumar, S. *J. Appl. Polym. Sci.* **2006**, 100, 791.
- (3) Choe, E. W.; Kim, S. N. *Macromolecules* **1981**, 14, 920.
- (4) Huang, J. W.; Bai, S. J. *Nanotechnology* **2005**, 16, 1406.
- (5) Kumar, S.; Dang, T. D.; Arnold, F. E.; Bhattacharyya, A. R.; Min, B. G. Zhang, X.; Vaia, R. A.; Park, C.; Adams, W. W.; Hauge, R. H.; Smalley, R. E.; Ramesh, S.; Willis, P. A. *Macromolecules* **2002**, 35, 9039.
- (6) Cotts, D. B.; Berry, G. C. *Macromolecules* **1981**, 14, 930.
- (7) So, Y. H.; Heeschen, J. P. *J. Org. Chem.* **1997**, 62, 3552.
- (8) Hsu, S. L. C.; Chang, K. C.; *Polymer* **2002**, 43, 4097.
- (9) So, Y. H.; Heeschen, J. P.; Bell, B.; Bonk, P.; Briggs, M.; Decaire, R. *Macromolecules* **1998**, 31, 5229.
- (10) So, Y. H. *J. Polym. Sci. Polym. Chem.* **1994**, 32, 1899.
- (11) Kramer, E. J. *Adv. Polym. Sci.* **1983**, 52/53, 1.
- (12) Yang, A. C. M.; Kramer, E. J.; Kuo, C. C.; Phoenix, S. L. *Macromolecules* **1986**, 19, 2010.
- (13) Yang, A. C. M.; Kramer, E. J.; Kuo, C. C.; Phoenix, S. L. *Macromolecules* **1986**, 19, 2020.
- (14) Yang, A. C. M.; Kunz, M. S.; Logan, J. A. *Macromolecules* **1993**, 26, 1776.
- (15) Yang, A. C. M.; Wang, R. C.; Lin, J. H.; *Polymer* **1996**, 37, 5751.

- (16) Lin, J. H.; Yang, A. C. M. *Macromolecules* **2001**, 34, 3698.
- (17) Lin, C. H.; Yang, A. C. M. *Macromolecules* **2001**, 34, 4865.
- (18) Hsiao, C. C.; Lin, T. S.; Cheng, L. Y.; Ma, C. C. M.; Yang, A. C. M. *Macromolecules* **2005**, 38, 4811.
- (19) Lin, C. W.; Huang, L. C.; Ma, C. C. M.; Yang, A. C. M.; Lin, C. J.; Lin, L. J. *Macromolecules* **2008**, 41, 4978.
- (20) Lin, C. W. ; Yang, A. C. M. *Macromolecules* **2010**, in press.
- (21) Coleman, J. N.; Cadek, M.; Blake, R.; Nicolosi, V.; Ryan, K. P.; Belton, C.; Fonseca, A .; Nagy, J. B.; Gun'ko, Y. K.; Blau, W.J. *Adv. Funct. Mater.* **2004**, 14, 791.
- (22) Blond, D; Barron, V.; Ruether, M.; Ryan, K. P.; Nicolosi, V.; Blau, W. J.; Coleman, J. N. *Adv. Funct. Mater.* **2006**, 16, 1608.
- (23) Hwang, G. L. ; Shieh, Y. T.; Hwang, K. C. *Adv. Funct. Mater.* **2004**, 14, 487.
- (24) Coleman, J. N.; Khan, U.; Gun'ko, Y. K. *Adv. Mater.* **2006**, 18, 689.
- (25) Schadler, L. S.; Giannaris, S. C.; Ajayan, P. M. *Appl. Phys. Lett.* **1998**, 73, 3842.
- (26) Zhou, C. G.; Wang, S. F.; Zhuang, Q.; Han, Z. W. *Carbon* **2008**, 46, 1232.
- (27) Lin, T. S.; Cheng, L. Y.; Hsiao, C. C.; Yang, A. C. M. *Mater. Chem. Phys.* **2005**, 94, 438.
- (28) Chen, R. J.; Zhang, Y.; Wang, D.; Dai, H. *J. Am. Chem. Soc.* **2001**, 123, 3838
- (29) Nelson, D. S.; Soane, D. S. *Polym. Eng. Sci.* **1994**, 34, 965.
- (30) Martin, D. C., Thomas, E. L. *Macromolecules* **1991**, 24, 2450.
- (31) Minus, M. L.; Chae, H. G.; Kumar, S. *Polymer* **2006**, 47, 3705.
- (32) Liu, G.; Zhao, Y.; Deng, K.; Liu, Z.; Chu, W.; Chen, J.; Yang, Y.; Zheng, K.; Huang, H.; Ma, W.; Song, L.; Yang, H.; Gu, C.; Rao, G.; Wang, C.; Xie, S.; Sun, L. *Nano Lett.* **2008**, 8, 1071.
- (33) Bhattachryya, A. B.; Sreekumar, T. V.; Liu, T.; Kumar, S.; Ericson, L. M.; Hauge, R. H.; Smalley, R. E. *Polymer* **2003**, 44, 2373.
- (34) Shieh, Y. T.; Liu, G. L.; Hwang, K. C.; Chen, C. C.; *Polymer* **2005**, 46, 10945.
- (35) Weibull, W. *J. App. Mech.* **1951**, 18, 293.
- (36) Bhaumik, D.; Welsh, W. J.; Jaffe, H. H.; Mark, J. E. *Macromolecules* **1981**, 14, 951.
- (37) Tashiro, K.; Kobayashi, M. *Macromolecules* **1991**, 24, 3706.

## SECTION 8

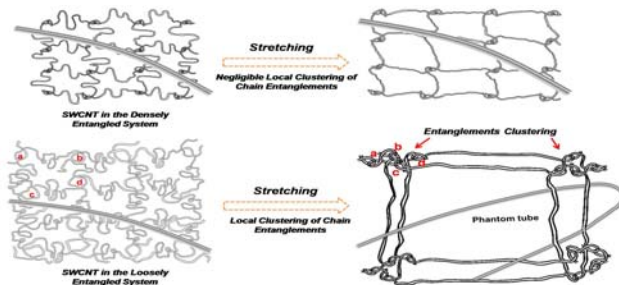
### Nano-Plastic Interactions of Surface-Grafted Single-Walled Carbon Nanotubes with Glassy Polymer Chains in Nanocomposites

Chih-Wei Lin and Arnold C.-M. Yang\*

Department of Materials Science and Engineering, National Tsing Hua University, Hsinchu, Taiwan

#### Abstract

The nanoscopic interactions between glassy macromolecules and the dispersed single-walled carbon nanotubes (SWCNTs) in a nanocomposite during very large local elongations were revealed. The results also unveiled a unique mode of molecular motions followed by glassy chains during brittle nano-plastic flows. Based on detailed nanomechanical calculations on results from atomic force and electron microscopy, the molecular motions of the “strain-softened” glassy polymer chains were found highly dependent on chain entanglement density ( $\nu_e$ ), in sharp contrast to the  $\nu_e$ -independent elastic reinforcement. Particularly, in the loosely entangled chains the SWCNTs behaved like “phantom tubes”, manifesting no effects on strain-hardening of the chain network during plastic flow. This indicates that the “glassy” chains had undergone entanglement clustering, a new and unique mode of non-affine molecular motions. The results bear important significance in revealing the fundamental behavior of glassy polymer chains and the reinforcement by SWCNTs.



#### Introduction

Glassy polymers, when exerted by large stresses, manifest plastic flows after passing through the brief elastic deformation regime.<sup>1-14</sup> As a result, local plastic deformation zones of crazes or shear deformation zones (SDZs) emerge by neck-drawing the stress-softened polymer, subsequently triggering respectively the brittle or ductile fractures. These local deformation mechanisms (crazing and local shear deformations) represent plastic flows of glassy chains that occur in nanoscopic scales, and therefore can be termed as nanoplastic flows to reveal the underlying nature of their formation. These deformation zones, once developed, behave as strain sinks and absorb the subsequent strains applied to the material, leaving the remaining regions in the primordial elastic state.

In details, the local deformation zones are formed via micro-necking processes by drawing polymer chains from the bulk, strain-softened and extended to a fixed draw ratio ( $\lambda_{\text{craze}}$ ) defined by the strain-hardened state of the entangled chain meshes.<sup>1-11</sup> It is well-established that the chain entanglement density ( $\nu_e$ ) determines whether crazes or SDZs occurs during the nanoplastic flows. For low  $\nu_e$  polymers, such as polystyrene (PS) ( $\nu_{e,PS} = 3.3 \times 10^{25} \text{ m}^{-3}$ ), fibrils (of around 10 nm in diameter) develop during the neck-drawing to form crazes.<sup>1-14</sup> On the other hand, polymers of high  $\nu_e$ , such as polyphenylene oxide (PPO) ( $\nu_{e,PPO} = 1.5 \times 10^{26} \text{ m}^{-3}$ ) grow the relatively featureless SDZs that are resulted from uniform thinning of the sample.<sup>4-6,22-24</sup> A high resolution microscope, such as transmission electron microscope (TEM) or atomic force microscope (AFM), is usually required to

discern if a fibril structure exists in the local deformation zones (The TEM micrographs of typical crazes and SDZs can be found in Figure 1 in reference 18.). Despite the extensive studies of using TEM, AFM, SAXS, and other tools that had clearly revealed the microstructure and micromechanics of these deformation zones,<sup>1-11</sup> the dynamic molecular mechanisms for strain softening remained largely illusive.

Carbon nanotubes (CNTs), owing to their superb mechanical reinforcement and outstanding electrical and thermal properties, are highly attractive as filler candidates for novel polymeric nanocomposites.<sup>17,26-30</sup> At the core of the endeavor are attempts of using them to intervene the dynamics of chain motions to achieve control over the mechanical behavior. With such, PS-grafted multi-walled CNTs (MWCNTs) had been prepared and dispersed into PS or PPO to investigate the nanoplastic flow interactions.<sup>16-18</sup> It was found that the loosely entangled PS chains tended to slip around the bulky MWCNTs (diameter ~30 nm) during nanoplastic flows, leaving the MWCNTs excluded from fibrillation and piled up at the craze boundaries. In contrast, the tightly entangled PPO chains engage effectively with the MWCNTs to draw the CNTs into the SDZs.<sup>18</sup>

To further reveal the molecular motions, PS-grafted single-walled CNTs (SWCNTs) were prepared and used to study the micromechanics and nanoscopic interactions, as reported here. SWCNTs are very thin (~1.0 -1.5 nm in diameter), quite comparable to the diameter of the confining tube of a single chain ( $D_{\text{chain}} = 0.94 \text{ nm}$  for PS). They are very soft, making them ideal for probing the characteristic behavior of polymer chains. New important insight was obtained in light of the strain softening of entangled glassy chains as well as the reinforcement effect by SWCNT in the nanocomposites.

## Experimental section

Monodisperse PS ( $M_w = 2000 \text{ kg/mol}$ ; Pressure Chemical, USA) and PPO ( $M_w = 244 \text{ kg/mol}$ ; Aldrich, USA) were used as received. The SWCNTs (AETC Co., Taiwan) were purified to > 95%, with average outer diameter of ca. 1–1.5 nm and average length of 10–20  $\mu\text{m}$ . The methods of preparing the PS-grafted CNTs and their polymeric nanocomposites thin films, as well as the mechanical characterization, were reported elsewhere<sup>1,5,7,9,16-18</sup> and will not be elaborated here. The molecular weight of the grafted PS was ca. 38 kg/mol (polydispersity = 2.2), determined from gel permeation chromatography of the PS chains that were cleaved from grafted CNTs.<sup>21</sup> The weight fraction of the grafted PS in the PS-g-SWCNTs was determined by using thermogravimetric analysis (TGA) to be around 61 wt%. The average length of the PS-g-SWCNTs was ca. 2–5  $\mu\text{m}$ . The surfaces of the SWCNTs, as revealed by transmission electron microscopy (TEM) (Figure 1a), were covered with a thin layer of PS chains. The SWCNTs used in this study often bundled even after surface modification, due to the large van der Waals forces, with a diameter ranging from 2 to 5 nm.

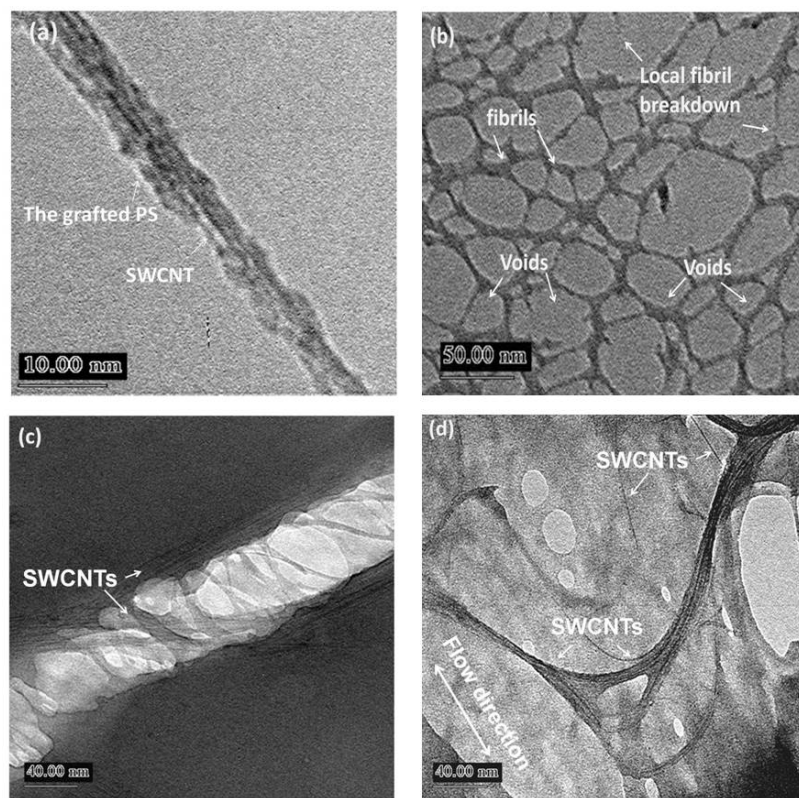


**Figure 1.** TEM micrographs of (a) SWCNT-grafted PS, (b) a craze microstructure, (c) a craze tip in SWCNT/PS films ( $c_0 = 15$  wt%), and (d) wider crazes in SWCNT/PS films ( $c_0 = 15$  wt%).

To fabricate free-standing films of the nanocomposite for mechanical characterization,<sup>1-13,16,18</sup> toluene solutions of one the polymer (neat PS, neat PPO, or a PS and PPO blend) and the PS-g-SWCNTs were prepared for spin-casting thin polymer films with thickness ( $t_0$ ) around 0.5  $\mu\text{m}$ . The films were then floated onto a water surface followed by being picked up on a piece of copper grids for subsequent mechanical stretching. Details of the sample preparations were elaborated elsewhere.<sup>1-13,16,18</sup> The weight fraction ( $c_0$ ) of the SWCNTs in the composite films ranged from 0 to 15 wt%. Prior to the mechanical testing, the SWCNTs/PPO, PPO-PS, and SWCNT/PPO-PS blend films were aged at 120 °C for 1 h to enhance the strain localization required for the growth of SDZs.<sup>12,13</sup>

For the mechanical test, the nanocomposite film was stretched using a strain jig and observed under an optical microscope. The applied strain rate was controlled approximately at  $2 \times 10^{-4} \text{ s}^{-1}$ . To characterize the microstructure of the deformation zones, the stretched samples were examined using an atomic force microscope (Veeco Instruments, Nanoscope IIIa) and a transmission electron microscope (JOEL JEM-2010; acceleration voltage: 200 kV).<sup>1-8,16-18</sup> The AFM topographic data were used to calculate the local stress and strain information in the DZs.<sup>1-8,16-18</sup> The widening velocities of the SDZs and crazes were obtained from images of the growing microdeformation zones, recorded using a video camera attached to an optical microscope.<sup>18</sup>

## Results and Discussions

**Loosely Entangled Chain Systems.** Crazes were initiated at ca. 1% strain ( $\varepsilon$ ) in neat PS; they were generally long and straight. AFM topography revealed that the craze depth ( $d$ ) increased linearly with respect to the craze width ( $w$ ) until the width reached a critical value,  $w_c$  (for 0.5- $\mu\text{m}$ -thick PS,  $w_c = \text{ca. } 2.5 \mu\text{m}$ ), above which  $d$  leveled and the craze necking had become mature (Figure 2a).<sup>7,8,16-18</sup> The leveling depth ( $d_s$ ) is directly related to the fibril draw ratio ( $\lambda_{\text{craze}}$ ) in the craze.<sup>2-5,9-11</sup> The maximum width of the crazes reaches ca. 20  $\mu\text{m}$ . Local fibril breakdown in the neat PS films occurred as the strain increased to ca. 8%, which ultimately led to fractures of the polymer films.<sup>5</sup> Figure 1b shows a TEM micrograph of a relaxed structure of the craze fibrils in the vicinity of a local breakdown site in a pristine PS film, which clearly reveals that the structure contained interconnected fibrils and voids. The average distance between the fibril nodes where fibrils locally joined together was around 40 nm.

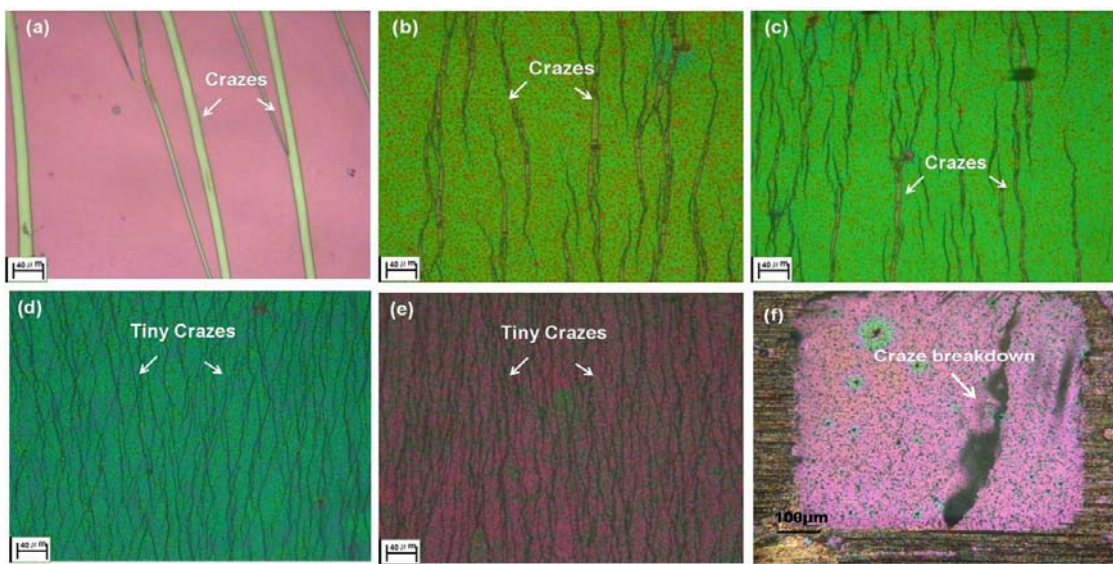


**Figure 2.** Optical micrographs of stretched (a) pristine PS films and (b–f) SWCNT/PS composite films having values of  $c_0$  of (b) 2 wt%, (c) 5 wt%, (d) 7 wt%, (e) 15 wt%, and (f) 20 wt%.

As SWCNTs were added into the neat PS, the craze morphologies of the SWCNT/PS ( $c_0 = 2\text{--}15$  wt%) changed dramatically. Generally, these crazes were narrow and short (Figures 2b–e). The number of crazes increased with  $c_0$  and local breakdowns hardly occurred even at strains greater than 20%. Examined under the TEM (Figures 1c–d), the SWCNTs were revealed to be drawn into crazes. The SWCNT distribution within the nanocomposite was further unveiled by mildly etching the sample with low power O<sub>2</sub> plasma<sup>16,18</sup> before the AFM examination. No local height increase at the craze boundaries were observed (Figure 3b), indicating that there were no SWCNTs pileups at the craze boundaries. This behavior is in stark contrast to that of MWCNTs that accumulate at the craze-bulk boundaries and eventually restrict the chain drawing and force the sample to break in a brittle fashion.<sup>18</sup>

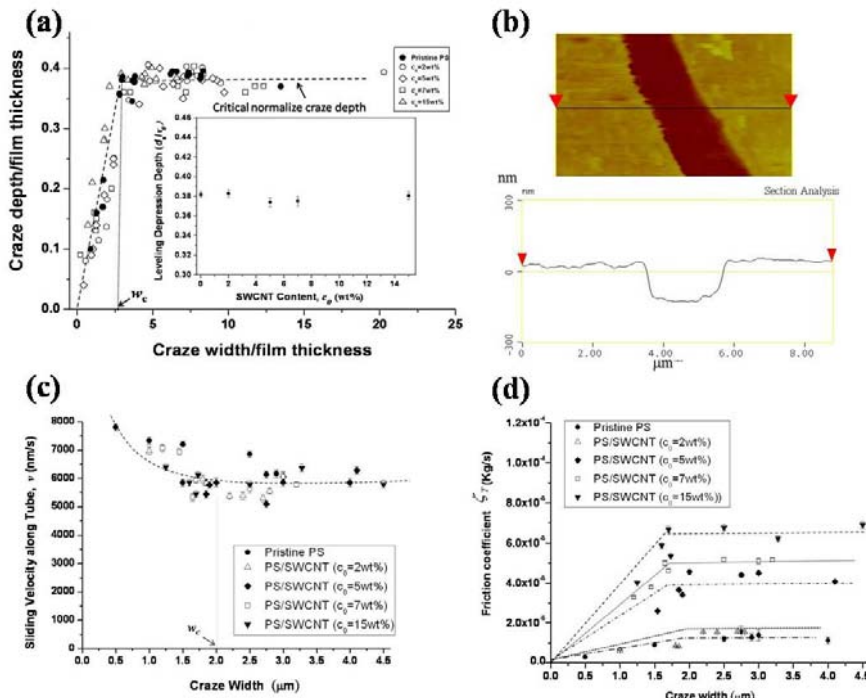


**Figure 3.** (a) Craze depth ( $d$ ) versus craze width ( $w$ ) for PS and SWCNT/PS films. Inset: Leveling depression depth versus  $c_0$ . (b) AFM micrograph of a stretched and SWCNTs/PS film ( $c_0 = 15\text{wt}\%$ ) etched by mild plasma. (c) The tube sliding velocity of a PS chain versus the craze width in both the pristine PS and SWCNT/PS films. (d) Friction coefficient of a PS chain versus craze width for pristine PS and SWCNT/PS films.

The microdrawing process was further studied by analyzing the AFM craze topography. It revealed a micro-necking process similar to that dominates the pristine PS in that the craze depression  $d$  increased linearly with  $w$  until  $w_c$  and then leveled off at  $d_s$ . Very surprisingly, however, was the discovery that the micronecking  $d$ - $w$  curve of the SWCNT/PS nanocomposites in independent of  $c_0$ , followed exactly the same curve as that of the neat PS (Figure 3a). This indicates that the fibril drawing processes in the SWCNTs/PS nanocomposites were utterly unchanged by the incorporation of SWCNTs (Figure 3a, inset).

The fibril drawing mechanics were studied further by assuming that the polymer chains are pulled along the confining tube under a constant force ( $f$ ) with a steady-state moving speed  $V$  that follows<sup>18,25</sup>  $f = V\zeta_T$  where  $\zeta_T$  is the characteristic chain friction coefficient. The chain pulling speed  $V$ , which can be calculated from the craze widening speed<sup>18</sup>, was found to decrease slightly with craze widening until it saturated ( $V_s$ ) for  $w > w_c$  (Figure 3c). The decrease in  $V$  is consistent with strain hardening at

the onset of steady-state necking. With the pulling force  $f$  calculated from the AFM craze topography using the Bridgman plastic model<sup>7,16,18</sup>, the chain friction  $\zeta_T$  was obtained. For the pristine PS,  $\zeta_T$  increased with  $w$  but subsequently leveled off in the steady-state necking ( $w > w_c$ ) (Figure 3d). The incorporation of SWCNTs caused  $\zeta_T$  to increase from  $1.1 \times 10^{-5}$  kg/s for the pristine PS to  $6.9 \times 10^{-5}$  kg/s for  $c_0 = 15$  wt%. This increase, however, does not impart influences on strain hardening of the nanoplactic process, as shown in Figure 3a.

Resulted from the restricting of craze widening that grew only very narrow crazes in the stretched film, the incorporation of SWCNTs endowed a reinforcement effect in the nanocomposite by suppressing local craze breakdowns which deceases exponentially with  $w$ .<sup>2,5,9</sup> Both the increase of the induced elastic stress around the deformation zones and the elevation of chain friction of nanoplactic flows were responsible for the strain delocalization. Ironically, the same factors contribute to the ultimate embrittlement in films of  $c_0$ 's greater than 20 wt% (Figure 2f).

**Densely Entangled Chain Systems.** The nanoplactic flows were further examined with the chain entanglement density increased roughly fivefold by using PPO as the polymer matrix. In pristine PPO films, SDZs were initiated at strains of ca.  $\epsilon = 2\%$  and started to break down to form cracks for  $\epsilon > 13\%$ . Figure 4d demonstrated a TEM micrograph of an SDZ that was characterized by its smooth surface contour and the absence of fibril/voids structure. The maximum widths of the SDZs may grow up to ca.  $40\ \mu\text{m}$  in width before cracking (Figure 4a). Similar to crazing, shear yielding also followed the micronecking mechanics.<sup>13,18</sup> The SDZ morphology underwent significant changes as the SWCNTs were dispersed in the PPO matrix. The SDZs became notably shorter and narrower ( $w < 15\ \mu\text{m}$ ) even at a low value of  $c_0$  at 2 wt% (Figure 4b). The fracture strain remained relatively unchanged at low  $c_0$ 's (at  $\sim 16\%$ ) but decreased significantly as  $c_0$  increases (Figure 4c). The film cracked at  $\epsilon = 6\%$  for  $c_0 = 5$  wt%. As will be shown in the following paragraphs, the hastened failure was due to the limitation of the chain extensibility in the SWCNTs/PPO films. Under the TEM (Figures 4e and 4f), the SWCNTs were observed to be drawn into the SDZs in a similar fashion as that in the SWCNT/PS system. However, probably due to the considerably smaller bending moment as compared to that of MWCNTs ( $\sim 10^4$ -fold), no debonding were observed at the SWCNT surfaces, in sharp contrast to the extensive debonding observed on MWCNTs in the PPO matrices.<sup>18,33</sup>

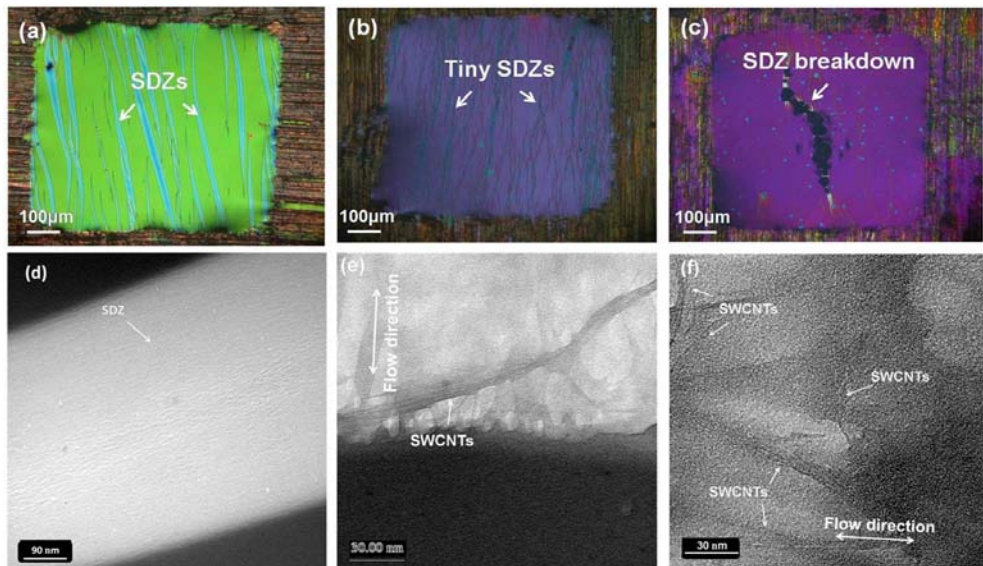


**Figure 4.** (a–c) Optical micrographs of stretched (a) pristine PPO films and (b, c) SWCNTs/PPO composite film with  $c_0$  of (b) 2 wt% and (c) 5 wt%. TEM micrographs of SDZs in (d) the PPO film and (e, f) SWCNT/PPO films ( $c_0 = 2$  wt%).

The embrittlement of SDZs by the incorporated SWCNTs was studied by examining the micronecking behavior under AFM (Figure 5a). In contrary to that illustrated in the PS systems, the leveling depth ( $d_s$ ) decreased substantially with  $c_0$ , indicating the drastic decrease of the extensibility

of the entangled chain network in the SWCNTs/PPO nanocomposites. This behavior also illustrates that the dispersed SWCNTs accelerated considerably the eventual strain hardening of the nanoplastic flows. Quantitatively, the local draw ratio,  $\lambda_{SDZ}$ , of the SDZ nanoplastic flows was related to  $d_s$  by<sup>9–10,18</sup>  $\lambda_{SDZ} \approx \tau_0/(\tau_0 - 2d_s)$ . The decrease of  $d_s/\tau_0$  from ~0.25 (pristine PPO film) to ~0.11 (SWCNTs/PPO,  $c_0 = 5$  wt% film) translated into a reduction of  $\lambda_{SDZ}$  from ~2.0 to ~1.3. The restriction on the network extensibility is obviously the main cause of the SWCNTs-induced embrittlement.

The chain pulling speed  $V$  and the tube friction coefficient  $\zeta_T$  in the PPO systems were calculated following the same procedures as above. The chain pulling speeds generally decreased with the width of SDZs (Figure 5b), truthfully reflecting strain hardening at the onset of steady-state nanoplastic flows. On the other hand, the addition of the SWCNTs in PPO modestly increased the chain friction, similar to that observed in the SWCNT/PS systems.<sup>18</sup> The chain friction coefficient ( $\zeta_T$ ) was found to increase from  $4.3 \times 10^{-5}$  kg/s for neat PPO films to  $6.7 \times 10^{-5}$  kg/s for  $c_0 = 5$  wt% (Figure 5c).

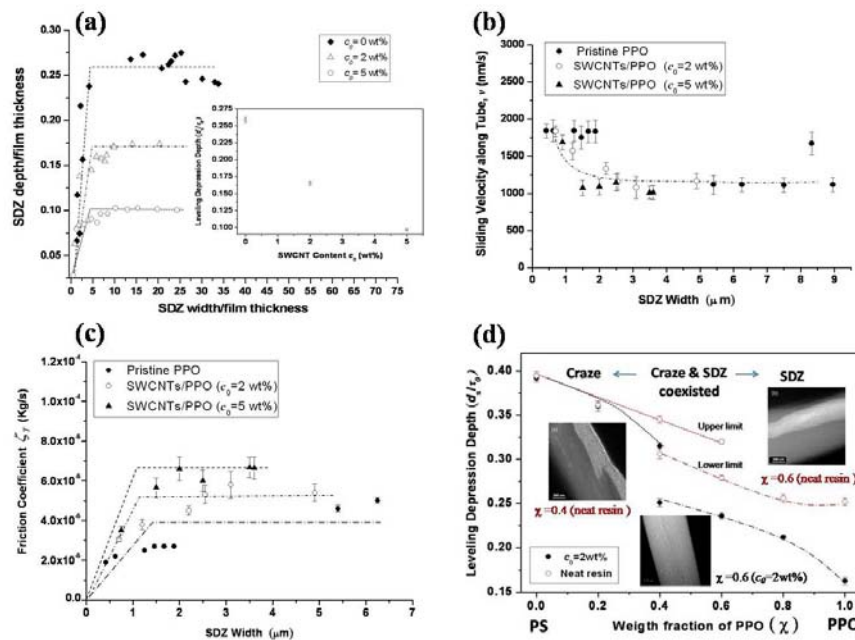


**Figure 5.** (a) SDZ depth ( $d$ ) versus craze width ( $w$ ) for PPO and SWCNT/PPO films. Inset: Leveling depression depth versus  $c_0$ . (b) The tube sliding velocity of a PPO chain versus the craze width for pristine PPO and SWCNT/PPO films. (c) The friction coefficient of a PPO chain versus the craze width for both the pristine PPO and SWCNT/PPO films. (d) The leveling depression depth versus the PPO content in PPO-PS and SWCNT/PPO-PS blends.

**Intermediate  $v_e$  Networks by Blending.** The effect of chain entanglement density was further investigated by blending the fully miscible PS and PPO as the polymer matrix of which the entanglement density ( $v_e$ ) was estimated from  $v_e = \rho N_A / M_e$  (where  $\rho$  is the mass density of the polymer and  $N_A$  is Avogadro's number). The entanglement molecular weight  $M_e$  follows<sup>7,9,23,31</sup>  $M_e(\chi) = M_e(\text{PS})/(1+3.2\chi)$  where  $\chi$  is the PPO fraction in the blend ( $M_e \sim 17,000$  g/mol. for the neat PS). As  $\chi$  increased from  $\chi = 0$ ,  $v_e$  increased and the nanoplastic flows switched from crazing to shear yielding. Consistent with literature,<sup>31</sup> crazing was observed in the blends of low  $v_e$ 's ( $v_e < 6 \times 10^{25} \text{ m}^{-3}$ ,  $\chi \leq 0.2$ ), shear yielding dominated in the high  $v_e$  blends ( $v_e \geq 8.07 \times 10^{25} \text{ m}^{-3}$ ,  $\chi \geq 0.4$ ), and crazes and SDZs coexisted in the intermediate  $v_e$ 's of  $0.2 \leq v_e \leq 0.4$  (Figure 5d)<sup>2,9</sup>. In the intermediate  $v_e$  range, the upper and the lower limits of  $d_s$  were measured from deformation regions of dominantly crazing or local shear yielding, respectively. Micronecking was followed closely by all the films.

In these PPO-PS blends, the extent of SDZ necking was restricted once the SWCNTs were incorporated ( $c_0 = 2$  wt%) in that the surface depressions  $d_s$ 's reduced significantly for  $\chi > 0.2$  (Figure 5d). At the same time, the  $\chi$  range of the mix-mode also was compressed significantly. By contrast, the SWCNTs incorporation produced no effect for crazing as the  $d_s$  followed almost the same curve as

that of the neat resins (Figure 5d,  $\chi \leq 0.2$ ). These results elucidated the strong  $v_e$  dependence of the SWCNT effect on the extensibility of polymer entanglement networks.

**SWCNT deformations from interactions with nanoplastic flows.** The drawing of the SWCNTs into both the crazes and SDZs illustrates the strength and persistence of the SWCNTs-polymer interactions over a relatively large scale of time (or length) that allows the SWCNTs to “flow” with the polymer chains during the nanoplastic flows. For this to happen, particularly for crazes, significant deformations of the SWCNTs (such as tube bending) induced by the polymer flows must have happened as the interfacial interactions based on friction between the short grafted PS chains on the tubes ( $M_w \sim 38\text{g/mol.}$ ) and the matrix are too limited to produce extensive center-of-mass movements of the nanotubes. As revealed by previous experiments, this type of interfacial interaction produces only slippage of the polymer chains around the MWCNTs, which are too bulky to bend by the nanoplastic flows, leaving the CNTs excluded from the crazes.<sup>18</sup> Thus, to unveil the role of SWCNTs during nanoplastic flows, their deformational states were examined. For craze formation, the polymer flow branches into many tiny fibrils as soon as they are drawn into the craze. The spacing between these “flow branches”, which becomes the fibril spacing ( $D_0$ ) in the craze, acts as a gating measure for the incoming CNTs that go along with the polymer flows. Severe bending of SWCNTs thus is inevitable for the randomly oriented SWCNTs being drawn into fibrils during craze formation because the SWCNT lengths ( $> 2 \mu\text{m}$ ) are far greater than the fibril dimensions ( $\sim 10 \text{ nm}$  for PS<sup>1,9</sup>). Only when the drawing force  $F$  of the nanoplastic flow overcomes the critical force  $F_c$ , derived from the critical bending moment  $M_c$  required for fitting a CNT into the tiny fibrils, the CNTs are pulled into crazes.<sup>41</sup> The drawing force  $F$  was readily determined from the AFM craze topography based on the Bridgman necking plasticity.<sup>7,8,13</sup> While the critical force  $F_c$  was obtained from  $F_c = 8M_c/L$  ( $L$ : suspended length  $\sim$  fibril spacing), following an analogue to the flow-induced fibers deformation,<sup>32-36</sup> in which  $M_c$  was calculated from  $M_c = E\pi r^3 tk$  ( $E$ : CNT Young's modulus,  $k$ : CNT buckling curvature for fitting into craze fibrils =  $2/d_f$  with  $d_f$  being the fibril diameter,  $t$ : effective CNT wall thickness,  $r$ : CNT outer radius).

In the SWCNTs/PS nanocomposites, the measured drawing force  $F$  was found to be increasing with  $c_0$ , ranging from 17.7 nN (for  $c_0 = 2.0\text{wt\%}$ ) to 86.3 nN (for  $c_0 = 15\text{wt\%}$ )<sup>18</sup>, which is significantly greater than  $F_c = 3.46 \text{ nN}$  of SWCNTs (calculated from  $E \sim 1\text{TPa}$ ,  $d_f = 10 \text{ nm}$ , and  $t \sim 0.04\text{--}0.07 \text{ nm}$ ).<sup>19-20,37,38,42,44</sup> For comparison, in the MWCNTs/PS nanocomposite,  $F$  is in the range from 10.8 to 12.3 nN (for  $c_0$  from 2 to 3 wt%)<sup>18</sup>, orders of magnitude smaller than the bending force  $F_c = 2.16 \times 10^7 \text{ nN}$ . These calculations are in excellent agreement with observations that SWCNTs were drawn into crazes while MWCNTs were excluded.<sup>18</sup> (Note that the critical kinking bending moment of SWCNTs,  $M_c$  (kinking) = 13 nN-nm, is substantially greater than  $M_c$  (bending) = 4.3 nN-nm required for crazing in the nanocomposites, therefore SWCNT kinking was ignored here.)

**“Phantom tube” behavior and heterogeneous chain motions.** With bending the dominant deformation mode of SWCNT in their interactions with nanoplastic flows, the existence of SWCNTs may produce no effect on chain extensibility if the bending incurred by the flow stress is sufficient to allow them to pass freely through the chain entanglement meshes; and vice versa. Calculated from the critical bending moment ( $F_c = 8M_c/L$ , with SWCNT diameter = 1.0 nm),  $F_c = 3.78 \text{ nN}$  for PS (mesh size  $\sim 9.6 \text{ nm}$ ) and  $F_c = 15.75 \text{ nN}$  for PPO (mesh size  $\sim 4.8 \text{ nm}$ ). Whilst the exerting force  $F$ , calculated from  $\tau A$  ( $A$  = entanglement spacing  $\times$  the CNT diameter), is from 2.2 to 4.1 nN for PS ( $c_0 = 2.0\text{--}5.0 \text{ wt\%}$ ) or from 0.62 to 1.82 nN for PPO ( $c_0 = 2.0\text{--}5.0 \text{ wt\%}$ ). Obviously,  $F < F_c$  for all  $c_0$ 's in PPO, thus the incorporated SWCNTs interfere with the movements of the entangled chains, consistent with the observations that the SWCNTs reduced the draw ratios of the PPO chains. However, for PS crazes,  $F < F_c$  is also obtained, in contradiction to the observed “phantom tube” behavior in PS. Therefore, the chain entanglement network of PS must have undergone significant modifications during fibril drawing.

According to the conventional convictions, this modifications may proceed by chain scissions or chain disentanglements.<sup>9-14,39,40</sup> However, chain scission is not dominant during crazing as the chain pulling force was  $\sim 0.065 \text{ nN}$  (or  $\tau = 94 \text{ MPa}$ ) for the steady-state necking, not enough to incite chain scissions that require a force of 4nN (or  $\tau = 6.0 \text{ GPa}$ ).<sup>16,18,40</sup> Effective disentanglements are also highly unlikely to occur as there are on average more than 100 entanglements along a single PS chain ( $M_w = 2000\text{kg/mol.}$ ,  $M_e \sim 17.5\text{kg/mol.}$ ). With such, any affine molecular deformation associated with the chain network would be impossible to explain the observed “phantom tube” behavior of SWCNTs in the PS matrix. Insightful clues may be found in the partially relaxed craze fibril structure that

manifests a quasi-regular mesh pattern constructed of voids surrounded by straightened fibril segments (of an unbroken length  $\sim 40$  nm) and fibril nodes (Figure 1b). This structure can be conceived as created from local entanglement clustering via chain sliding. With the entanglement clustering dominating, the SWCNTs pass through the chain entanglements freely during the nanoplastic flows as  $F_c$  now reduces to 0.22 nN, well below the drawing force of the nanoplastic flows ( $F = 2.2$  to 4.1 nN). This heterogeneous behavior, although requiring further explorations, conceivably arises from the large fluctuations of inter-chain couplings of the loosely entangled PS chains, and may find similar analogues, e.g., the banding phenomena of polymer melts under large shear.<sup>45,47</sup> For the tight entanglement networks, such as PPO's, the chain coupling fluctuations are significantly limited so that chain flows uniformly during the nanoplastic flows. The internal friction incurred during entanglement clustering may contribute to the toughening effect by crazing in thermoplastics. Finally, the dynamic behavior of polymer chains in the glassy state is very important for understanding the physical state of polymer glasses for the theoretical development. It is also crucial for the control over the various polymer properties demonstrated in the vast real applications. The knowledge of which, however, is still elusive. Our endeavor here may have provided some important progress in this exploration.

## Conclusions

In summary, the micromechanics of nanoplastic flows and the nanoscopic interactions between the glassy polymer chains and the embedded SWCNTs were studied. The dispersion of the surface-grafted SWCNTs in a polymer matrix significantly enhances the fracture toughness through effective elastic interactions and delocalization of the plastic strains. The drawing stress and micronecking behavior of the strain-softened chains during the nanoplastic flows were investigated for various matrix entanglement densities. The SWCNTs, unlike MWCNTs, were found to intimately interact with the polymer chains during the nanoplastic flows in a fashion highly dependent on the chain entanglement density. For tight chain entanglement networks ( $v_e \geq 8.07 \times 10^{25}$  chains/m<sup>3</sup>), the SWCNTs fully participated in the fibrillation process and significantly interfered the extension ratio of the fibrils. In sharp contrast, the SWCNTs behaved as "phantom tubes" in the loose chain entanglement network ( $v_e < 6 \times 10^{25}$  chains/m<sup>3</sup>), producing no effect on the nanoplastic flows. According to the micromechanical calculations of the SWCNT deformations, this "phantom tube" behavior is only possible when the entangled chains undergo chain sliding during nanoplastic flows to result in local entanglement clustering that effectively alters the entanglement network for the SWCNTs to pass freely. This type of chain motions is consistent with the observed craze fibril microstructures. The result bears very important implications on the fundamental properties of glassy polymer chains (e.g., the chain dynamics during strain-softening or yielding) and the reinforcement role by SWCNTs in glassy polymer nanocomposites.

## Acknowledgments

We thank the financial supports by both the National Science Council of Taiwan and the US Air Force Office of Scientific Research (AFOSR) through the Taiwan-US Air Force Nanoscience Program (AOARD-084125 and -094024).

## References

- (1) Yang, A. C.-M.; Kramer E. J.; Kuo, C. C.; Phoenix, S. L. *Macromolecules* **1986**, *19*, 2020.
- (2) Kramer, E. J.; Berger, L. L. *Adv. Polym. Sci.* **1990**, *91/92*, 1.
- (3) Yang, A. C.-M.; Kramer, E. J. *J. Polym. Sci.-Polym.Phys.* **1985**, *23*, 1353.
- (4) Yang, A. C.-M.; Kramer, E. J. *J. Mater. Sci.* **1986**, *21*, 3601.
- (5) Yang, A. C.-M.; Kramer E. J.; Kuo, C. C.; Phoenix, S. L. *Macromolecules* **1986**, *19*, 2010.
- (6) Yang, A. C.-M.; Kunz, M. S.; Logan, J. A. *Macromolecules* **1993**, *26*, 1776.
- (7) Lin, J. H.; Yang, A. C.-M. *Macromolecules* **2001**, *34*, 3698.
- (8) Lin, C. H.; Yang, A. C.-M. *Macromolecules* **2001**, *34*, 4865.
- (9) Kramer, E. J. *Adv. Polym. Sci.* **1983**, *52/53*, 1.
- (10) Donald, A. M., Kramer, E. J. *J. Polym. Sci.-Polym. Phys.* **1982**, *20*, 899.
- (11) Donald, A. M.; Kramer E. J. *Polymer* **1982**, *23*, 457.
- (12) Yang, A. C.-M, Wang, R. C., Lin, J. H. *Polymer* **1996**, *37*, 5751.

- (13) Yang, A. C.-M.; Wang, R. C.; Kunz, M. S.; Yang, I. C. *J. Polym. Sci., Polym. Phys. Ed.* **1996**, *34*, 1141.
- (14) Henkee, C. S.; Kramer, E. J. *J. Polym. Sci.-Polym. Phys.* **1985**, *22*, 721.
- (15) Ma, W.; Liu, L.; Zhang, Z.; Yang, R.; Liu, G.; Zhang, T.; An, X.; Yi, X.; Ren, Y.; Niu, Z.; Li, J.; Dong, H.; Zhou, W.; Ajayan, P. M.; Xie, S. *Nano Lett.* **2009**, *9*, 2855.
- (16) Hsiao, C. C.; Lin, T. S.; Cheng, L. Y.; Ma, C. C. M.; Yang, A. C.-M. *Macromolecules* **2005**, *38*, 4811.
- (17) Lin, T. S.; Cheng, L. Y.; Hsiao, C. C.; Yang, A. C.-M. *Mater. Chem. Phys.* **2005**, *94*, 438.
- (18) Lin, C. W.; Huang, L. C.; Ma, C. C. M.; Yang, A. C.-M. Y.; Lin, C. J.; Lin, L. J. *Macromolecules* **2008**, *41*, 4978.
- (19) Moniruzzaman, M.; Winey, K. I. *Macromolecules* **2006**, *39*, 5194.
- (20) Salvetat, J. P.; Briggs, G. A. D.; Bonard, J. M.; Bacsa, R. R.; Kulik, A. J.; Stockli, T.; Burnham, N. A.; Forro, L. *Phys. Rev. Lett.* **1999**, *83*, 944.
- (21) Kong, H.; Gao, C.; Yan, D. *Macromolecules* **2004**, *37*, 4022.
- (22) Berger, L. L. *Macromolecules* **1989**, *22*, 3162.
- (23) Whitten, P. G.; Brown, H. R. *Phys. Rev. E.* **2007**, *76*, 026101.
- (24) Rottler, J.; Robbins, M. O. *Phys. Rev. E.* **2003**, *68*, 011801.
- (25) Rubinstein, M.; Colby, R. H. *Polymer Physics*; Oxford University Press; Oxford, 2003; Chapter 9.
- (26) Kumar, S.; Dang, T. D.; Arnold, F. E.; Bhattacharyya, A. R.; Min, B. G. Zhang, X.; Vaia, R. A.; Park, C.; Adams, W. W.; Hauge, R. H.; Smalley, R. E.; Ramesh, S.; Willis, P. A. *Macromolecules*, **2002**, *35*, 9039.
- (27) Moniruzzaman, M.; Winey, K. I. *Macromolecules*, **2006**, *39*, 5194.
- (28) Crosby, A. J.; Lee, J. Y. *Polym. Rev.* **2007**, *47*, 217.
- (29) Janmey, P. A.; McCormick, M. E.; Rammensee, S.; Leight, J. L.; Georges, P. C.; Mackintosh *Nat. Mater.* **2007**, *6*, 48.
- (30) Sui, X.; Wagner, H. D. *Nano Lett.* **2009**, *9*, 1423.
- (31) Melick, H. G. H.; Govaert, L. E.; Meijer, H. E. H. *Polymer* **2003**, *44*, 2493.
- (32) Gibson, S. L.; Pathak, J. A.; Grulke, E. A.; Wang, H.; Hobbie, E. K. *Phys. Rev. Lett.* **2004**, *92*, 048302.
- (33) Schmid, C. F.; Klingenberg, D. J. *Phys. Rev. Lett.* **2000**, *84*, 290.
- (34) Xu, D. H.; Wang, Z. G.; Douglas, J. F. *Macromolecules* **2008**, *41*, 815.
- (35) Kharchenko, S. B.; Douglas, J. F.; Obrzut, J.; Grulke, E. A.; Migler, K. B. *Nat. Mater.* **2004**, *3*, 564.
- (36) Riley, W.; Sturges, L. D.; Morris, D. H. *Mechanics of Materials*; Wiley: Asia, 2006; Chapter 8.
- (37) Mylvaganam, K. Vodenitcharova, T.; Zhang, L. C. *J. Mater. Sci.* **2006**, 3341.
- (38) Jensen, W.; Kis, A.; Zettl, A. *Phys. Rev. B.* **2007**, *76*, 195436.
- (39) Kaucsh, H. H. *Macromol. Symp.* **2004**, *214*, 17.
- (40) Arlette, R. C. B.; Robbins, M. O. *Science*, **1996**, *26*, 271.
- (41) Silvestre, N.; Camotim, D. *Nanotechnology in Construction 3: Proceeding of the NICOM3*; Springer Verlag, 2009; p 365.
- (42) Wang, C. Y.; Zhang, L. C. *Nanotechnology* **2008**, *19*, 075705.
- (43) Yankobson, B. I.; Brabec, C. J.; Bernholc, J. *Phys. Rev. Lett.* **1996**, *76*, 2511.
- (44) Salvetat, J. P.; Kulik, A. J.; Bonard, J. M.; Brigg, G. A. D.; Stockli, T.; Metenier, K.; Bonnamy, S.; Beguin, F.; Burnham, N. A.; Forro, L. *Adv. Mater.* **1999**, *11*, 161.
- (45) Wang, S. Q.; Ravindranath, S.; Boukany, P.; Olechnowicz, M.; Quirk, R. P.; Halasa, A.; Mays, J. *Phys. Rev. Lett.* **2006**, *97*, 187801.
- (46) Tapadia, P.; Wang, S. Q. *Phys. Rev. Lett.* **2006**, *96*, 016001.
- (47) Tapadia, P.; Ravindranath, S.; Wang, S. Q. *Phys. Rev. Lett.* **2006**, *96*, 196001.